Modeling and Validating Orbits and Clocks Using the Global Positioning System

Inauguraldissertation
der Philosophisch-naturwissenschaftlichen Fakultät
der Universität Bern

vorgelegt von

Timon Anton Springer

aus den Niederlanden

Leiter der Arbeit:	Prof. Dr. Gerhard Beutler Astronomisches Institut der Universität Bern Prof. Dr. Markus Rothacher Technische Universität München Dr. Jan Kouba National Resources Canada

Modeling and Validating Orbits and Clocks Using the Global Positioning System

Inauguraldissertation
der Philosophisch-naturwissenschaftlichen Fakultät
der Universität Bern

vorgelegt von

Timon Anton Springer

aus den Niederlanden

Leiter der Arbeit: Prof. Dr. Gerhard Beutler
Astronomisches Institut der Universität Bern
Prof. Dr. Markus Rothacher
Technische Universität München
Dr. Jan Kouba
National Resources Canada

Von der Philosophisch-naturwissenschaftlichen Fakultät angenommen.

Der Dekan:

Bern, den 4. November 1999 Prof. Dr. A. Pfiffner

Contents

List of Tables

List of Figures

1 Introduction

This work covers a broad range of different topics such as orbit modeling, orbit validation using satellite laser ranging observations, time transfer, station coordinates and velocities, and Earth rotation. The common aspect of these very different topics is the Global Positioning System (GPS). The GPS is a satellite system for global navigation and positioning developed by the U.S. Department of Defense. Nominally it consists of 24 satellites in six orbital planes. The signals of these satellites may be tracked by receivers on or near the Earth and can be used for a large variety of applications in the fields of navigation, geodesy, and timing. Apart from the GPS we will also make use of the Russian Global Navigation Satellite System (GLONASS), which, from the technical point of view, is a close relative of the GPS.

Over the last decade GPS has started to play a major role in regional and global studies of the Earth. To facilitate the use of the GPS system and to improve the results for regional and global network solutions the International GPS Service (IGS) was conceived. The main goals of the IGS are to collect and archive GPS data from a global network and to generate precise orbits of the GPS satellites. The generation of precise orbits is important in order to reduce, or even eliminate, the effect of orbit errors on geodetic network solutions. The IGS, which is based on voluntary contributions of a large number of organizations, started in 1992 with a 3-month test campaign. Thanks to the success of this test campaign, the IGS continued after the initial three months. The official start of the IGS took place in 1994. The core products of the IGS are the data from the global network of approximately 200 stations, precise GPS satellite orbits and clocks, Earth rotation parameters, station coordinates and velocities, station specific tropospheric zenith path delays, global ionosphere maps, and GPS receiver clock estimates.

The Center for Orbit Determination in Europe (CODE), located at the Astronomical Institute of the University of Berne (AIUB), participates in the IGS as one of the analysis centers. CODE has been part of the IGS since the start in June 1992. Thus it has been processing the GPS observations of a global network on a daily basis for more than seven years using the Bernese GPS software package. Thanks to the daily activities performed at CODE within the framework of the IGS, long time series of precise results are readily available. The time series of these estimates, which include orbit estimates, solar radiation pressure accelerations, station coordinates, geocenter estimates, and Earth rotation parameters, are the basis for the investigations described in this work. Many improvements were made in the processing algorithms used at the IGS analysis centers over the years of IGS activities. Apart from these algorithm improvements, the GPS system was upgraded from 19 satellites at the end of 1992 to the full constellation of 24 satellites by 1994. Also, the IGS global tracking network improved dramatically in a few years time. In June 1992 data from approximately 30 permanent global GPS receivers were available. This number has grown rapidly to well over 200 stations in 1998.

In our opinion the key to the IGS improvements has been the continuous validation of the IGS products by means of inter-comparing and combining the results of the IGS analysis centers. The feedback emerging from these comparisons has led to significant improvements in, e.g., the orbit parameterization resulting in improved orbit quality. The high quality of the orbit estimates has improved the understanding of the GPS orbit model. This improved understanding showed that the solar radiation pressure model originally adopted for the GPS satellites, is no longer adequate for precise orbit estimation. Solar radiation pressure is the biggest non-gravitational acceleration acting on the GPS satellites. An accurate solar radiation pressure model is therefore equally important for high accuracy GPS orbits as an accurate gravity model of the Earth.

One of the limitations of most comparisons performed within the IGS is that they only compare the results stemming from one single technique, i.e., the GPS microwave observation technique. In some cases it is difficult to find accurate external references for comparisons like, e.g., for the orbit and the tropospheric zenith delay estimates. For the station coordinates and the Earth rotation parameters results from other space geodetic techniques, e.g., satellite laser ranging (SLR) and very long baseline interferometry (VLBI), are readily available. To provide some limited means of comparison, two GPS satellites were equipped with a small laser retroreflector array. These two GPS satellites may be observed by the ground station tracking network of the International Laser Ranging Service (ILRS). The observations may be used in turn to obtain an independent validation of the IGS orbit quality. Similarly, we may also use the SLR observations taken from the GLONASS satellites, which are *all* equipped with a large retroreflector array, to validate the orbit quality of the precise orbits produced for the International GLONASS Experiment (IGEX). Furthermore, the combination of the microwave and SLR (optical) observations will be of benefit for all parameters common to both techniques.

The high quality of the IGS products has led to the usage of the GPS system for several new applications, e.g, for meteorology and time transfer. In this work the IGS products of the CODE analysis center are used to demonstrate the usefulness of GPS for precise time transfer at the sub-nanosecond level. GPS is already a widely accepted technique for time transfer. The method applied, however, the so-called common-view method, does not exploit the full potential of the GPS. The precision of the common-view method is at the few nanosecond level. The IGS satellite clock estimates have been demonstrated to be at least a factor of ten better. To obtain receiver and/or satellite clock estimates from GPS data processing, the commonly used double differencing approach cannot be used. This has implications on the processing strategy like, e.g., the cleaning and processing of undifferenced carrier phase data.

Let us now give a short overview of the subsequent chapters. In Chapter 2 the basics of the GPS, its observation types, linear combinations, and differencing methods, are discussed. It also contains a brief introduction of the GLONASS. Chapter 3 gives an overview of the models needed to process GPS data from global networks.

In Chapter 4 we introduce the IGS and many of its products. The routine IGS processes at the CODE analysis center are presented followed by an overview of varies CODE and IGS products like, e.g., orbits, Earth rotation parameters, station coordinates and velocities. A short introduction of how to use IGS products for regional networks is given.

Chapter 5 describes the developments which took place within the IGS over the years of its existence, focusing on the CODE analysis center, and the effect these developments had on the CODE and IGS products. We highlight some of the significant improvements which were achieved within the IGS and the expansion of the number of applications of the GPS system due to the IGS products. The potential of the GPS to provide a high time resolution of the estimated parameters is demonstrated using sub-daily Earth rotation estimates. The importance of performing ambiguity fixing, using low elevation data, and proper modeling and estimation of the tropospheric delays is shown. The chapter also discusses the current limitation of the accuracy of the IGS products due to, e.g., the antenna phase center offsets of both, the transmitting and receiving antennas, and the unexplained geocenter shift observed in the early IGS results. The chapter is concluded with an overview of the current precision of the CODE and IGS products.

In Chapter 6 we review the solar radiation pressure model of GPS satellites. First, the commonly used radiation pressure model, the ROCK-model, is introduced. Then we give a description of the extended CODE orbit model, an orbit parameterization which is well suited to absorb the effects of solar radiation pressure on the GPS satellites. Based on the experiences and results obtained using the extended CODE orbit model, a new solar radiation pressure model is derived. The complete time series of IGS precise orbits, starting in June 1992, is used for that purpose. The new model is presented, validated, and compared to other models.

In Chapter 7 the SLR observations of the GPS satellites are processed to validate the quality of the CODE IGS orbits. The SLR observations provide a completely independent check of the (radial) orbit errors of the IGS orbit estimates which are based on microwave observations. The same validation is also performed using the IGEX orbits and the SLR observations of the GLONASS satellites.

In Chapter 8 the use of the GPS system and the IGS products is presented for the purpose of time transfer. First we discuss the observation cleaning of undifferenced GPS data. Then, results from different time transfer experiments are presented to reveal the capabilities of the GPS in this area. Finally, the satellite clock estimates and their use for precise point positioning are discussed.

Chapter 9 contains a brief summary the results achieved in this work. Possible future directions of research are discussed.

2 The Global Positioning Systems and Their Observables

2.1 The GPS

In 1973 a project group was formed with representatives of the U.S. armed forces and the Defense Mapping Agency to develop a new navigation and positioning system. This new satellite positioning system, which would replace the old DOPPLER- or TRANSIT-navigation system, became known as the NAVSTAR GPS. Where NAVSTAR stands for "NAVigation by Satellite Timing And Ranging", and GPS for "Global Positioning System". The system was put into operation by the U.S. Department of Defense for military applications. Civilian users are given access with some restrictions. The name GPS is most commonly used today. We will use the term GPS from here onwards as a synonym to NAVSTAR GPS. The main characteristic of the GPS is that it is a continuously available global system which allows for instantaneous position determination using simultaneously measured pseudo-ranges to at least four satellites. For a thorough discussion of the GPS we refer to, e.g., [*Wells et al.*, 1987; *Hofmann-Wellenhof et al.*, 1992; *Leick*, 1995].

The presently available full constellation guarantees simultaneous observations of at least four GPS satellites from (almost) every point on the surface of the Earth at (almost) every time of the day. This is accomplished by 24 satellites (21 plus 3 active spares) located in six orbital planes in almost circular orbits with an altitude of about 20 200 km above the surface of the Earth. The orbital plane is inclined by 55^o with respect to the equator. The sidereal revolution period of the GPS satellites is 11 hours 58 minutes (approximately half a sidereal day). Consequently, the same satellite configuration is repeated 4 minutes earlier every day for one and the same location. This leads to an almost perfectly repeated "ground-track" (projection of the satellite position on the Earth) of the GPS satellites as shown in Figure 2.1. Due to this orbital revolution period the GPS satellites are in deep 2:1 resonance with the rotation of the Earth with respect to inertial space which gives rise to resonance perturbations [*Hugentobler*, 1997].

The first GPS satellite PRN 4 (PRN: Pseudo-Random Number) was launched on February 22, 1978. PRN 4 was the first in a series of 11 so-called Block I satellites. The Block I satellites had an inclination of about 63^o with respect to the equator. At present the Block I satellites are no longer active. They were followed by the Block II, IIA and IIR satellites. The

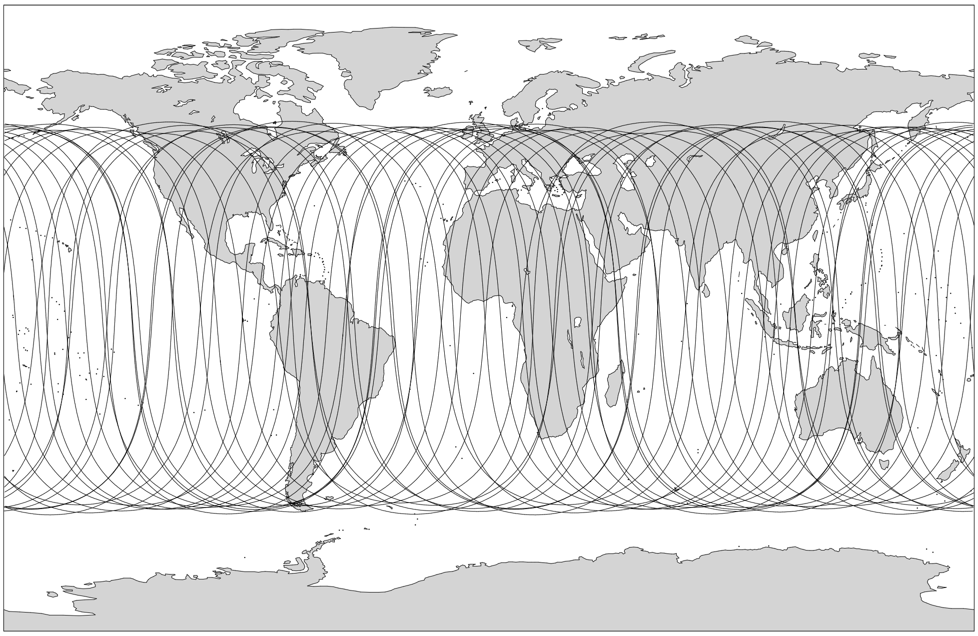

(a) All satellites

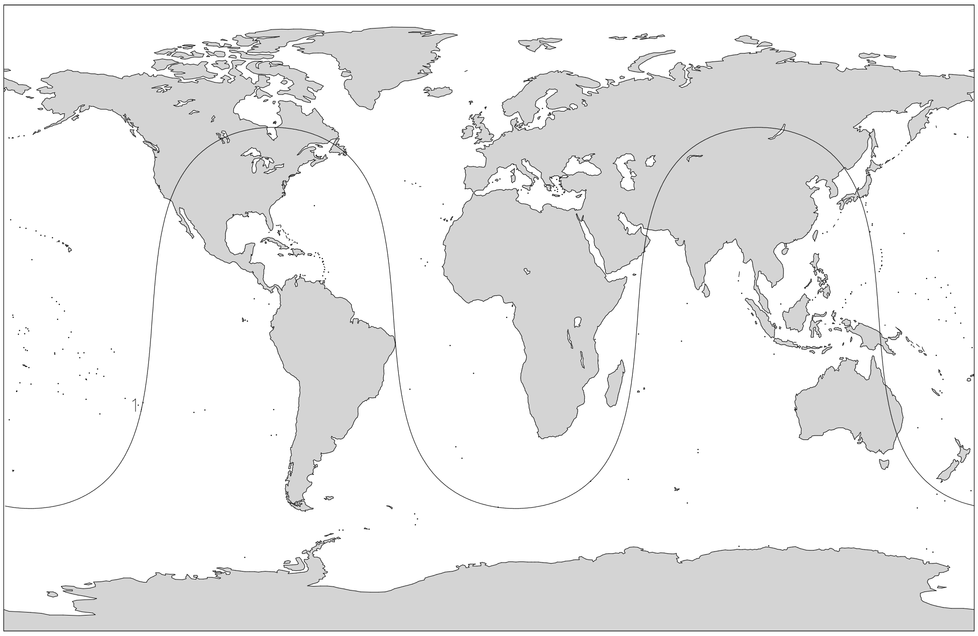

(b) PRN 1 only

Figure 2.1: Ground-tracks of the GPS over 24 hours, 2 full orbital revolutions, for June 1, 1998.

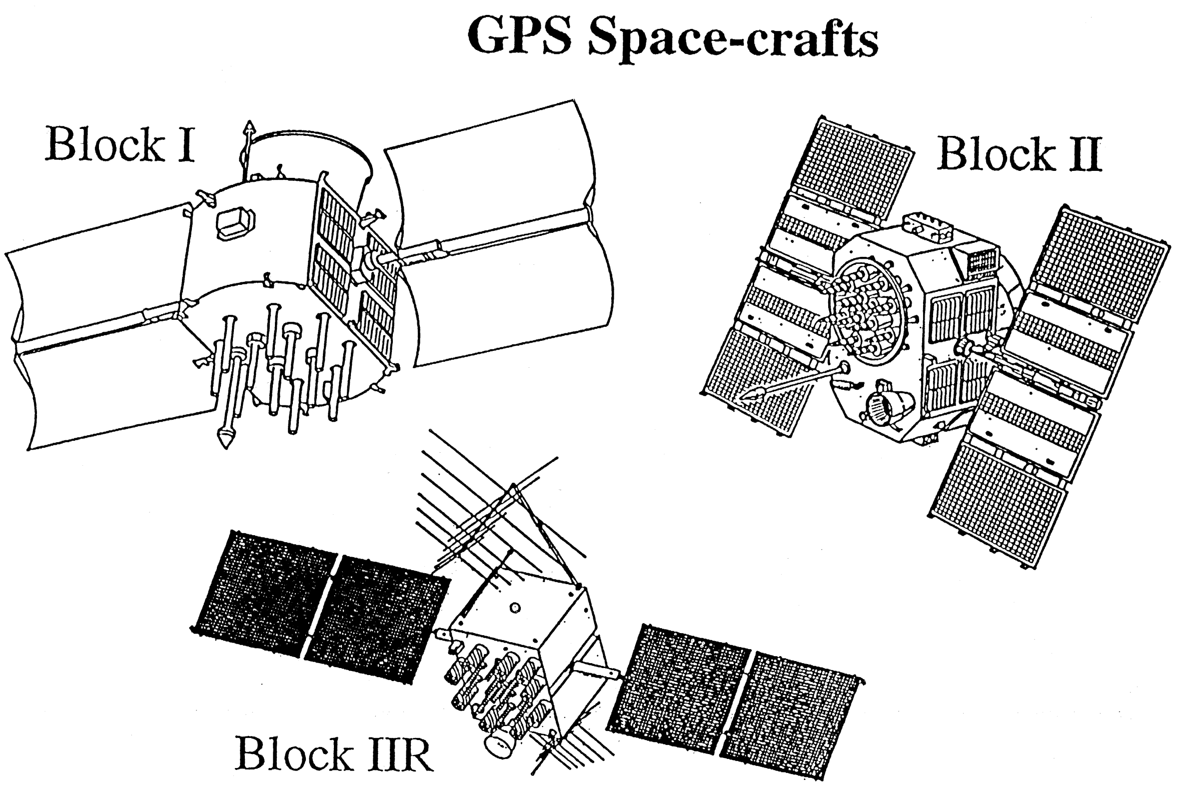

Figure 2.2: GPS satellites of different generations: Block I, II and IIR (from *Fliegel et al.* [1992]).

different satellite Block types are shown in Figure 2.2. The Block II and IIA satellites are very similar and therefore only a Block II satellite is shown in Figure 2.2.

The operational constellation is realized by the Block II and Block IIA satellites. The first Block II satellite was launched in February 1989. The current constellation, consisting of 27 satellites, is listed, including some history, in Table 2.1. The constellation currently contains one Block IIR satellite, PRN 13. Table 2.1 gives both, the space vehicle number (SVN) and the pseudo-random number (PRN) of the satellites, the date of launch, the start and end of operation, and the slot. Note that we will always refer to the satellites by their PRN code number. The column “remarks” contains special information concerning the satellites, e.g., why the satellite stopped operation and problems during the operation. The following remarks are of significance here:

Wheels: Indicate that there are problems with the momentum wheels, which are needed for the satellite attitude control. If all momentum wheels fail this means that the attitude has to be maintained through thruster firings. In case of (partial) failure of the momentum wheels the so-called “momentum dumps”, achieved by thruster firings, will become much more frequent. These thruster firings cannot be modeled very accurately and therefore have severe implications on orbit modeling.

Panels: Satellite PRN23 cannot automatically point its panels towards the Sun. The panels are "manually" adjusted once per orbit revolution by the Master Control Center.

SLR LRA: Two satellites, PRN 5 and PRN 6, are equipped with a Laser Reflector Array (LRA) which enable tracking of the satellites by the Satellite Laser Ranging (SLR) system. For more information about SLR see Chapter 7.

All signals transmitted by the satellite (summarized in Table 2.2) are derived from the fundamental frequency (f_0) of the satellite oscillator. The two carrier frequencies, f_1 and f_2 (the corresponding wavelengths are $\lambda_1 \approx 19\ cm$ and $\lambda_2 \approx 24\ cm$), are modulated with the codes and the navigation message to transmit information such as the readings of the satellite clocks, the orbital parameters, etc. The C/A-code (Coarse-Acquisition, Clear-Access, or Civil-Access) is modulated on the L_1 carrier only. The P-code (Precise or Protected) is modulated on both carriers.

There are two limitations for civilian users, namely Selected Availability and Anti-Spoofing, briefly referred to as SA and AS, respectively. Both deteriorate the achievable accuracy for civilian users significantly.

Selective Availability (SA), the denial of full accuracy, is accomplished by "manipulating" navigation message orbit data (epsilon) and/or the satellite clock frequency (dither). So far, only the satellite clock frequency has been manipulated. With this dithering process the GPS satellite clocks are artificially degraded by adding a signal with an unknown frequency and amplitude to the know clock behavior. This is done to degrade the performance of GPS for the "normal" users. Both, the frequency and amplitude of the added signal, change rapidly over time. The amplitude of this "clock dithering" is of the order of 0.3 μs (100 meters) and the frequency is of the order of only a few minutes. This SA clock dithering limits the accuracy of real time position estimates to 25 meters RMS. Selected (military) users possess special "keys" to remove the SA-effect in real time giving them access to the full navigation potential of GPS, i.e., one meter real time absolute point positioning.

Figure 2.3 shows the effect SA has on the satellite clocks. It shows the satellite clock estimates every 30 seconds over a period of 6 hours for day 307 of 1998. Two satellites are shown, PRN 2 which is affected by SA and PRN 15 which is not affected by SA. The typical SA amplitude of the order 0.2–0.3 μs is clearly visible. The RMS of the clock variations over the 6 hour period are 83.3 ns and 3.5 ns for PRN 2 and PRN 15, respectively, corresponding to 25 and 1 meters.

Anti-spoofing (AS) is a protection against "fake" transmissions by encrypting the P-code to form the Y-code. This ensures that the GPS signals cannot be disturbed (spoofed) by a GPS-like transmitter on the Earth. The anti-spoofing procedure converts the P-code to the Y-code which is only usable when a secret conversion algorithm is available to the receiver. The Y-code is the "modulo two sum" of the P-code and the encryption code W. Only selected (military) users have access to the conversion algorithm. The effect of AS is that civilian users have only access to the C/A-code and therefore only to one single frequency. This disables the

SVN	PRN	Block	Launch	Slot	Operation			Remark
					Start	End	#Months	
1	4	I-1	22-Feb-78	–	29-Mar-78	25-Jan-80	21.9	Clock
2	7	I-2	13-May-78	–	14-Jul-78	30-Aug-80	25.5	Clock
3	6	I-3	6-Oct-78	–	9-Nov-78	19-Apr-92	161.3	Clock
4	8	I-4	11-Dec-78	–	8-Jan-79	27-Oct-86	93.6	Clock
5	5	I-5	9-Feb-80	–	27-Feb-80	28-Nov-83	45.0	Wheels
6	9	I-6	26-Apr-80	–	16-May-80	10-Dec-90	126.8	Wheels
8	11	I-8	14-Jul-83	–	10-Aug-83	4-May-93	116.8	EPS
9	13	I-9	13-Jun-84	–	19-Jul-84	25-Feb-94	115.2	EPS
10	12	I-10	8-Sep-84	–	3-Oct-84	18-Nov-95	133.5	Clock
11	3	I-11	9-Oct-85	–	30-Oct-85	27-Feb-94	99.9	TT&C
14	14	II-1	14-Feb-89	E1	14-Apr-89		112.6	Wheels
13	2	II-2	10-Jun-89	B3	12-Jul-89		109.6	
16	16	II-3	17-Aug-89	E5	13-Sep-89		107.6	Wheels
19	19	II-4	21-Oct-89	A4	14-Nov-89		105.6	wheels?
17	17	II-5	11-Dec-89	D3	11-Jan-90		103.7	
18	18	II-6	24-Jan-90	F3	14-Feb-90		102.6	wheels?
20	20	II-7	25-Mar-90	–	19-Apr-90	10-May-96	72.7	Wheels
21	21	II-8	2-Aug-90	E2	31-Aug-90		96.0	
15	15	II-9	1-Oct-90	D2	20-Oct-90		94.4	NO SA
23	23	IIA-10	26-Nov-90	E4	10-Dec-90		92.7	Panels
24	24	IIA-11	3-Jul-91	D1	30-Aug-91		84.0	wheels?
25	25	IIA-12	23-Feb-92	A2	24-Mar-92		77.2	
28	28	IIA-13	9-Apr-92	–	25-Apr-92	5-May-97	76.2	Hardware
26	26	IIA-14	7-Jul-92	F2	23-Jul-92		73.3	
27	27	IIA-15	9-Sep-92	A3	30-Sep-92		71.0	
32	1	IIA-16	22-Nov-92	F1	11-Dec-92		68.7	
29	29	IIA-17	18-Dec-92	F4	5-Jan-93		67.9	wheels?
22	22	IIA-18	2-Feb-93	B1	4-Apr-93		64.9	
31	31	IIA-19	30-Mar-93	C3	13-Apr-93		64.6	
37	7	IIA-20	13-May-93	C4	12-Jun-93		62.6	
39	9	IIA-21	26-Jun-93	A1	21-Jul-93		61.3	
35	5	IIA-22	30-Aug-93	B4	20-Sep-93		59.4	SLR LRA
34	4	IIA-23	26-Oct-93	D4	1-Dec-93		57.0	
36	6	IIA-24	10-Mar-94	C1	28-Mar-94		53.1	SLR LRA
33	3	IIA-25	28-Mar-96	C2	9-Apr-96		28.7	
40	10	IIA-26	16-Jul-96	E3	15-Aug-96		24.5	
30	30	IIA-27	12-Sep-96	B2	1-Oct-96		23.0	
38	8	IIA-28	6-Nov-97	A5	18-Dec-97		8.4	
43	13	IIR-2	22-Jul-97	F5	31-Jan-98		7.0	

Table 2.1: GPS constellation history and status of September 1998.

Component	**Frequency** [MHz]		
Fundamental frequency	f_0	=	10.23
Carrier L_1	$f_1 = 154\ f_0$	=	1575.42 ($\lambda_1 = 19.0\ cm$)
Carrier L_2	$f_2 = 120\ f_0$	=	1227.60 ($\lambda_2 = 24.4\ cm$)
P-code $P(t)$	f_0	=	10.23
C/A-code $C(t)$	$f_0/10$	=	1.023
Navigation message $D(t)$	$f_0/204600$	=	$50 \cdot 10^{-6}$

Table 2.2: Components of the GPS satellite signal.

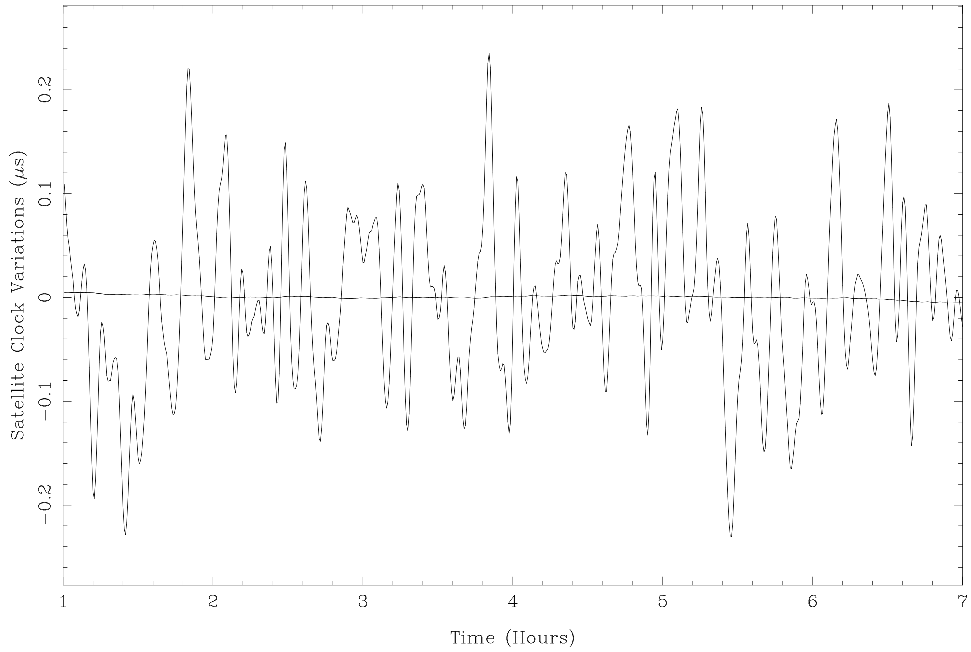

Figure 2.3: Effect of SA on PRN 2 on November 11, 1998. For reference also PRN 15 is plotted which is the only satellite without SA.

possibility to eliminate ionospheric refraction using observations on two different frequencies. This further limits the accuracy for the civilian users.

For real time non-differential applications, the SA effect limits the accuracy to about 100 meters. At this accuracy level the effect of AS is negligible because both, the effects of a more precise code and the ionosphere, are negligible compared to the 100 meter level SA effect. For real time differential GPS AS is the accuracy limiting factor. In differential applications, the SA effect cancels out almost completely. The accuracy is in this case limited by the degraded accuracy of the code and by ionospheric refraction.

2.2 The GLONASS

Although our main focus will be the NAVSTAR GPS, we include a short description of its Russian counterpart. This Russian GLobal NAvigation Satellite System (GLONASS), developed and deployed by the former USSR and maintained by the Russian federation, has much in common with the GPS in terms of the satellite constellation, the orbits, and the signal structure. Both systems are owned and operated by their respective defense departments and offer precise, global, and continuous positioning capabilities. Both transmit signals on two frequencies in the L-band (1.2 GHz and 1.6 GHz), and make a subset of signals available for civil use.

The fully deployed GLONASS constellation is composed of 24 satellites in three orbital planes with ascending nodes separated by 120^o on the equator. Each orbital plane contains 8 satellites equally spaced with a separation of 45^o. The arguments of latitude of the satellites in subsequent orbital planes are shifted by 15^o. GLONASS orbits are almost circular in an altitude of 19 100 km with an inclination of 64.8^o w.r.t. the equator. The sidereal revolution period of the GLONASS satellites is approximately 11 hours 15 minutes. As opposed to the GPS the ground-track of the GLONASS satellites do not repeat after one day. This avoids the resonance effects which makes station keeping of GPS satellites difficult and expensive. The constellation of satellites should guarantee that a minimum of 5 satellites is in view to users world-wide, with adequate geometry, i.e., the GLONASS constellation allows for continuous and global navigation.

GLONASS is still in development. In January 1996 the system had a full constellation of 24 active satellites. However, no new satellites were launched until December 1998. The guaranteed lifetime for the GLONASS satellites is about 3 years compared to 7.5 years for the GPS Block II and IIA satellites, and 10 years for the Block IIR satellites. Due to this relatively short lifetime of the GLONASS satellites there remain only 15 active satellites in April 1999. The main advantage of GLONASS is that there are no plans to degrade the signals for civil use. This has major advantages for real-time applications. A significant difference between GPS and GLONASS is that the GPS satellites are all using different PRN codes on the same frequency, whereas the GLONASS satellites all use the same PRN code but slightly different frequencies. The small frequency differences give rise to complexity in the processing of the carrier phase data. Contrary to GPS all GLONASS satellites are equipped with a laser retroreflector array and may therefore be observed by the ground station tracking network of the International Laser Ranging Service (ILRS). For more information about GLONASS we refer to *Habrich* [1999].

2.3 The Observation Equations

We only review the most important aspects of the observation equations for GPS. For more information we refer to, e.g., [*Leick*, 1995; *Kleusberg and Teunissen*, 1996]. Let us use the following notation:

k ... Index of a particular receiver.
i ... Index of a particular transmitter.
t ... Signal reception time (GPS time).
t_k ... Reading of the receiver clock at signal reception time.
δ_k ... Error of the receiver clock at time t with respect to GPS time. The signal reception time t may be written as: $t = t_k - \delta_k$.
τ ... Signal traveling time between satellite and receiver.
δ^i ... Error of the satellite clock at time $t - \tau$ w.r.t. GPS time.
$\vec{r}_k(t)$ ... Position of receiver k at signal reception time t.

$\vec{r}^{\,i}(t-\tau)$ ... Position of the satellite i at signal emission time $t-\tau$.
ϱ_k^i ... Geometrical distance between satellite i (at signal emission time $t-\tau$) and receiver k (at signal reception time t), also called "slant range".

2.3.1 Code Observation Equation

Using the known codes provided on the GPS carriers, the GPS receivers measure the so-called pseudo-range:

$$P_k^i = c\,((t+\delta_k) - (t-\tau+\delta^i)) \tag{2.1}$$

"pseudo", because of the biases introduced by the satellite and receiver clock errors. Using the geometrical distance ϱ_k^i the code observation equation, in its simplest form, may be written as:

$$P_{Fk}^i = \varrho_k^i + c\,\delta_k - c\,\delta^i \tag{2.2}$$

where:

P_F ... Code measurement at frequency *F*.

Note that both terms, $c\,\delta_k$ and $c\,\delta^i$, depend on the frequency *F* due to the different location of the phase centers of both, transmitter and receiver.

2.3.2 Phase Observation Equation

The GPS receiver measures the difference between two phases. The observation equation may be written as follows:

$$\psi_{Fk}^i(t) = \phi_{Fk}(t) - \phi_F^i(t-\tau) + n_{Fk}^i \tag{2.3}$$

where:

$\psi_{Fk}^i(t)$ ... Phase measurement (in cycles) at epoch t and frequency *F*.
$\phi_{Fk}(t)$ ... Phase of the signal generated by the receiver oscillator at reception time t.
$\phi_F^i(t-\tau)$ ... Phase of the signal generated by the satellite oscillator at emission time $t-\tau$.
n_{Fk}^i ... Unknown integer number of cycles (the so-called initial phase ambiguity).

Using a Taylor series development truncated after the terms of first order we may rewrite this as:

$$\psi_{Fk}^i(t) = \phi_{Fk}(t) - \phi_F^i(t) + \tau\,f_F + n_{Fk}^i \tag{2.4}$$

where f_F is the frequency of the carrier signal. Taking into account the receiver clock error δ_k and the satellite clock error δ^i the phase difference may be written as:

$$\phi_{Fk}(t) - \phi_F^i(t) = (\delta_k - \delta^i)\,f_F$$

The observation equation is then given by:

$$\psi_{Fk}^i(t) = (\delta_k - \delta^i)\,f_F + \tau\,f_F + n_{Fk}^i \tag{2.5}$$

Multiplying this equation by the wavelength λ_F of the carrier we obtain the phase observation equation:

$$L^i_{Fk} = \varrho^i_k + c\,\delta_k - c\,\delta^i + \lambda_F\, n^i_{Fk} \tag{2.6}$$

2.3.3 Measurement Delays

Phase measurements and code pseudo-ranges are affected by both, systematic and random effects. Let us mention, e.g., satellite orbit errors, clock errors, propagation effects, receiver clock errors, relativistic effects, antenna phase center variations, and multipath. Let us address three effect, namely tropospheric and ionospheric refraction, and the relativistic effect.

T^i_k … Tropospheric refraction, i.e., the signal delay due to the neutral (i.e., the non-ionized) part of the Earth's atmosphere. It is important that the tropospheric refraction, in the GHz region, does not depend on the frequency and that the effect is the same for code and phase measurements.

I^i_k … Ionospheric refraction, i.e., the signal delay respectively phase advance due to the free electrons in the Earth's atmosphere. The ionosphere is a dispersive medium for microwave signals, which means that the refractive index for GPS signals is frequency-dependent.

δ^i_r … Relativistic correction. The atomic frequency standards in the GPS satellites are "affected" by general (gravity) and special relativity (the satellite's velocity). The predominant portion of these relativistic effects is constant and, due to their common height, common to all GPS satellites. The effect is that the clocks in orbit appear to run faster by about 40 μs per day. This constant part is corrected for by adjusting the frequency of the oscillators of the GPS satellites prior to launch by -0.00455 Hz. The remaining part of the effect, caused by the eccentricity of the orbit, is often called the periodic relativistic effect.

The periodic relativistic effect is not commonly used in the GPS observation equations because it is satellite-dependent and therefore cancels in the single difference between stations. However, it is important if stations and/or satellite clocks are estimated, e.g., when applying undifferenced processing techniques and for absolute navigation. The effect, which may reach up to about 50 ns (15 m), is easily computed by the formula:

$$\begin{aligned}\delta^i_r &= F \cdot \sqrt{a} \cdot e \cdot \sin(E) \\ &= \frac{-2 \cdot \vec{r}^{\,i} \cdot \dot{\vec{r}}^{\,i}}{c^2}\end{aligned}$$

with:

$$F = \frac{-2\sqrt{GM}}{c^2} = -4.4428 \cdot 10^{-10} \frac{s}{\sqrt{m}}$$

where:

G ... Newtonian gravitational constant.
M ... Total mass of the Earth.
GM ... Product of G and M ($398600.4415 \cdot 10^9 \; m^3/s^2$).
e ... Eccentricity of the satellite orbit.
a ... Semi-major axis of the satellite orbit.
E ... Eccentric anomaly of the satellite.
$\vec{r}^{\,i}$ ... Geocentric position vector of satellite i.
$\dot{\vec{r}}^{\,i}$ ... Geocentric velocity vector of satellite i.
c ... Velocity of light.

Taking into account these three effects the observation equations (2.2) and (2.6) for both frequencies and both types of measurements (code and phase) may be refined as:

$$
\begin{aligned}
L^i_{1k} &= \varrho^i_k - I^i_k + T^i_k - c\,\delta^i_r + c\,\delta_k - c\,\delta^i + \lambda_1\, n^i_{1k} \\
L^i_{2k} &= \varrho^i_k - \frac{f_1^2}{f_2^2}\, I^i_k + T^i_k - c\,\delta^i_r + c\,\delta_k - c\,\delta^i + \lambda_2\, n^i_{2k} \\
P^i_{1k} &= \varrho^i_k + I^i_k + T^i_k - c\,\delta^i_r + c\,\delta_k - c\,\delta^i \\
P^i_{2k} &= \varrho^i_k + \frac{f_1^2}{f_2^2}\, I^i_k + T^i_k - c\,\delta^i_r + c\,\delta_k - c\,\delta^i
\end{aligned}
\tag{2.7}
$$

2.4 Forming Differences

We may form differences of the original observation equations in order to eliminate some of the effects in eqns. (2.7). Elimination of the biases has the advantage that the number of unknown parameters may be reduced significantly. However, the consequence is that no estimates for the eliminated parameters will be available like, e.g., satellite and station clocks.

2.4.1 Single Differences

The single difference is a linear combination of two measurements. There are three different kinds of single differences:

Between stations: Difference between two simultaneous measurements of the same satellite from two different receivers. In this single difference the satellite specific terms (δ^i and δ^i_r) are almost eliminated.

Between satellites: Difference between two simultaneous measurements from one receiver to two different satellites. In this single difference the receiver clock error (δ_k) is eliminated.

Between epochs: Difference between two measurements from one receiver of one satellite at two different epochs. In this single difference the ambiguity (n^i_k) is eliminated.

2.4.2 Double Differences

A double difference is a linear combination of four simultaneous measurements or the linear combination of two single difference measurements. Although other combinations may make sense, a double difference usually consist of the linear combination of two single differences between stations for two different satellites at the same epoch. Figure 2.4 shows the geometry of a typical double difference. In this double difference observation both, the station and satellite specific effects (δ^i, δ^i_r, and δ_k), are eliminated or at least greatly reduced. This double difference is the basic observation used in the Bernese software for precise parameter estimation. It is defined by:

$$L^{ij}_{Fkl} = (L^i_{Fk} - L^i_{Fl}) - (L^j_{Fk} - L^j_{Fl}) \tag{2.8}$$

The corresponding observation equations are:

$$\begin{aligned}
L^{ij}_{1kl} &= \varrho^{ij}_{kl} - I^{ij}_{kl} + T^{ij}_{kl} + \lambda_1\, n^{ij}_{1kl} \\
L^{ij}_{2kl} &= \varrho^{ij}_{kl} - \frac{f_1^2}{f_2^2}\, I^{ij}_{kl} + T^{ij}_{kl} + \lambda_2\, n^{ij}_{2kl} \\
P^{ij}_{1kl} &= \varrho^{ij}_{kl} + I^{ij}_{kl} + T^{ij}_{kl} \\
P^{ij}_{2kl} &= \varrho^{ij}_{kl} + \frac{f_1^2}{f_2^2}\, I^{ij}_{kl} + T^{ij}_{kl}
\end{aligned} \tag{2.9}$$

2.5 Relevant Linear Combinations and their Characteristics

It is often useful to form linear combinations of the original carrier phase and/or code measurements. This may be done on any differencing level. Let L_1 and L_2 represent the phase observables, and P_1 and P_2 the code observables, both in meters. The main disadvantage of forming linear combinations is the increased noise of the linear combination as compared to that of the original measurements. A general linear combination may be written as:

$$L_{LC} = \alpha \cdot L_1 + \beta \cdot L_2 \tag{2.10}$$

with real coefficients α and β. The noise of the linear combination may be written as:

$$\sigma_{LC} = \sqrt{\alpha^2 + \beta^2} \cdot \sigma_0 \tag{2.11}$$

where it is assumed that the original measurements, L_1 and L_2, both had the same noise σ_0. The relevant linear combinations are discussed in the next sections, their characteristics are summarized in Table 2.3.

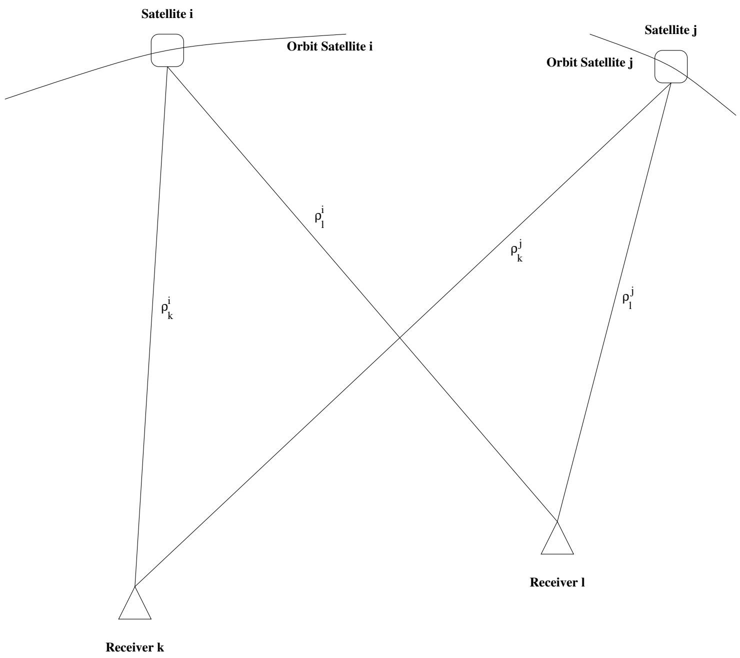

Figure 2.4: Geometry of a typical double difference observation.

2.5.1 The Ionosphere-free Linear Combination

The linear combination of type (2.10) with the coefficients:

$$\alpha = \frac{f_1^2}{f_1^2 - f_2^2} \quad \text{and} \quad \beta = \frac{-f_2^2}{f_1^2 - f_2^2}$$

yielding:

$$L_3 = \frac{1}{f_1^2 - f_2^2} \left(f_1^2 \; L_1 - f_2^2 \; L_2 \right) \tag{2.12}$$

is often called "ionosphere-free" because the ionospheric path delay is practically eliminated. The same is true for the corresponding combination of code measurements:

$$P_3 = \frac{1}{f_1^2 - f_2^2} \left(f_1^2 \; P_1 - f_2^2 \; P_2 \right) \tag{2.13}$$

Taking into account the double difference phase measurements and neglecting tropospheric refraction T_{kl}^{ij} in eqn. (2.9) the ionosphere-free linear combination has the form:

$$L_{3kl}^{ij} = \varrho_{kl}^{ij} + B_{3kl}^{ij} \tag{2.14}$$

where the ionosphere-free bias B_{3kl}^{ij} may be written as:

$$B_{3kl}^{ij} = \frac{1}{f_1^2 - f_2^2} \left(f_1^2 \lambda_1 n_{1kl}^{ij} - f_2^2 \lambda_2 n_{2kl}^{ij} \right) \tag{2.15}$$

This bias cannot be expressed in the form $\lambda_3 \, n^{ij}_{3kl}$, where n^{ij}_{3kl} is an integer ambiguity. If we know the difference $n^{ij}_{5kl} = n^{ij}_{1kl} - n^{ij}_{2kl}$ (the so-called wide-lane ambiguity), however, the ionosphere-free bias B^{ij}_{3kl} may be written as:

$$B^{ij}_{3kl} = c \, \frac{f_2}{f_1^2 - f_2^2} \, n^{ij}_{5kl} + \underbrace{\frac{c}{f_1 + f_2}}_{\lambda_3} \, n^{ij}_{1kl} \tag{2.16}$$

where the first term on the right-hand side is known. The artificial wavelength λ_3 is only about 11 cm. For obvious reasons the unknown ambiguity n^{ij}_{1kl} in eqn. (2.16) is often called narrow-lane ambiguity.

2.5.2 The Geometry-free Linear Combination

The linear combination of type (2.10) with the coefficients:

$$\alpha = 1 \ \text{ and } \ \beta = -1$$

yields:

$$L_4 = L_1 - L_2 \tag{2.17}$$

It is independent of receiver and satellite clocks and geometry (orbits, station coordinates). It only contains the ionospheric delay and the initial phase ambiguities. It is well suited for the estimation of ionosphere models and for cleaning undifferenced data. The same linear combination may be applied to the code observations.

2.5.3 The Wide-lane Linear Combination

The linear combination of type (2.10) with the coefficients:

$$\alpha = \frac{f_1}{f_1 - f_2} \ \text{ and } \ \beta = \frac{-f_2}{f_1 - f_2}$$

gives:

$$L_5 = \frac{1}{f_1 - f_2} \, (f_1 \, L_1 - f_2 \, L_2) \tag{2.18}$$

It is often used for phase observations for the purpose of cycle slip detection and ambiguity resolution on the double difference level. Using eqn. (2.9) and neglecting both, ionospheric refraction I^{ij}_{kl} and tropospheric refraction T^{ij}_{kl}, we obtain:

$$L^{ij}_{5kl} = \varrho^{ij}_{kl} + \underbrace{\frac{c}{f_1 - f_2}}_{\lambda_5} \, \underbrace{(n^{ij}_{1kl} - n^{ij}_{2kl})}_{n^{ij}_{5kl}} \tag{2.19}$$

Carrier	Description	Wavelength	Noise rel to L_1	Ionosphere rel to L_1
L_1	Actual Carrier	19 cm	1	1
L_2	Actual Carrier	24 cm	1	1.6
L_3	Ionosphere-free LC	0 cm	3	0
L_4	Geometry-free LC	∞	1.4	0.6
L_5	Wide Lane	86 cm	5	1.3
L_6	Melbourne-Wüebbena	86 cm	-	0

Table 2.3: Linear combinations of the L_1 and L_2 observables. L_3–L_6 are the naming convention of the Bernese GPS Software package.

The artificial wavelength λ_5 is about 86 cm and is approximately four times longer than λ_1 and λ_2. Therefore, this linear combination is called the wide-lane and the ambiguity:

$$n_{5kl}^{ij} = n_{1kl}^{ij} - n_{2kl}^{ij} \tag{2.20}$$

is called the wide-lane ambiguity.

2.5.4 The Melbourne-Wübbena Linear Combination

The Melbourne-Wübbena combination is a linear combination of both, carrier phase (L_1 and L_2) and P-code (P_1 and P_2) observations described by [*Wübbena*, 1985] and [*Melbourne*, 1985]. This combination eliminates the effect of the ionosphere, the geometry, the clocks, and the troposphere. The combination is given by:

$$L_6 = \frac{1}{f_1 - f_2}\,(f_1\;L_1 - f_2\;L_2) - \frac{1}{f_1 + f_2}\,(f_1\;P_1 + f_2\;P_2) \tag{2.21}$$

For double difference observations we obtain:

$$L_{6kl}^{ij} = \lambda_5\;n_{5kl}^{ij} \tag{2.22}$$

With good P-code data (RMS $\leq$ 1 m) this linear combination may be used for the resolution of the wide-lane ambiguities n_{5kl}^{ij}. On the undifferenced (zero difference) level the same linear combination gives:

$$L_{6k}^{i} = \lambda_5\;n_{5k}^{i} \tag{2.23}$$

which means that this linear combination may be used to check zero difference observations for cycle-slips. Note that only the difference $n_{1k}^{i} - n_{2k}^{i}$ can be checked in this way.

3 Modeling the Observables

3.1 Definitions of the Time Systems

There are three different systems of time in common use [*Seidelmann*, 1992]:

Dynamical Time: The independent argument in the equation of motions. When we generate ephemerides for GPS satellites, we implicitly use (terrestrial) dynamical time.

Atomic Time: The time realized through atomic clocks on the Earth's surface. It is the basis for a uniform time scale on the Earth. The atomic time scale is defined by the frequency of the basic oscillation of the frequency-determining element. The origin of the time scale is defined by international convention.

Sidereal Time: The time defined through the rotation of the Earth. Although once used as a measure of time by means of astronomical observations, it is much to irregular by today's standards.

3.1.1 Dynamical Time

Dynamical time is required to describe the motion of bodies in a particular reference system and according to a particular gravitational theory. Today, general relativity and an inertial reference system are fundamental concepts. The best possible inertial reference frame we can access has its origin in the center of mass of the solar system (barycenter). Dynamical time associated with this system is called Barycentric Dynamical Time (TDB, as for most other time scales the abbreviation reflects the French order of the words). A clock fixed on Earth will exhibit periodic variations as large as 1.6 ms with respect to TDB due to the motion of the Earth in the gravity field of the Sun. However, in describing the orbital motion of near-Earth satellites we need not use TDB, nor account for these relativistic variations, because both, the satellite and the Earth, are subject to nearly the same perturbations. For near-Earth satellite orbit computations we may use Terrestrial Dynamical Time (TDT), which represents a uniform time scale for motions within the gravity field of the Earth.

3.1.2 Atomic Time

The fundamental time scale for time keeping on Earth is the International Atomic Time (TAI). It results from analyses by the "Bureau International des Poids et Mesures" (BIPM) in Paris, France, using data from atomic standards of many countries. It is a continuous time scale and serves in practice to define TDT:

$$\mathrm{TDT} = \mathrm{TAI} + 32.184\ s$$

There is a fundamental problem of using TAI in practice; the rotation of the Earth around its spin axis is slowing down. Thus TAI would eventually become inconveniently out of synchronization with the solar day. This problem has been overcome by introducing Coordinated Universal Time (UTC), which runs at the same rate as TAI but is incremented by leap seconds when necessary. Normally these leap seconds are introduced at on January 1^{st} or July 1^{st} but they may also be introduced on March 1^{st} and September 1^{st}.

Each of the worlds time laboratories keeps a local realization of UTC. All these local realizations of UTC have to be synchronized. The technique to inter-compare and synchronize different frequency standards is called "time transfer". Time transfer currently depends very much on GPS using the so-called "common-view" technique. Time transfer will be addressed in Chapter 8.

GPS System Time

All the clocks on board the GPS satellites have to be tuned to GPS time. Because of the independence of the satellite clocks very precise synchronization is mandatory to give accurate point positioning. This can only be accomplished by using atomic clocks. Therefore all the GPS satellites are equipped with a set of two cesium and two rubidium frequency standards. For comparison, the GLONASS satellites are equipped with three cesium standards. The GPS system time is given by its "Composite Clock (CC)". The CC or "paper" clock consists of all operational monitoring stations and satellite frequency standards. GPS system time, in turn, is referenced to the Master Clock (MC) at the USNO and steered to UTC(USNO) from which GPS time will not deviate by more than one microsecond. The exact difference is contained in the navigation message in the form of two constants, A0 and A1, giving the time difference and rate of GPS time w.r.t. UTC(USNO,MC). UTC(USNO) itself is kept very close to the international standard UTC(BIPM), and the exact difference is available in near real time. GPS time was aligned to UTC on 6 January 1980 and is not incremented by leap seconds. Therefore, the two time scales differ by an integer number of seconds. By definition, there is a constant offset of 19 seconds between the GPS and TAI time scales, that is, at any instant we have:

$$\mathrm{GPS} = \mathrm{TAI} - 19\ s$$

Figure 3.1 shows the relationship between the time scales.

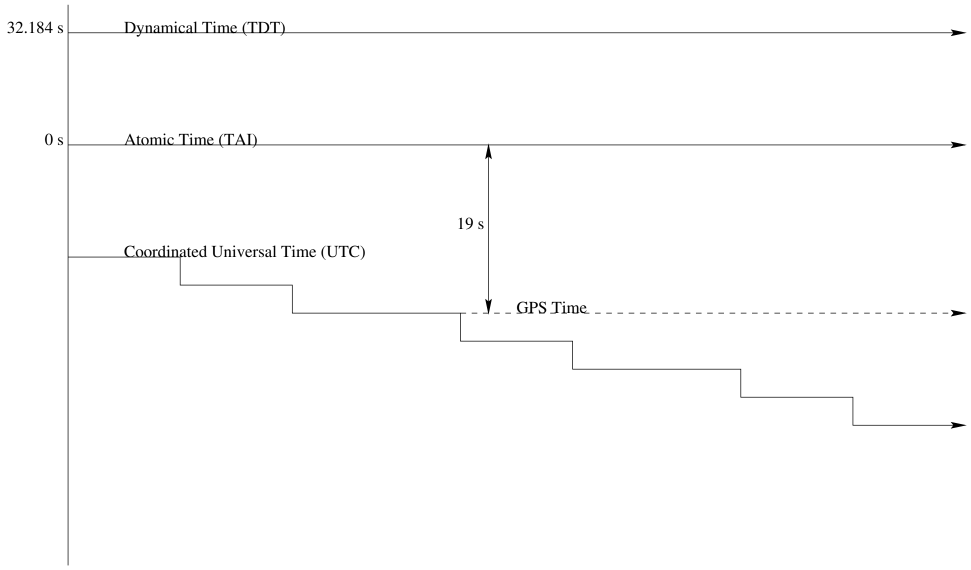

Figure 3.1: The relationship between time scales.

3.2 Reference Systems

3.2.1 Terrestrial Reference System

The distance between the receiver and the satellite is the most important constituent of the range measured by GPS receivers. The receiver position is given in a Terrestrial Reference System (TRS) which meets the following criteria [*McCarthy*, 1996]:

- It is geocentric, the center of mass being defined for the whole Earth, including oceans and atmosphere.
- Its scale is that of a local Earth frame, in the meaning of a relativistic theory of gravitation.
- Its orientation was initially given by the BIH orientation of 1984.0.
- Its time evolution in orientation shall create no residual global rotation with regard to the crust.

A Conventional Terrestrial Reference System (CTRS) is realized through a set of coordinates for a network of stations. The CTRS, which is monitored by the International Earth Rotation Service (IERS), is called the International Terrestrial Reference System (ITRS). Realizations of the ITRS are produced by the IERS under the name International Terrestrial Reference Frame (ITRF). Currently the ITRF realizations of the ITRS are done annually. In the designation ITRF-yy the “yy” specifies the last year of which data were used in the formation of the frame. Hence ITRF-96 designates the frame of coordinates and velocities constructed in 1997 using all of the IERS data available through 1996.

3.2.2 Celestial Reference System

The equations of motion for a (artificial) satellite have the most convenient form if expressed in a Celestial Reference System (CRS). The celestial reference system is realized by a celestial reference frame defined by the precise coordinates of extra-galactic radio sources with its origin at the barycenter of the solar system and the directions of the axes fixed with respect to the quasars. In compliance with this, the IERS CRS is realized by the IERS CRF defined by the J2000.0 equatorial coordinates of extra-galactic objects determined from Very Long Baseline Interferometry (VLBI) observations. The catalog of source coordinates published in the IERS Annual Reports provides access to the ICRS. The direct access to the quasars is most precise through VLBI observations, a technique which is not readily available to users. Therefore, while VLBI is used for the maintenance of the frame, the tie of the ICRF to the major practical reference frames may be obtained through use of the IERS Terrestrial Reference Frame and the JPL ephemerides of the solar system. The IERS Earth orientation parameters provide the permanent tie of the ICRF to the ITRF.

3.2.3 Transformation between the Celestial and Terrestrial System

The coordinate transformation to be used to go from the TRS to the CRS at the epoch t of the observation can be written as [*McCarthy*, 1996]:

$$[\mathrm{CRS}] = \mathrm{P}^{\mathrm{T}}(\mathrm{t})\mathrm{N}^{\mathrm{T}}(\mathrm{t})\mathrm{R}^{\mathrm{T}}(\mathrm{t})\mathrm{W}^{\mathrm{T}}(\mathrm{t})[\mathrm{TRS}] \tag{3.1}$$

where:

$P^T(t)$	...	Transformation matrix corresponding to the precession between the reference epoch and the epoch t.
$N^T(t)$	...	Transformation matrix corresponding to the nutation at epoch t.
$R^T(t)$	...	Transformation matrix arising from the rotation of the Earth around the axis of the CEP.
$W^T(t)$	...	Transformation matrix arising from polar motion.
$[\mathrm{CRS}]$	...	Vector in the Celestial Reference System.
$[\mathrm{TRS}]$	...	Vector in the Terrestrial Reference System.

The transformation matrix arising from polar motion is:

$$W^T(t) = R_1(y_p) \cdot R_2(x_p) \tag{3.2}$$

where x_p and y_p are the "polar coordinates" of the CEP in the TRS. The transformation matrix arising from the rotation of the Earth around the axis of the CEP has the form:

$$R^T(t) = R_3(-GST) \tag{3.3}$$

where GST is the Greenwich True Sidereal Time at epoch t.

3.3 The Station Model

The origin of the terrestrial reference system is the geocenter of the Earth's masses. However, the Earth's crust may move relative to the Earth's center of mass. This translational motion is known as "geocenter motion". It is caused by the mass movement of planetary fluids, primarily the atmosphere and oceans. The position of a point located on the surface of the solid Earth, relative to the Earth's center of mass, may be expressed by [*McCarthy*, 1996]:

$$\vec{X}(t) = \vec{X}_0 + \vec{V}_0(t - t_0) + \sum_i \Delta\vec{X}_i(t) - \vec{X}_{gc}(t) \tag{3.4}$$

where:

$\vec{X}(t)$	...	Position vector relative to the Earth's center of mass at time t.
$\vec{X}_0$	...	Position vector at epoch t_0.
$\vec{V}_0$	...	Velocity vector at epoch t_0.
$\vec{X}_i(t)$	...	Corrections, at time t, due to various time changing effects.
$\vec{X}_{gc}(t)$	...	The instantaneous vector translation of the Earth's center of mass (including oceans and atmosphere) at time t, relative to its long-term time-averaged position.

The time changing effects on the station position are, e.g., solid Earth tidal displacements, ocean tidal loading, polar loading, post-glacial rebound, atmospheric loading.

The set of positions ($\vec{X}_0$) and velocities ($\vec{V}_0$) at epoch t_0 constitutes the ITRF. The origin of this system is defined to be the long-term time-averaged position of the Earth's center of mass (including oceans and atmosphere). In GPS data analyses these positions and velocities ($\vec{X}_0$, $\vec{V}_0$) are usually solve-for parameters. In global GPS analyses we may also solve for the geocenter offset and/or variations ($\vec{X}_{gc}$).

3.4 The Satellite Orbit Model

Only a basic introduction to satellite orbit modeling is presented here. It is based on [*Beutler*, 1990*b*, 1990*a*, 1991; *Beutler et al.*, 1996*a*; *Rothacher*, 1992, 1996], which may serve for further reference.

3.4.1 Equations of Motion

The equations of motion of an artificial Earth satellite may be written as:

$$\ddot{\vec{r}} = -GM \cdot \frac{\vec{r}}{r^3} + \vec{a}(t, \vec{r}, \dot{\vec{r}}, q_1, q_2, q_3, \ldots, q_m) \tag{3.5}$$

where the first term represents the central gravity term and $\vec{a}$ the total perturbing acceleration with:

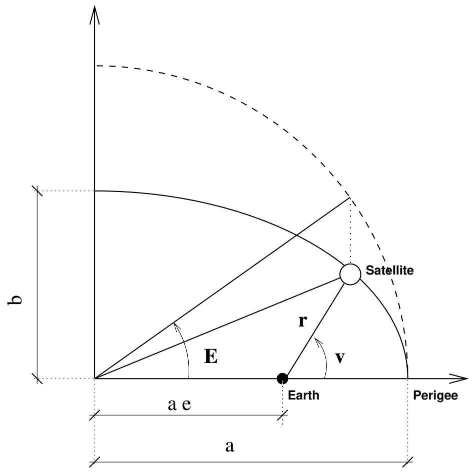

(a) Semi-major axis a, eccentricity e, eccentric E, and true ν anomaly

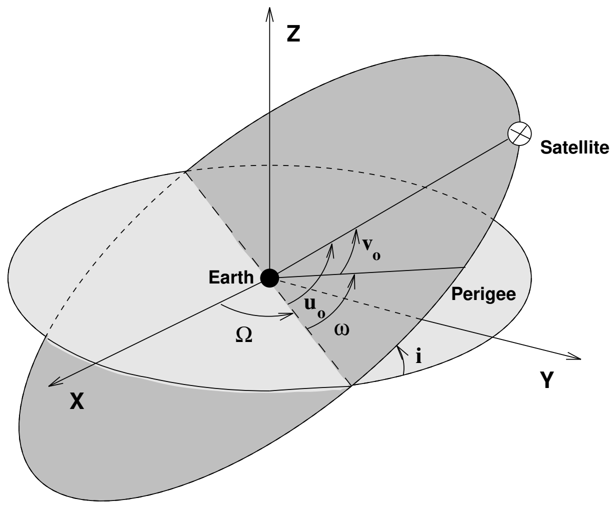

(b) Ascending node Ω, inclination i, argument of perigee ω, and the argument of latitude u_0 of the Satellite in the orbital plane

Figure 3.2: Definition of the Keplerian elements.

G	…	Newtonian gravitational constant.
M	…	Total mass of the Earth.
GM	…	Product of G and M ($398600.4415 \cdot 10^9 m^3 s^{-2}$).
$\vec{r}$	…	Position vector of the satellite with respect to the center of mass of the Earth.
q_n	…	Dynamical parameters (e.g., solar radiation pressure parameters).

We may also write:

$$\ddot{\vec{r}} = \vec{f}(t, \vec{r}, \dot{\vec{r}}, q_1, q_2, q_3, \dots, q_m) \tag{3.6}$$

These equations of motion (3.5 or 3.6) do not define a unique orbit (particular solution of the equations of motion). We have to specify in addition, e.g., the so-called initial conditions at a time t_0:

$$\vec{r}(t_0) = \vec{r}_0 \ , \ \dot{\vec{r}}(t_0) = \dot{\vec{r}}_0 \tag{3.7}$$

This second order differential equation system, in general, cannot be solved analytically, because the function $\vec{f}$ may be very complicated. Therefore, numerical integration algorithms have to be used.

In satellite geodesy, we are mainly interested in elliptic orbits which may be characterized by the six Keplerian elements, see Figure 3.2. All six Keplerian elements, at epoch t, may be computed from the position vector $\vec{r}(t)$ and the velocity vector $\dot{\vec{r}}(t)$, see, e.g., [*Beutler et al.*, 1996*a*].

The perturbation term $\vec{a}$ is small compared to the two-body term (or central gravity term) and the solution of the unperturbed equations is therefore a good approximation to the perturbed solution, at least in the vicinity of the initial epoch t_0. It therefore makes sense to introduce for each epoch t an instantaneous ellipse and to speak of the Keplerian elements as evolving in time. Let us assume that $\vec{r}(t)$ and $\dot{\vec{r}}(t)$ are the true position and velocity vectors for each time argument t as they are computed from the equations of motion (3.6). The osculating elements at time t are then defined as the Keplerian elements computed from $\vec{r}(t)$ and $\dot{\vec{r}}(t)$. In this way we get time series of osculating elements $a(t)$, $e(t)$, $i(t)$, $\Omega(t)$, $\omega(t)$, and $T_p(t)$ (perigee passing time).

3.4.2 Orbit Improvement

Orbit determination in its general sense is the problem of determining the following $n = 6+m$ unknown parameters p_i that define a unique (particular) solution of the above set of three equations:

$$\{p_1, p_2, \ldots, p_n\} = \{a, e, i, \Omega, \omega, T_p, q_1, q_2, \ldots, q_m\} \tag{3.8}$$

The six Keplerian elements at time t_0 define the initial conditions of the problem. Instead of the Keplerian elements it would be possible, as well, to set up the components of the vectors $\vec{r}(t_0) = \vec{r}_0$ and $\dot{\vec{r}}(t_0) = \dot{\vec{r}}_0$ as unknowns. The parameters $q_1, q_2, \ldots, q_m$ are the unknown dynamical parameters describing the accelerations acting on the satellite. All the parameters p_i $(i = 1, 2, \ldots, n)$ refer to a certain time interval $[t_0, t_1]$ which is identical with the time interval containing all observations used to establish the orbital parameters. If we only consider the solution in this time interval, we speak of a satellite arc with an arc length $l = t_1 - t_0$.

When we have to determine the orbits of GPS satellites, we may consider most of the parameters $q_1, q_2, \ldots, q_m$ defining the force field to be known very accurately. The coefficients of the gravity field, e.g., are known with high precision from Satellite Laser Ranging solutions. It is not possible, however, to assume all dynamical parameters to be known, e.g., the solar radiation pressure. Let us assume that we have an approximate a priori orbit available. This a priori orbit $\vec{r}_0(t)$ must be a solution of the same equations of motion with approximate values $(\vec{r}_0, \dot{\vec{r}}_0, q_{10}, \ldots, q_{m0})$ for the same set of parameters:

$$\ddot{\vec{r}}_0 = -GM \cdot \frac{\vec{r}_0}{r_0^3} + \vec{a}(t, \vec{r}_0, \dot{\vec{r}}_0, q_{10}, \ldots, q_{m0}) \tag{3.9}$$

$$\vec{r}_0(t_0) = \vec{r}(a_0, e_0, i_0, \Omega_0, \omega_0, T_{p0}; t_0) \tag{3.10}$$

$$\dot{\vec{r}}_0(t_0) = \dot{\vec{r}}(a_0, e_0, i_0, \Omega_0, \omega_0, T_{p0}; t_0) \tag{3.11}$$

where a_0, e_0, i_0, Ω_0, ω_0, T_{p0} and q_{i0} are the approximate values p_{i0} of the unknown parameters p_i. We may now linearize the unknown orbit $\vec{r}(t)$ by developing it into a Taylor series which we truncate after the linear terms:

$$\vec{r}(t) = \vec{r}_0(t) + \sum_{i=1}^{n} \frac{\partial \vec{r}_0(t)}{\partial p_i} \cdot (p_i - p_{i0}) \tag{3.12}$$

The unknown orbit $\vec{r}(t)$ is thus represented as a linear function of the unknown parameters p_i $(i = 1, 2, \ldots, n)$. To set up a least squares algorithm we need to compute the partial derivatives in eqn. (3.12). Let us first introduce the following symbol for the partial derivative of the orbit with respect to one orbit parameter $p \in \{p_1, p_2, \ldots, p_n\}$:

$$\vec{z}(t) = \frac{\partial \vec{r}_0(t)}{\partial p} \tag{3.13}$$

Taking the total derivative of the equations of motion (3.9) with respect to the parameter p, we obtain a differential equation system for the partial derivatives $\vec{z}(t)$:

$$\ddot{\vec{z}} = \mathbf{A}_0 \cdot \vec{z} + \mathbf{A}_1 \cdot \dot{\vec{z}} + \vec{a}_p \tag{3.14}$$

where $\mathbf{A}_0$ and $\mathbf{A}_1$ are 3x3 matrices with elements defined by:

$$\mathbf{A}_{0,ik} = \frac{\partial f_i}{\partial r_{0,k}} \qquad i, k = 1, 2, 3 \tag{3.15}$$

$$\mathbf{A}_{1,ik} = \frac{\partial f_i}{\partial \dot{r}_{0,k}} \qquad i, k = 1, 2, 3 \tag{3.16}$$

and:

$$\vec{a}_p = \frac{\partial \vec{a}}{\partial p} \tag{3.17}$$

We used f_i here to denote the components of the vector function $\vec{f}$ in eqn. (3.6). All the partials have to be evaluated using the known a priori orbit $\vec{r}_0(t)$. Equations (3.14) are called the variational equations (one for each parameter p_i) belonging to the original equations of motions (3.9), also called the primary equations in this context. The initial conditions for the variational equations (3.14) may be obtained by taking the partial derivatives of the initial conditions (3.10) of the primary system with respect to the unknown parameter p:

$$\vec{z}(t_0) = \frac{\partial \vec{r}_0(t_0)}{\partial p} \qquad \dot{\vec{z}}(t_0) = \frac{\partial \dot{\vec{r}}_0(t_0)}{\partial p} \tag{3.18}$$

For $p \in \{a, e, i, \Omega, \omega, T_p\}$ we have:

$$\vec{a}_p = \vec{0}, \qquad \vec{z}(t_0) \neq \vec{0}, \qquad \dot{\vec{z}}(t_0) \neq \vec{0} \tag{3.19}$$

whereas for $p \in \{q_1, q_2, \ldots, q_d\}$ we have:

$$\vec{a}_p \neq \vec{0}, \qquad \vec{z}(t_0) = \vec{0}, \qquad \dot{\vec{z}}(t_0) = \vec{0} \tag{3.20}$$

In summary we may say, that in an orbit improvement step we have to solve, in addition to the non-linear primary equations (3.9, 3.10), one linear differential equation system (3.14, 3.18) for each orbit parameter p_i to obtain the partial derivatives $\vec{z}(t)$ of the orbit $\vec{r}(t)$ w.r.t. the parameters p_i. All these differential equation systems have to be solved using numerical integration methods, [*Beutler*, 1998]. Let us also mention that because at present no velocity dependent forces are modeled for the GPS satellite orbits we may assume that:

$$\mathbf{A}_{1,ik} = 0 \qquad i, k = 1, 2, 3 \tag{3.21}$$

3.4.3 Accelerations Acting on the GPS Satellites

Let us now have a closer look at the second term $\vec{a}$ on the right hand side of the equations of motion (3.5). This perturbing acceleration is composed of:

$$\vec{a} = \vec{a}_{NS} + \vec{a}_{MS} + \vec{a}_{TID} + \vec{a}_{RPR} + \vec{a}_{rest} \tag{3.22}$$

where the various accelerations are due to:

$\vec{a}_{NS}$ ... Non-sphericity of the Earth gravity potential.
$\vec{a}_{MS}$ ... Gravitational acceleration due to the Moon and the Sun.
$\vec{a}_{TID}$ ... Earth tidal potential.
$\vec{a}_{RPR}$ ... Solar radiation pressure.
$\vec{a}_{rest}$ ... Sum of all remaining small accelerations ($< 10^{-9} m/s^2$).

Table 3.1 summarizes the order of magnitude of the various perturbing accelerations acting on the GPS satellites. Two different approaches were chosen to study the magnitude of the accelerations. First, a reference orbit was generated by integrating a given set of osculating Keplerian elements over a time period of three days (72 hours) using a standard orbit model. For this purpose the full GPS satellite constellation of January 1, 1998 was used.

For the first approach the same set of osculating Keplerian elements was integrated over the same time period of three days with the respective acceleration turned off. Consequently the RMS difference between this perturbed orbit and the reference orbit over the full 72-hour arc-length was computed and is shown in the left half of Table 3.1. In the second approach the positions of the perturbed orbit were used as pseudo-observations in an orbit determination process where we again used the same standard orbit model which was used for the generation of the "reference orbit". In this orbit estimation step we characterize each orbit by 11 parameters; six for the initial conditions and five for the solar radiation pressure. These are the same parameters we currently use for our routine GPS orbit computations. Consequently the RMS difference between this fit through the perturbed orbit and the perturbed orbit over the full 72 hour arc-length was computed and is also shown in Table 3.1.

Perturbing Acceleration	RMS orbit difference over 3 days Radial	Along	Cross	Total	RMS of orbit determination Radial	Along	Cross	Total
	units: meters				units: meters			
Earth oblateness (C_{20})	1341	36788	18120	41030	1147	1421	6841	7054
Moon (gravitation)	231	3540	1079	3708	87	126	480	504
Sun (gravitation)	83	1755	431	1809	30	13	6	33
C_{22} S_{22}	80	498	10	504	3	3	4	5
C_{nm} S_{nm} (n,m=3..8)	11	204	10	204	4	13	5	15
C_{nm} S_{nm} (n,m=4..8)	2	41	1	41	1	2	1	2
C_{nm} S_{nm} (n,m=5..8)	1	8	0	8	0	0	0	0
	units: meters				units: millimeters			
Solar Radiation Pressure	90	258	4	273	0	1	1	2
	units: millimeters				units: millimeters			
Fixed body tides	46	1382	225	1400	16	28	80	87
Relativistic Effects	17	584	0	585	4	1	1	5
Ocean Tides	12	221	22	223	4	11	8	14
Venus, Jupiter, Mars (grav.)	8	157	44	164	3	3	13	13

Table 3.1: Effect of different perturbations on a GPS satellite over 3 days.

4 The International GPS Service and its Products

4.1 The International GPS Service

Over the last decade GPS started playing a major role in regional and global studies of the Earth. In view of a continued growth and diversification of GPS applications, the scientific community has made an effort to promote international standards for GPS data acquisition and analysis, and to deploy and operate a common, comprehensive global tracking network. As part of this effort, the International GPS Service (IGS) was established by the International Association of Geodesy (IAG) in 1993 and began official operation in January 1994.

Usually, the International Association of Geodesy (IAG) General Meeting in August 1989 in Edinburgh, UK, is considered as the starting point for the IGS. The IGS planning committee was created shortly thereafter and the IGS call for participation was send out in February 1991. At the $\mathrm{XX}^{\mathrm{th}}$ IUGG General Assembly in Vienna in August 1991 the IGS planning committee was reorganized and renamed IGS campaign oversight committee. This oversight committee organized the 1992 IGS Test Campaign scheduled from June 21 to September 23.

The 1992 operations were so successful, that data collection, processing, and product dissemination continued without interruption after September 23, 1992, first on a “best effort bases”, then, starting November 1, 1992, as the “IGS Pilot Service”. During this pilot phase in 1993, the IGS Terms of Reference were written and the current IGS structure was established. The official start of the IGS took place in January 1994. In December 1997 the name of the IGS was slightly changed. The original name was International GPS Service for Geodynamics. Due to the enormous expansion of the IGS the term “for Geodynamics” was no longer considered to accurately reflect all IGS activities, which now also included atmospheric studies. For more information concerning this early phase of the IGS see, e.g., *Mueller and Beutler* [1992], *Beutler et al.* [1994*a*].

The IGS is based on the voluntary contributions of a large number of organizations. The current structure of the IGS consists of [*IGS*, 1998]: global network of tracking stations, operational centers, regional data centers, global data centers, analysis centers (AC), associate analysis centers (AAC), analysis center coordinator (ACC), central bureau (CB), governing board (GB), and working groups. According to the Terms of Reference the accuracy of the IGS products should be sufficient to support current scientific objectives including: scientific satellite orbit determinations, monitoring Earth rotation, realization and easy global accessibility to the International Terrestrial Reference Frame (ITRF), monitoring deformations of the solid Earth, and variations in the liquid Earth, climatological research, eventually weather prediction, and ionosphere monitoring. The primary objective of the International GPS Service (IGS) is to provide the reference system for a wide variety of scientific and practical applications involving GPS. To fulfill its role the IGS produces a number of "fundamental" products, which are: GPS data from a global network of about 200 stations, GPS satellite orbits, GPS satellite clocks, Earth rotation parameters, station coordinates and velocities, station specific tropospheric zenith path delays (ZPD), global ionosphere maps, and GPS receiver clocks.

At the start of the IGS Test Campaign in 1992 the focus was mainly on the GPS satellite orbits. The goal was to provide orbits of an accuracy which would allow the "normal" geodetic GPS user to avoid orbit determination. The effect of an orbit error dR on an estimated baseline component is given by the following "rule of thumb", see [*Baueršíma*, 1983]:

$$dx \approx dR \cdot \frac{L}{R} \tag{4.1}$$

where L and dx are baseline length and baseline component error and R, dR are satellite distance and orbit error. From eqn. (4.1) we see that for a baseline with length $L = 400$ km, $dR = 2$ m (typical error for the GPS broadcast orbits), and $R = 20000$ km the baseline component error will be about 40 mm. Using IGS orbits, assuming an orbit error (dR) of about 100 mm, the baseline length error due to the orbit error will be at the 2 mm level. Figure 4.1 illustrates the effect of the orbit quality on baseline estimates quite nicely. A European baseline of approximately 400 km was processed once using broadcast orbits and once using precise IGS orbits, both solutions were performed over a period of about 100 days. The coordinates of one station were kept fixed, whereas the coordinates of the second station were solved for. Figure 4.1 shows the variation of the daily position estimates of the second, free station, from both solutions. The RMS of the variations using broadcast orbits is 13, 24, and 23 mm in the north, east, and up directions, respectively. This corresponds quite well with the estimated orbit effect of 40 mm. In the case of the IGS orbits the RMS of the variations is 2, 3, and 6 mm in the north, east, and up directions, respectively.

In the following sections we will have a closer look at the IGS products. Our main focus will be on the products as generated by the Center for Orbit Determination in Europe (CODE) for the IGS since June 1992. CODE is one of the seven IGS Analysis Centers (ACs). Where needed, e.g., for comparison, the products of other ACs are also shown. For more information about the IGS and all its components see, e.g., the IGS Annual Reports [*Zumberge et al.*, 1997*a*; *IGS*, 1998; *Mueller et al.*, 1998].

4.2 The Center for Orbit Determination in Europe

The Center for Orbit Determination in Europe, is a joint venture of the Federal Office of Topography (L+T), Wabern, Switzerland, the Federal Office for Cartography and Geodesy

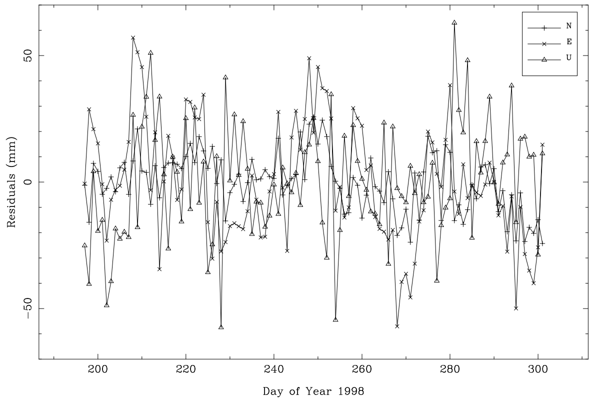

(a) Using broadcast orbits

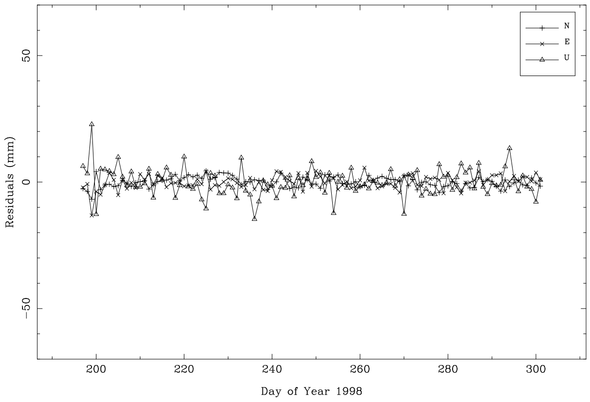

(b) Using IGS orbits

Figure 4.1: Residuals of daily position estimates on a 400 km baseline using orbits of different quality.

(BKG, formerly IfAG), Frankfurt, Germany, the Institut Géographique National (IGN), Paris, France, and the Astronomical Institute of the University of Berne (AIUB), Berne, Switzerland. Although CODE is primarily a global IGS Analysis Center (producing all global IGS products), it lays – according to its name and the participating institutions – special emphasis on Europe. This is mainly reflected by the three following activities at CODE:

- About one third of the sites included in the global CODE solutions are European sites. This should guarantee that the CODE orbits are of best possible quality over Europe.
- Separately a network of about 40 European sites is processed on a daily basis since day 204 (23 July), 1995, using different processing options.
- CODE has also been appointed to combine the weekly solutions of presently 12 regional processing centers in Europe into one official weekly EUREF (European Reference Frame) solution.

CODE is located at the AIUB. All solutions and results are produced with the Bernese GPS Software [*Rothacher and Mervart*, 1996]. Currently version 4.3 of the software is used. For more information about CODE and its IGS and EUREF activities we refer to the CODE annual reports for the IGS [*Rothacher et al.*, 1994, 1995*a*, 1996*a*, 1997*a*].

Three major processing procedures are running at CODE every day: the normal IGS processing to generate the CODE final products, the so-called rapid orbit solution to generate orbits for the "previous" day including predicted orbits which can be used in real time, and the computation of a European solution. The following sections will give a brief overview of these routine procedures.

4.2.1 Daily Global Routine Processing at CODE

A flow chart of the normal IGS routine at CODE is shown in Figure 4.2 and discussed in some detail below. One hour before the start of the routine processing, the data availability is checked. The IGN Global Data Center and the BKG Regional Data Center provide us with the data of the stations we want to process. For several reasons there may still be data missing and therefore the attempt is made to download data that is missing from CDDIS or SIO, the two other global data centers. Under normal circumstances only a few stations have to be downloaded in this step.

The routine analysis starts at 20:00 local time with the processing of the data that were collected three days before. After the download step, all RINEX (Receiver INdependent Exchange format [*Gurtner*, 1994]) observation and navigation files are transformed into the Bernese format, the code observations are checked for outliers, and code single point positioning solutions are computed for each station. This step is necessary to obtain the synchronization errors of the receiver clocks with respect to GPS time. Broadcast ephemerides and clocks are used in this step.

The next part of the routine procedure should result in a set of clean double difference phase data. Because the orbit quality is important for data cleaning this procedure also generates a global 1-day solution of a reasonably good quality. Parameters estimated in this 1-day solution are: orbit parameters, ERPs (including ERP drifts), station coordinates, troposphere zenith delays, and tropospheric gradients. The results of this 1-day solution are labeled G1.

The procedure for the 3-day solutions starts with the computation of a global ionosphere model used for the ambiguity resolution step which follows. Ambiguities are fixed only on baselines shorter than 2000 km. The so-called "Quasi Ionosphere Free" (QIF) method is used to fix the L_1 and L_2 double difference ambiguities to their integer values [*Mervart*, 1995]. On the average 70% of the ambiguities are fixed on these baselines. This relatively low percentage is caused by the low elevation cut-off angle (10^o) which is currently used. With an elevation cut-off angle of 15^o the percentage of fixed ambiguities would be at the 85% level. The low elevation data are obviously of inferior quality.

After the ambiguity fixing (on the single baseline level) a new, complete 1-day solution is generated. This 1-day solution is performed by stacking the normal equations of three different network parts, called clusters [*Brockmann*, 1997]. Within these clusters the correlations between the double difference observations are treated correctly. From this solution (Q1) the full 1-day normal equation system is saved for later use in the 3-day solutions. These 1-day normal equation (NEQ) files contain all parameters that might be of interest later on, i.e., orbit parameters, station coordinates, 2-hourly Earth rotation parameters, nutation drifts, geocenter offsets, tropospheric zenith delays, and satellite antenna offsets.

Two other 1-day solutions, called S1 and S1N, are generated based on the Q1 NEQ file. The S1 solution is generated to obtain the best possible 1-day orbits. This solution is useful because it allows to study the orbit differences between 1-day and 3-day solutions. In comparison with the G1 solution it also shows the effect of ambiguity fixing and correct correlations (in the three clusters) on the orbit estimates. The S1N solution generates a small NEQ file

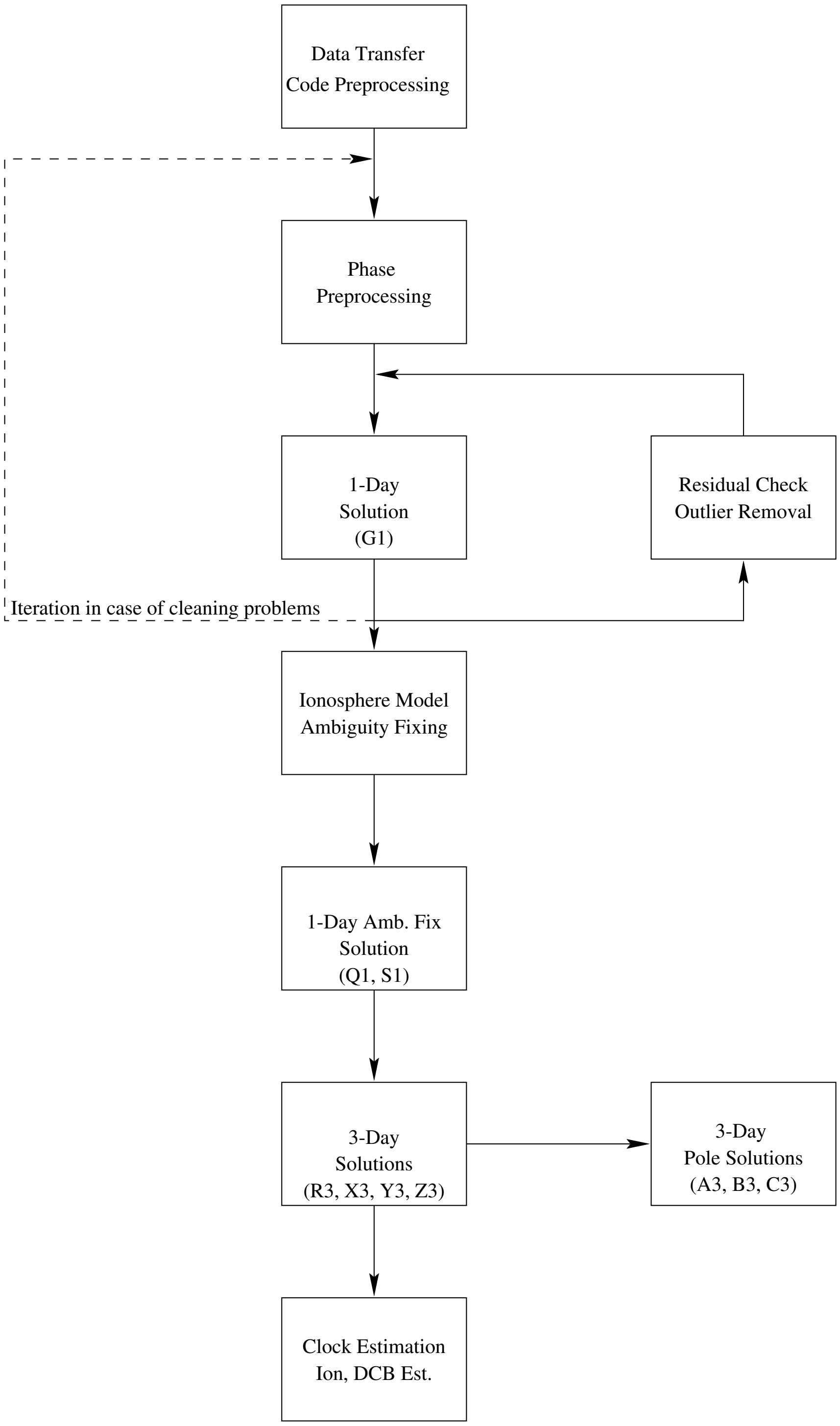

Figure 4.2: Flow diagram of the IGS data processing at CODE.

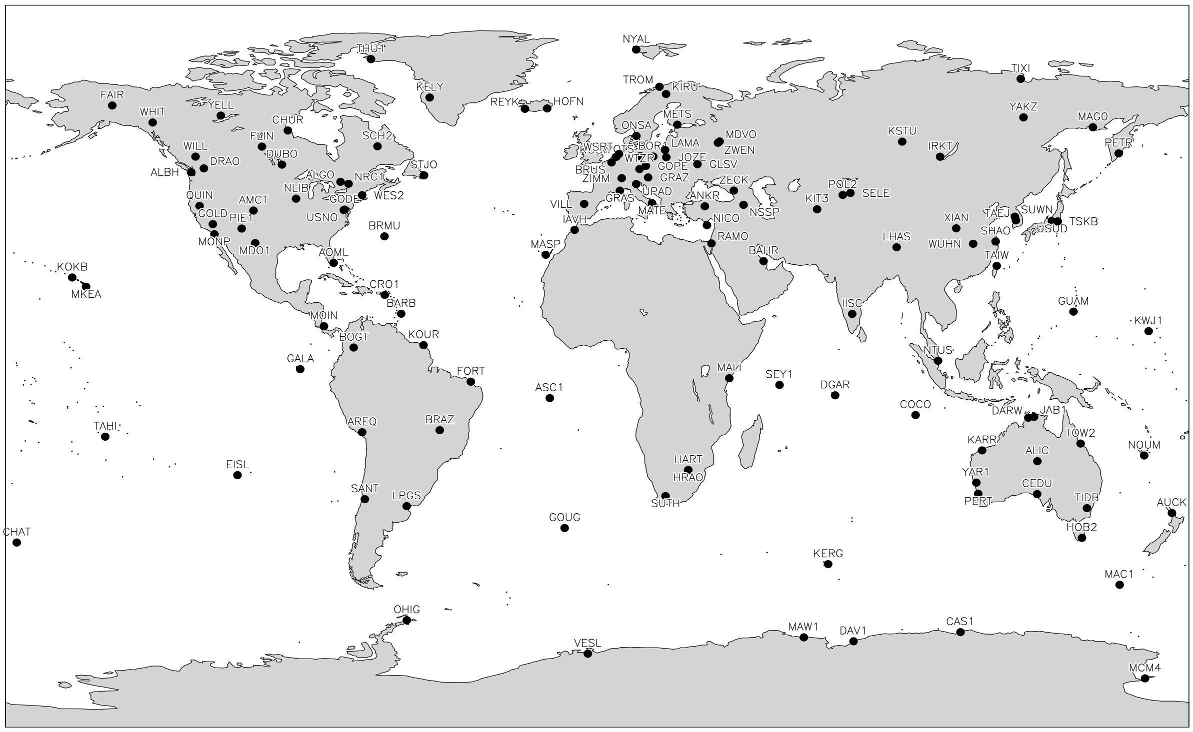

Figure 4.3: The global network of stations used in the CODE routine analysis.

which contains only station coordinates, geocenter, and satellite antenna offsets. These small NEQ files are very useful for generating and studying time series of coordinate estimates.

The 3-day solutions are produced by combining the normal equation of the current 1-day (Q1) solution with the normal equations of the previous two 1-day solutions. In this procedure the three 1-day orbital arcs are combined into one 3-day orbital arc [*Beutler et al.*, 1996*b*]. Currently five slightly different 3-day solutions are created in this way, labeled S3, R3, X3, Y3, and Z3. The S3 solution is generated to save a small 3-day NEQ file containing only station coordinates, ERPs, geocenter, and satellite antenna offsets. The other solutions differ only in the estimated orbit parameters.

Finally, a clock solution is computed, where the satellite and station clocks are solved for simultaneously using undifferenced smoothed code observations. All relevant estimated parameters are taken from the 3-day solution: satellite orbits, ERPs, station coordinates, and tropospheric delays. This ensures that the clock estimates are compatible with these other products.

Figure 4.3 shows the map of the complete network of stations used for the normal IGS routine analysis at CODE (May 1999). From the selected 141 sites at maximum 100 sites are used on any particular day.

The rapid solution, which is computed within 17 hours after the observations were collected, is generated along the same lines, but only one 1-day and one 3-day solution are generated. Furthermore, minor differences exist to speed up the processing in order to guarantee a fast submission of the results.

4.2.2 Daily European Routine Processing at CODE

The European network is used to test and study different processing strategies. Currently, eight different European solutions are generated for each day. Their characteristics are (note that there is only one strategy change from solution to solution):

EG_: Full network solution without ambiguity fixing using a cut-off angle of 15^o. For each station 12 troposphere zenith delay parameters are estimated. A priori the Saastamoinen model is used to correct for the tropospheric delay [*Saastamoinen*, 1972]. The tropospheric zenith delay corrections with respect to the a priori model are estimated by using the simple mapping function $\frac{1}{\cos(z)}$, where z is the zenith angle.

EQB: Same as EG_ solution but with ambiguities fixed to their integer values and estimating 24 instead of 12 tropospheric zenith delay parameters per station. On the average 80% to 90% of the ambiguities are resolved using the QIF ambiguity resolution strategy. This solution is used to study the impact of ambiguity fixing.

NMF: Same as EQB solution but using the Niell mapping function [*Niell*, 1996] without a priori corrections for the tropospheric delays. With a cut-off angle of 15^o degrees no significant differences are expected w.r.t. the EQB solution.

NMW: Same as NMF solution, but using elevation-dependent weighting of the observations. The weight of the undifferenced observations is given by the square of the cosine of the zenith angle ($\cos^2 z$). Because the data at low elevations is likely to be nosier and suffer more from multipath effects, elevation-dependent weighting of the data may be important.

EQ_: Same as NMW solution but using a cut-off angle of 10^o. A lower elevation cut-off angle should give a better decorrelation of station heights and tropospheric delay estimates. However, lower elevation data will probably be nosier and may show more cycle slips and multipath effects.

ET_: Same as EQ_ solution but using the tropospheric delay estimates from the CODE global solution for those stations which are common to both, the global and European network. The idea behind introducing tropospheric delays based on a global GPS solution is, that in regional networks it is difficult or even impossible (depending on the size of the network) to correctly estimate the absolute tropospheric delays. Therefore, it could be an advantage to introduce troposphere estimates for at least one of the regional sites.

NM5: Same as EQ_ solution but using an elevation cut-off angle of 5^o.

NMG: Same as NM5 solution but solving in addition for tropospheric gradients. The asymmetry in the troposphere may play a significant role at low elevations.

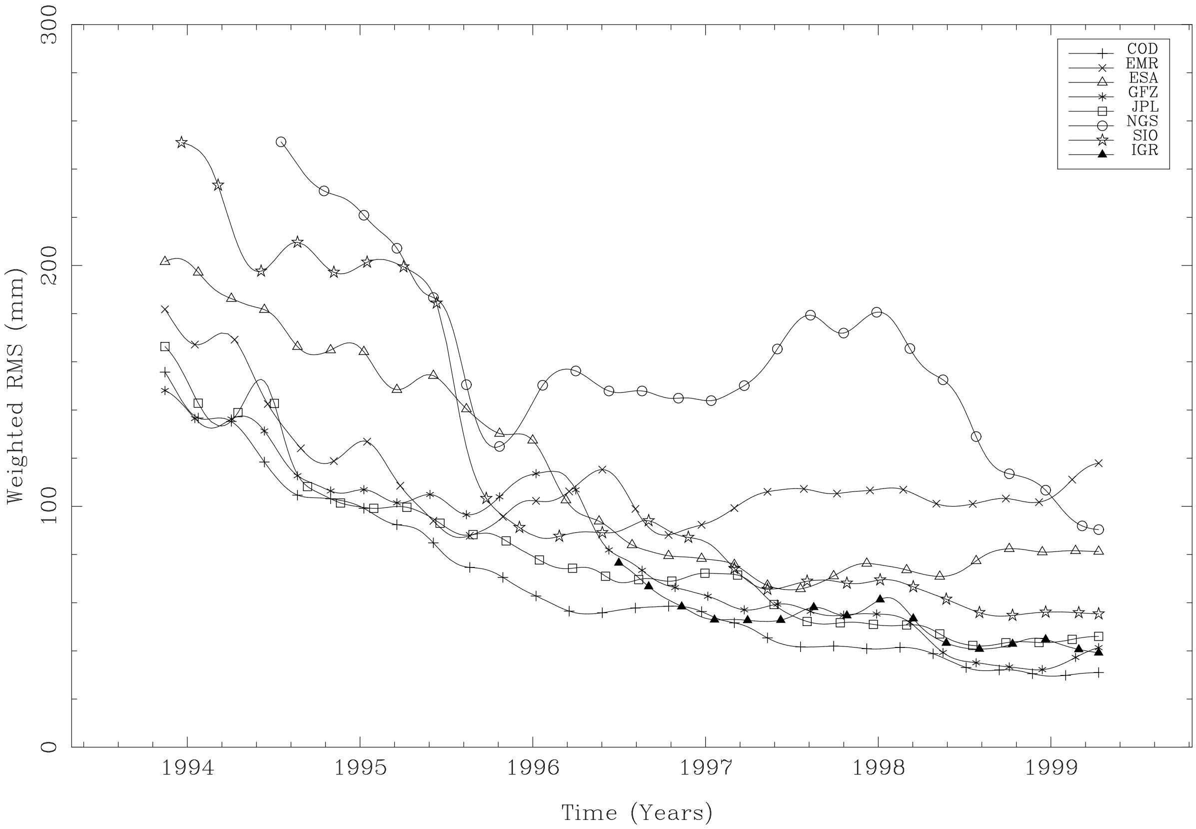

Figure 4.4: Improvement of the IGS combined orbit product since the official start of the IGS in 1994.

4.3 IGS Products and their Quality

The main products of the IGS are still the GPS orbits, although other products have gained some attention as well. In this section we will illustrate the precision of some of the IGS products to show, the improvement of the IGS results over the last couple of years and the quality achieved today.

4.3.1 Orbits

Figure 4.4 shows the orbit quality of the individual IGS ACs as a function of time. The quality of the IGS orbit estimates has improved from a 200 mm to a 30 mm level in a time period of 5 years. Figure 4.4 only shows the internal consistency of the IGS products and not their accuracy. It gives a fair measure of the performance of the individual ACs.

Notice also the quality of the IGS rapid orbit (IGR) in Figure 4.4. This orbit product is available with a delay of currently only 17 hours after the end of observation and its quality is comparable to that of the best final products.

4.3.2 Earth Rotation

Since the very beginning of the IGS activities in 1992, Earth rotation parameters (ERPs) were considered an important product. Soon after the start of the IGS the IERS sub-bureau generating the Bulletin A pole series recognized the timeliness of the GPS ERP estimates and started to rely on this source of information for the X- and Y-component of the Earth rotation axis. By 1996, Bulletin A values were based to about 75% on IGS estimates. For UT this percentage is substantially smaller (few percent only) because of the correlation between the ascending node of the GPS orbits and the rotation of the Earth. This is a problem for all satellite-based UT, estimates. The contribution of the GPS estimates to the final IERS ERP values the "C04" series, had grown to about 45% in 1996 [*Gambis*, 1996]. Another important aspect of the IGS ERP series is the high time resolution of one value per day. The other two space techniques contributing to the establishment of ERPs, SLR and VLBI, provide estimates typically once per 3–5 days. For SLR this spacing is caused by the lack of tracking data. For VLBI this spacing is caused by the observation schedule. With the planned VLBI CORE (Continuous Observations of the Rotation of the Earth) operations this aspect will improve.

Figure 4.5 shows the difference between the CODE ERP estimates and the Bulletin A values. A significant improvement from the 0.5 mas level in 1993 to the 0.1 mas level in 1999 may be observed. The offset of the X-component of about 0.3 mas is significant. This offset is seen by all seven IGS analysis centers (see, e.g., IGSREPORT # 6021) and is clearly above the noise level of the estimates. This indicates that the reference frame, as realized by the IGS products, differs from the reference frame the Bulletin A pole values are referring to.

4.3.3 Station Coordinates and Velocities

The IGS allows the estimation of station positions for a large global network with a precision of a few millimeters in the horizontal and about 10 millimeters in the vertical direction. Crustal movements thus may be detected within a few months. To give an idea of the precision of the IGS coordinate estimates Figure 4.6 shows the weekly coordinate estimates of the station Zimmerwald in Switzerland after removing an offset and drift. The RMS of these residuals is 3, 4, and 8 mm for the north, east and up directions, respectively. However, significant systematic effects may be observed in this kind of time series, i.e., the residuals are far from being random. The height component in particular shows clear signals. Often an annual term is observed which may be caused by multipath effects. Annual periods in 24-hour solutions are expected for multipath because of the 4 minute rotation per day of the satellite–station geometry, resulting in a yearly period of the satellite–station geometry. An annual signal may also be observed in Figure 4.6 for the height residuals of the last 2 years.

Based on the time series of coordinate estimates we may estimate the velocities for all sites in the network. Figure 4.7 shows the estimated (horizontal) velocity vectors for all 164 sites which were used in the CODE IGS processing over the last 6 years. The movements of six of the seven major plates may easily be detected: Eurasia, North-America, South-America, Nazca, Pacific, and Australia. Only the movement of the African plate is difficult to see

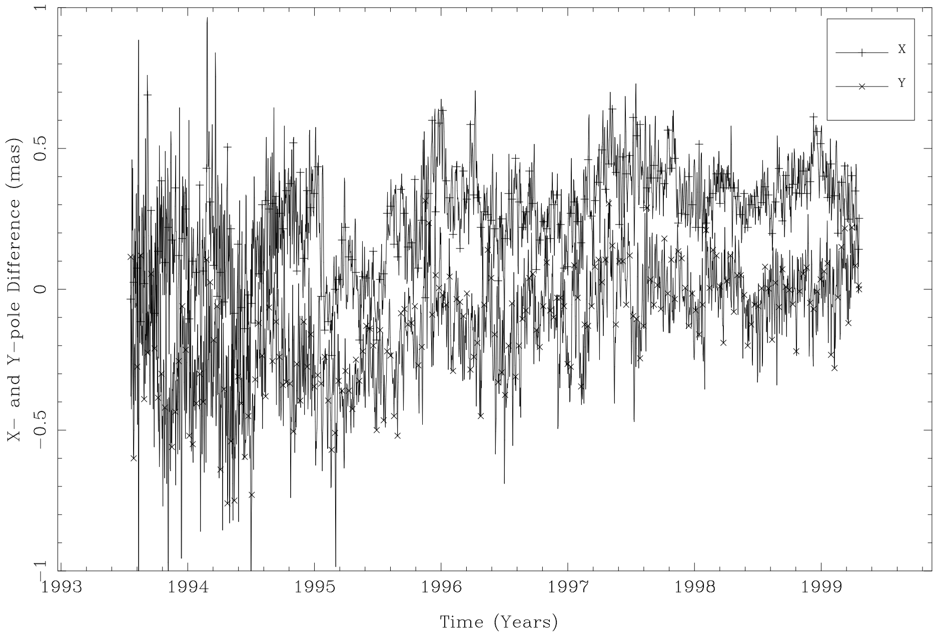

Figure 4.5: Difference between the CODE pole estimates and the IERS Bulletin A values for the X- and Y-pole components.

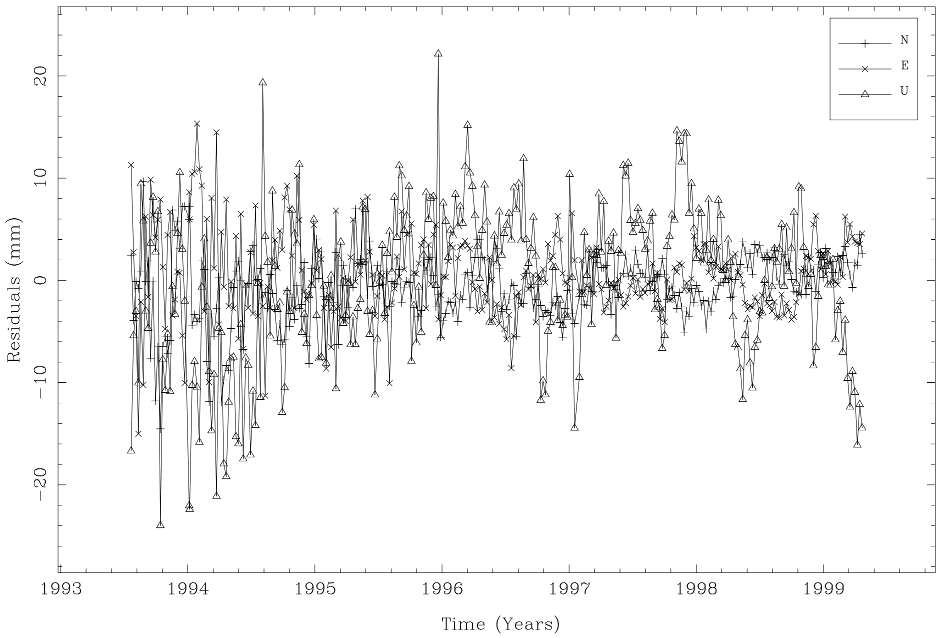

Figure 4.6: Residuals of weekly coordinate estimates for the station Zimmerwald, Switzerland.

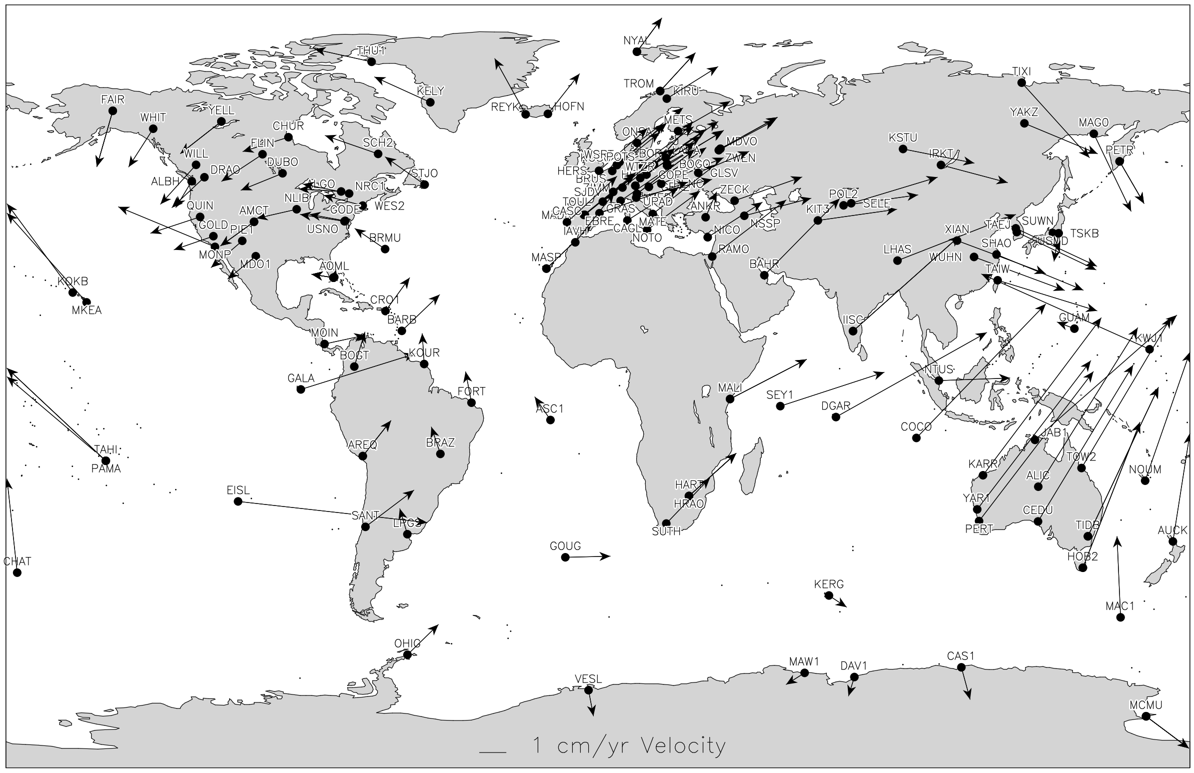

Figure 4.7: Estimated horizontal velocities for 164 sites based on 6 years of continuous GPS observations.

because only few stations are located on this plate. Interesting to see is the movement of the site “MONP” in California. This site is located on the pacific plate rather than on the North-American plate. The large differential velocity between these two plates, as seen in the velocity estimates for “MONP” compared to the velocities of the sites nearby located on the North-American plate, is responsible for the frequent and strong earthquakes in California.

4.4 Using IGS Products for EUREF

Within a few years time the IGS network has grown from a few tens to a few hundreds of stations. In addition many regional arrays have been and are being deployed. Because it is not feasible nor useful to process a network of more than approximately 200 stations in the same adjustment process it is clear that the IGS ACs will never process all the worldwide operational permanent stations. Therefore, in 1994, the IGS started the densification project which aimed at a distributed processing [*Blewitt et al.*, 1994; *Zumberge and Liu*, 1994]. In this scheme all (permanent) IGS stations are processed by at least one AC or Regional Network Associate Analysis Center (RNAAC). The results of all these different distributed processes are than combined at the Global Network AAC (GNAAC) level.

EUREF is one of the RNAACs providing a coordinate solution to the IGS on a weekly basis. The EUREF solution itself is already a combined product based on the contributions from currently 12 different EUREF analysis centers. CODE is one of the EUREF analysis centers and it is responsible for the combination of the individual AAC results into the official EUREF combined solution. Each of the EUREF AACs processes a certain subset of the available European permanent GPS receivers. Results based on a complete (GPS-) week worth of data are submitted by each of the AACs in the Software INdependent EXchange (SINEX) format [*Kouba*, 1996]. All AAC SINEX files are rigorously combined on a weekly basis into the official EUREF (weekly) combined solution. These weekly combined solutions define the EUREF reference frame. Furthermore, they are the EUREF contribution to the realization of the ITRF and to the IGS densification project. For more information about the EUREF activities we refer to [*Springer et al.*, 1997; *Bruyninx*, 1997; *Bruyninx et al.*, 1998].

Regional solutions are sensitive to reference frame changes of the orbits because all regional solutions are processed keeping the IGS orbits fixed. This implies that the reference frame changes of the orbits will show up in the coordinate estimates of the regional solutions.

Reference frame changes occurred several times in the IGS history when changing from one ITRF realization to the next, e.g., from ITRF-92 to ITRF-93. Figure 4.8 shows the change from the ITRF-93 to the ITRF-94 (end of June 1996) producing jumps in the north and east components of the coordinate estimates for the site Maspalomas. In fiducial free network solutions the reference frame change may also be observed in the transformation parameters between the individual weekly solution and the combined solution, based on all the weekly solutions, as also shown in Figure 4.8.

The expected reference frame change from ITRF-93 to ITRF-94, is approximately -1.3 and -1.0 mas for the X- and Y-rotations, respectively (see IGSMAIL # 1384 and # 1391). The observed network rotations agree quite well with these values. Notice also that the change from ITRF-94 to ITRF-96 in March 1998 does not show any signal thanks to the fact that the orientation of both ITRFs is nominally the same. These reference frame differences have to be accounted for when combining regional solutions based on different reference frame realizations.

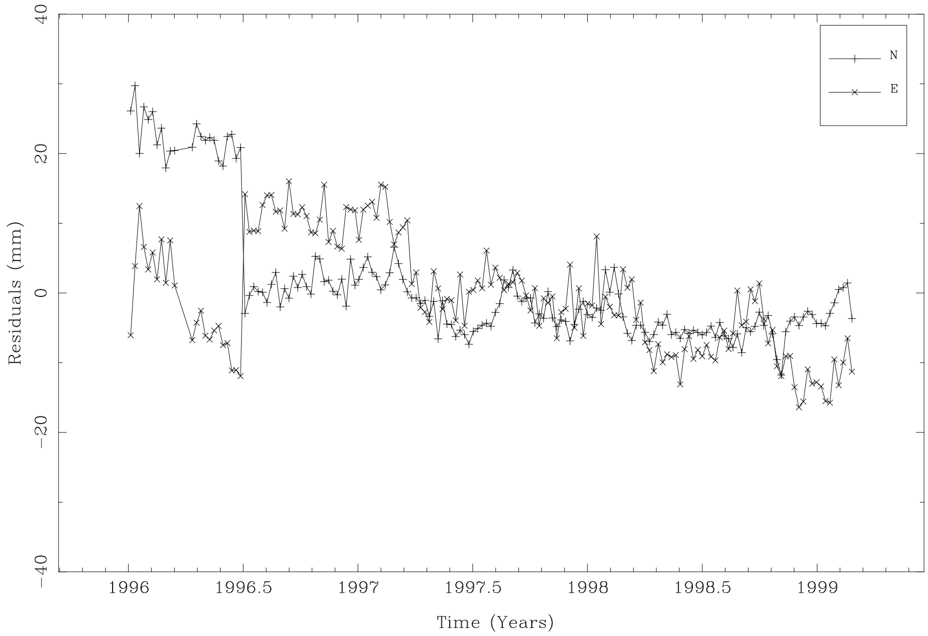

(a) Effect on coordinates of Maspalomas

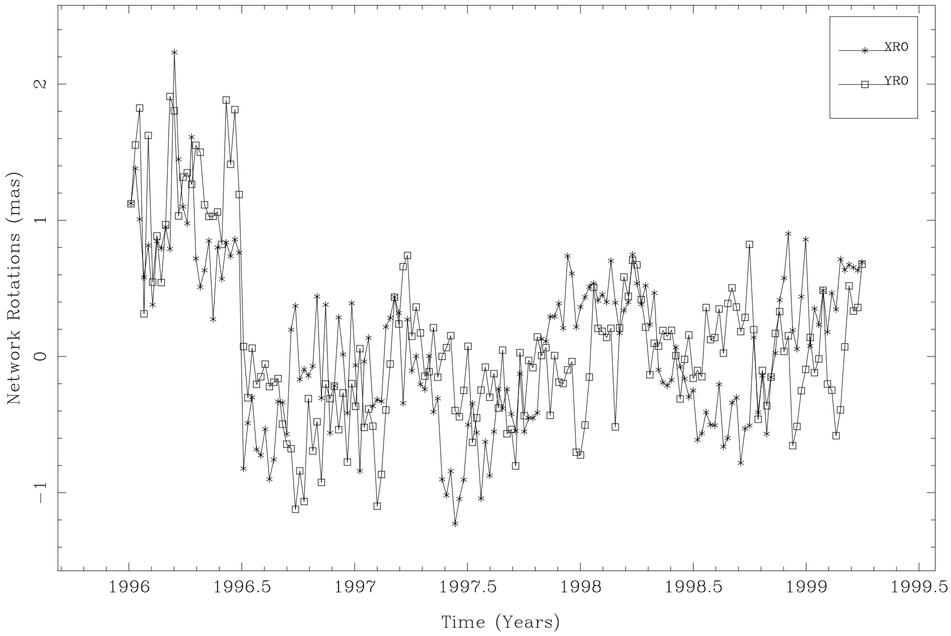

(b) Effect on network

Figure 4.8: The effect of changes in the reference frame of the IGS orbits on regional solutions with “fixed” orbits.

5 Investigations Based on CODE and IGS Products

5.1 Developments at CODE

CODE has been part of the IGS since its foundation in June 1992. Thus by now, May 1999, CODE has been processing the GPS observations of a global network for almost 7 years. Table 5.1 lists the more significant changes between June 1992 and December 1995 and Table 5.2 shows the changes since 1996.

Apart from these processing improvements, the number of stations (and consequently the number of observations) included in the global network as processed by CODE, steadily increased from about 20 at the beginning in June 1992 to 100 by mid 1998. Furthermore, during the early phase of the IGS also the number of satellites increased rapidly from 19 to 25 in one year. The increase of both, the number of satellites and the number of stations over the last 6 years, is shown in Figure 5.1. All the improvements in the processing scheme and the increase of the number of stations and satellites have significantly improved the quality of the CODE IGS products. Below we will have a closer look at the influence of the processing changes on the IGS and CODE products.

5.1.1 Reference Frame Changes

Four reference frame changes are documented over the last 7 years in Table 5.1 and Table 5.2. Because of its close link to the IERS (International Earth Rotation Service), the IGS always adopted the latest realization of the ITRF soon after its official release. In only a few years time the reference frame was therefore changed from the ITRF-91, to the ITRF-92, ITRF-93, ITRF-94, and in March 1998 to the ITRF-96. These changes in the reference frame can very clearly be seen in our routine 1-day (G1) pole series when compared to the, presumably continuous, IERS Bulletin A pole series, as shown in Figure 5.2. These changes in the reference frame cause some practical problems for users of the IGS products as we have seen in Section 4.4.

At CODE we save small NEQ files from our 3-day solutions (S3) which allow to easily and quickly recompute our ERP, station coordinate, and velocity time series in a new reference frame. Based on the larger 1-day NEQ files we could of course also recompute our orbits. However, we have only a limited number of these large (25 MB!) files on-line and it would

Date	Doy/Year	Description of Changes at CODE
01-Oct-92	275/92	Zenith distance computation corrected to use ellipse and not sphere.
02-Apr-93	092/93	Use of some redundant baselines.
14-Jun-93	165/93	Estimate small velocity changes for the eclipsing satellites.
01-Jan-94	001/94	Change from the ITRF-91 to the ITRF-92 coordinate and velocity set for the 13 fixed sites.
29-May-94	149/94	Estimate polar motion as offset and drift over 3-days.
01-Jan-95	001/95	Change from the ITRF-92 to the ITRF-93 coordinate and velocity set for the 13 fixed sites.
04-Jun-95	155/95	Estimation of small velocity changes for all GPS satellites at 12:00 UT and 24:00 UT (once per revolution).
04-Jun-95	155/95	Correct correlations in the 1-day solutions using 7 different clusters.
25-Jun-95	176/95	Ambiguity-fixed solutions submitted as the official solution.
31-Aug-95	243/95	Number of clusters reduced from 7 to 5.
10-Sep-95	253/95	Precise satellite clocks are estimated using code observations and submitted together with the precise orbit files.

Table 5.1: Major changes in the processing scheme at the CODE analysis center from June 1992 to December 1995.

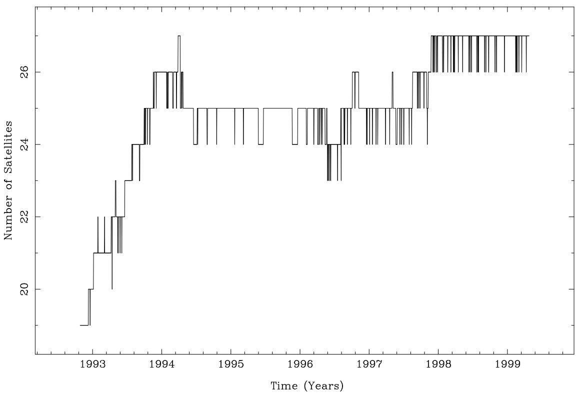

(a) Number of Satellites

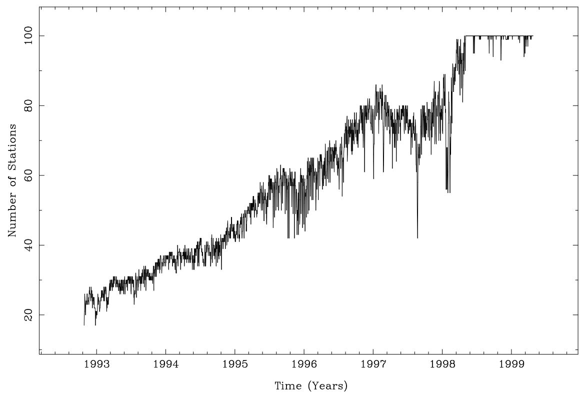

(b) Number of Stations

Figure 5.1: Increase in the number of satellites and stations over the 7 years of IGS activities at CODE.

Date	Doy/Year	Description of Changes at CODE
21-Jan-96	021/96	Switch of radiation pressure model from Rock4/42 S-model to the T-model.
24-Mar-96	084/96	Set-up of sub-daily pole and UT1-UTC estimates (offsets and drifts in 2-hour intervals) in the routine solutions for internal purposes.
15-May-96	136/96	Number of clusters reduced from 5 to 4.
30-Jun-96	182/96	Change of the reference frame to ITRF-94. Phase center corrections with model IGS_01.PCV. Model by R.D. Ray [*McCarthy*, 1996] for sub-daily variations in the Earth rotation introduced as a priori model.
30-Jun-96	182/96	Orbit force model changed: JGM3 (previously GEMT3); General relativity term implemented; Love number changed from 0.285 to 0.300 (IERS Standards [*McCarthy*, 1996]).
29-Sep-96	273/96	CODE final orbits are now based on a solution using the extended radiation pressure model. Besides the direct radiation pressure term and the Y-bias the 3 terms (one constant and two periodic terms) in the B-direction (see Chapter 6) are estimated. In addition, several minor improvements of the force field were implemented.
19-Jan-97	019/97	Satellite clocks estimated using phase-smoothed code observations.
05-Oct-97	278/97	Elevation cut-off angle decreased from 20^o to 10^o. Furthermore the observations are now weighted with $\cos^2 z$, where z is the zenith angle. A new tropospheric mapping function (Niell) is now used.
19-Oct-97	292/97	Number of clusters reduced from 4 to 3.
01-Mar-98	060/98	Reference frame changed to ITRF-96. Number of reference sites increased from the original 13 to 37 sites. Ocean loading corrections for the station coordinates.

Table 5.2: Major changes in the processing scheme at the CODE analysis center from January 1996 to May 1999.

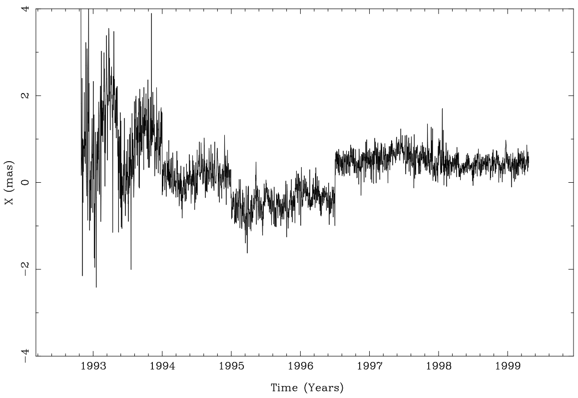

(a) X-pole

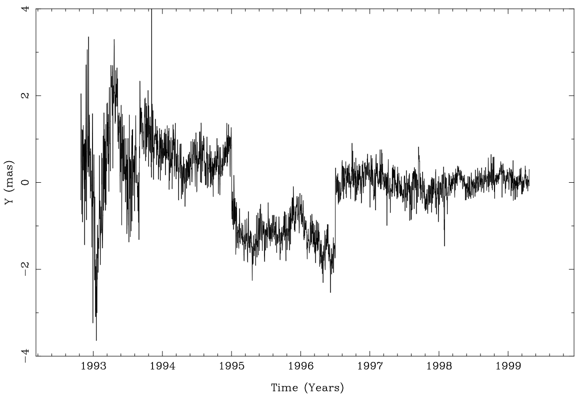

(b) Y-pole

Figure 5.2: Changes in the reference frame realization as seen in the estimates of the pole coordinates (x_p and y_p) compared to a continuous pole series (Bulletin A).

take a lot of time (30 min CPU time per 3-day solution) which makes the task very difficult. The small (2 MB) NEQ files are all available on-line and processing a 3-day solution takes only a few seconds.

Over the years the quality of the ITRF realizations steadily improved. Until March 1998 the reference frame was realized by fixing, or tightly constraining, the positions of 13 selected stations. By mid 1996 it had become clear that from the original 13 stations, selected in 1993, only 8 or 9 remained valid candidates. At that time it became evident that the realization of the reference frame for the IGS products was limited by the set of stations used for the realization rather than by the quality of the reference frame itself. Therefore, at the IGS workshop in 1996, a new and much enlarged set of stations was selected and the final set of 52 so-called reference stations was agreed upon during the IGS workshop in 1997 [*Kouba et al.*, 1998]. The change in the realization of the reference frame, in March 1998, from the ITRF-94 to the ITRF-96, and, at the same time, the new and larger set of reference stations, greatly improved the IGS realization of the terrestrial reference frame [*Kouba and Mireault*, 1998*a*].

Although the ITRF-96 is of excellent quality, a pure GPS-based reference frame might still provide a better precision. Therefore, a new IGS working group, the IGS reference frame project, was created. This group should develop the official IGS terrestrial reference frame. This IGS reference frame shall be aligned to the official IERS terrestrial reference frame.

5.1.2 Orbit and Clock Changes

Figure 5.3 shows the development of the CODE orbit and satellite clock estimates as reflected by the IGS combination reports. Figure 5.3(a) shows the development of the CODE orbit esti-

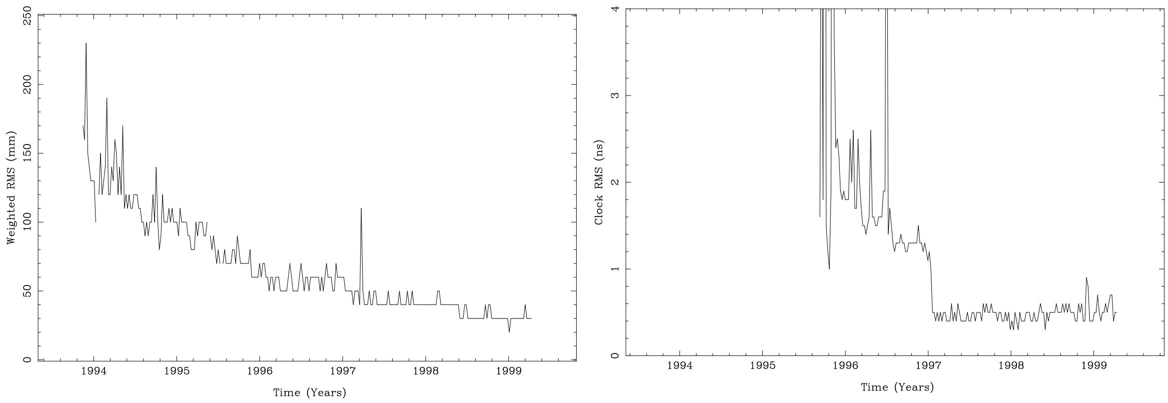

(a) CODE Orbit RMS

(b) CODE Clock RMS

Figure 5.3: Improvement of the CODE orbit and satellite clock estimates since the official start of the IGS in 1994.

mates using the weighted RMS of the IGS orbit combination as quality measure. An impressive improvement from 200 mm to 30 mm in a few years time may be observed. Many factors have contributed to this quality improvement like, e.g., the increased number of satellites and stations, and numerous model and processing improvements. The improvements resulting from the estimation of stochastic pulses and the ambiguity fixing, implemented in mid 1995, are clearly visible. The RMS improved from the 90–100 mm level to the 70–80 mm level. Surprisingly, the change of orbit parameterization in September 1996 [*Springer et al.*, 1999*b*], does not show up although this change constituted a large improvement. That the estimation of the three solar radiation pressure parameters in the B-direction (see Chapter 6) actually improved the orbit estimates can be seen in Figure 5.4. This figure shows the daily RMS, over all satellites, of the differences between the satellite positions at the end of the middle day of a 3-day arc and the beginning of the middle day of the next 3-day arc. The figure shows these RMS values for all 3-day solutions of the year 1997. The extended (+3 parameters) model performs much better than the classical model. We will take a closer look at the orbit model and possible improvements in Chapter 6.

Figure 5.3(b) shows the development of the CODE satellite clock estimates taking the RMS of the IGS clock combination as quality measure. CODE started providing satellite clock estimates in September 1995. After some initial problems the quality of the clock estimates was stabilized at the 1.4 ns level. This quality level agrees quite well with the noise of the undifferenced P_3 code observations ($\pm$ 50 cm) which were used to obtain these clock estimates. Since January 1997 the clock estimates are based on phase-smoothed code observations and consequently the quality reached the 0.5 ns level. More information about the CODE clock estimates may be found in Chapter 8.

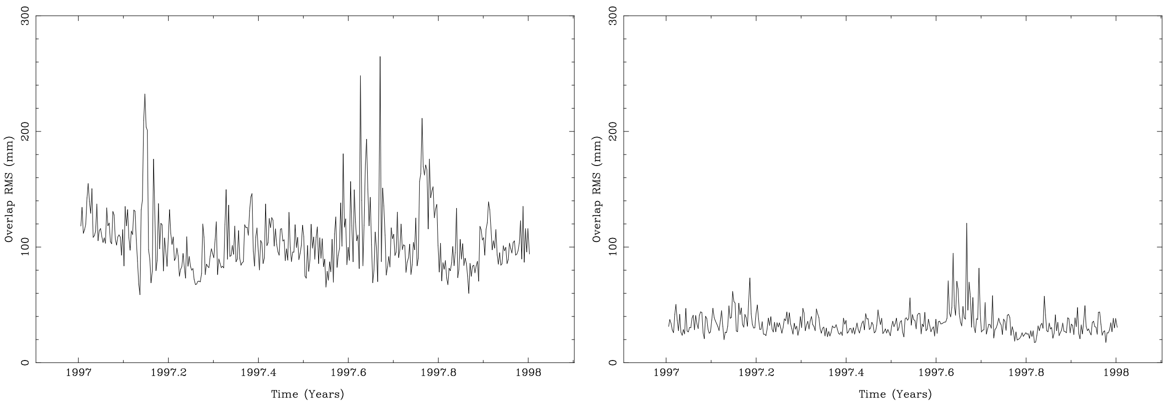

(a) Classical model

(b) Extended model

Figure 5.4: Orbit overlap results for the classical (2-RPR parameters) and extended (5-RPR parameters) radiation pressure models.

5.1.3 ERP Estimation with Sub-Daily Resolution

The amount of data available within the IGS and the temporal density of the data allows for a high time resolution of the estimated parameters. This aspect is interesting for polar motion and UT1 because it allows to estimate sub-daily variations in Earth rotation as caused by, e.g., the tidal effects from Sun and Moon. Therefore, CODE started to solve for ERPs with a time resolution of 2 hours, on a routine basis, early in 1996. Thanks to a reprocessing effort, in which all data from 1995 onward was reprocessed, CODE has an uninterrupted series of 2-hourly ERP estimates starting in 1995. The diurnal retrograde polar motion (nutation) which is not accessible by GPS, has been suppressed in the processing. This unique series now covers more than 4 years and allows the accurate determination of sub-daily polar motion and length of day (LOD). The GPS-based ERP series is at least as good as the best currently available series extracted from SLR or VLBI [*Rothacher*, 1998]. Figure 5.5 shows the sub-daily polar motion as seen by the CODE 2-hourly estimates and the sub-daily polar motion based on the Ray model which is the current IERS standard [*McCarthy*, 1996]. The two curves in Figure 5.5 are shown with the same line type to underline the agreement between the GPS estimates and the Ray model. We expect that future ocean tide models for sub-daily variations in Earth rotation will heavily depend on GPS observations.

In June 1996 the Ray model was implemented into the software as a priori model for the sub-daily variations in Earth rotation due to ocean tides. The LOD and the associated UT, actually integrated LOD, time series, based on our 1-day (G1) solutions are shown in Figure 5.6. We clearly see the impact of including the sub-daily ERP model. The annual signal observed from 1993 until mid 1996 disappeared after the introduction of the sub-daily model. The same effect was observed for some of the other IGS ACs. The annual period

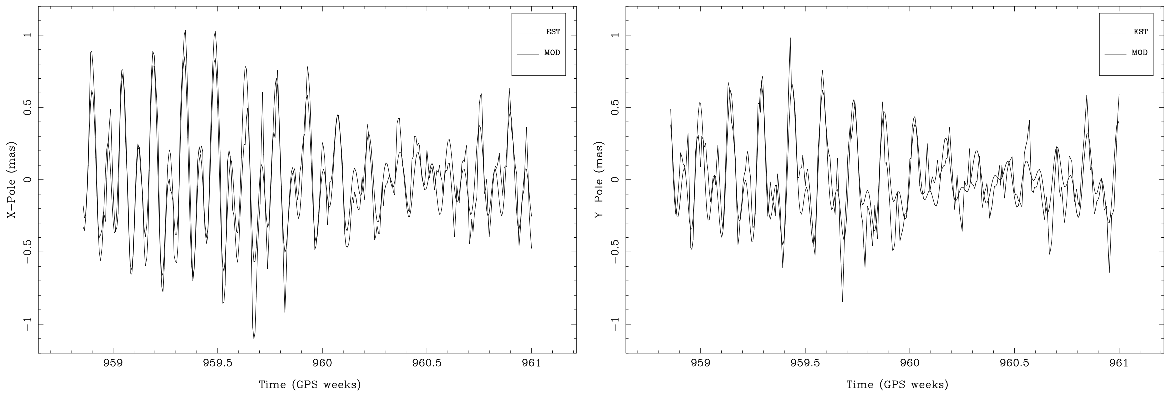

(a) X-pole (b) Y-pole

Figure 5.5: GPS-based 2-hourly X- and Y-pole estimates compared to 2-hourly values predicted by a sub-daily polar motion model for GPS weeks 959 and 960.

is caused by the daily "sampling" of the sub-daily signals which do not have exactly 12 and 24 hour periods. Our official products, based on 3-day rather than 1-day solutions, suffered much less from this problem thanks to the implicit smoothing caused by using 3-day solutions.

5.1.4 Other Processing Changes

Figure 5.7 shows the significant impact of two processing changes on the geocenter estimates. The Y-component of the geocenter changed significantly when we introduced the estimation of small velocity changes for all satellites in June 1995. The Z-component changed when we started global ambiguity fixing in September 1994.

The estimation of small velocity changes improved our orbit estimates significantly as was shown in Figure 5.3(a). At the same time a small Y-shift of the orbit was noticed in the IGS orbit combination (see Figure 5.8(b)). A similar Y-shift has also been observed for the JPL AC related with its estimation of stochastic pulses [*Kouba*, 1995]. It is interesting that the Y-shift of the orbit occurred despite the fact that the positions of the 13 reference stations were tightly constrained. Figure 5.7(a) shows that this Y-shift is also observed in our weekly geocenter estimates. After the introduction of the small velocity changes the geocenter estimates are much closer to the ITRF origin. We will have a closer look at this Y-shift in Section 5.2.

CODE was the first IGS AC implementing global ambiguity fixing on a routine basis. For our IGS products we introduced global ambiguity fixing in June 1995, but internally we started to produce ambiguity fixed series already in September 1994. Ambiguity fixing improves the results in general. The improvement is most pronounced in the geocenter estimates. Figure 5.7(b) shows the Z-component of our weekly geocenter estimates. During the first years

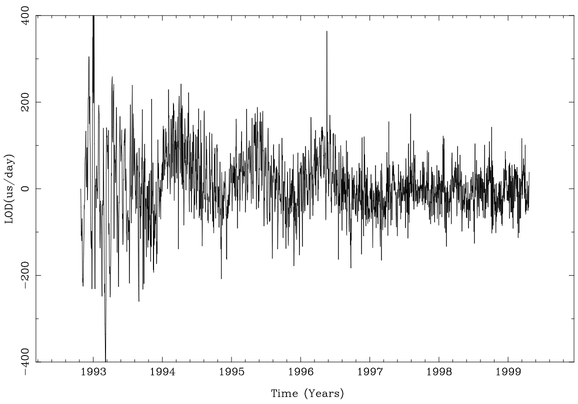

(a) LOD

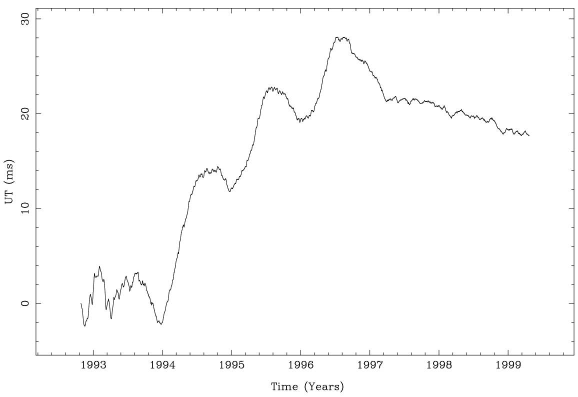

(b) UT, integrated LOD

Figure 5.6: Impact of the sub-daily ERP model on the LOD estimates.

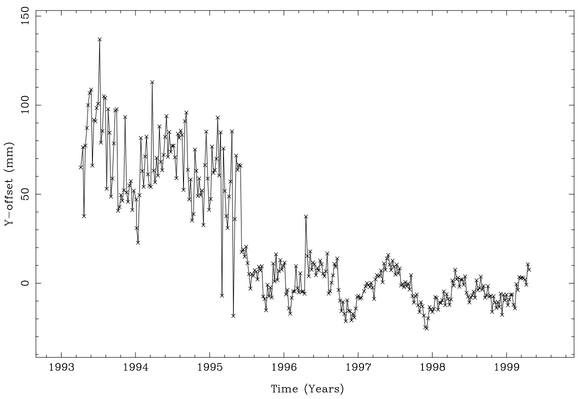

(a) Y-offset

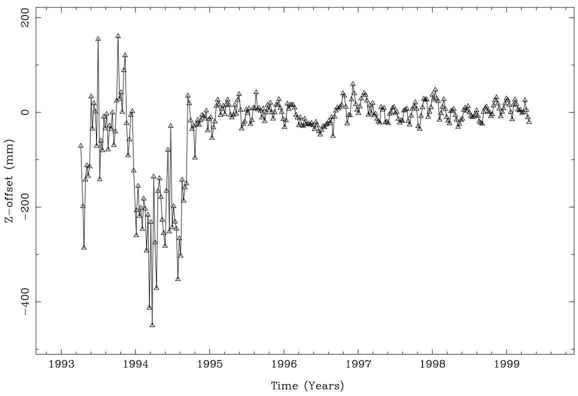

(b) Z-offset

Figure 5.7: Effect of processing changes on the weekly geocenter estimates.

Sol. ID.	Amb. Fix.	Ele. Cut.	Map. Func.	Ele. Wgt.	Repeatability			Remarks
					N	E	U	
EG_	NO	15	SAAS	NO	2.1	2.6	5.7	Amb. Free
EQB	YES	15	SAAS	NO	1.9	1.9	5.6	Amb. Fixed
NMF	YES	15	NMF	NO	1.9	1.9	5.8	Niell Map.
NMW	YES	15	NMF	YES	1.7	1.7	5.5	Ele. Weight
EQ_	YES	10	NMF	YES	1.8	1.7	4.9	cut-off 10^o
ET_	YES	10	NMF	YES	1.7	1.7	4.5	Global Trop.
NM5	YES	5	NMF	YES	1.8	1.8	4.8	cut-off 5^o
NMG	YES	5	NMF	YES	1.7	1.7	4.8	Tropo. Gradients

Table 5.3: Repeatability of the daily European solutions at CODE based on days 060–157 of 1998.

the estimates are rather unstable. Clearly, the repeatability of the (Z) geocenter estimates improves significantly after September 1994, when we started using our ambiguity fixed results. Also, we observe a jump when switching from the ambiguity free to the ambiguity fixed results. Let us add that ambiguity fixing improves the repeatability of station coordinate estimates, especially in the east component.

The different scales of the geocenter Y- and Z-plots, indicate that the estimates of the Z-component are weaker than those of the Y-component. The RMS over all weekly geocenter estimates since 1996 is 7, 10, and 20 mm for the X-, Y-, and Z-component, respectively. The quality difference may be explained by the fact that the rotation of the Earth around its spin axis provides a good observation geometry for the X- and Y-component but not for the Z-component. In addition, the Z-estimates may also be weakened by the observation "gaps" at the poles due to the 55^o inclination of the orbits. In the Y-component a clear annual signal is observed with an amplitude of 10 mm. If this signal is subtracted from the time series the RMS for the Y-component is reduced to 7 mm. In the Z-component an annual signal with an amplitude of 17 mm is observed. In addition, two signals with periods of 50 and 44 days are observed with amplitudes of 11 and 6 mm, respectively. Subtracting these three signals from the time series reduces the RMS of the Z-component to 13 mm. No periodic signals are observed in the X-component. Annual and semi-annual signals are expected in the geocenter estimates and have been observed by other techniques, SLR and VLBI, as well [*Ray*, 1999]. The two signals around 50 days, observed in the Z-component, are unexpected. One possible explanation might be the orbit model because these signals start to show up after September 1996 which is where we changed our solar radiation pressure model.

Over the last couple of years we intensively studied the effect of different processing strategies, mainly using our European network. Recently, our focus has been on lowering the elevation cut-off angle, improving the modeling of the tropospheric delays, and improving the observation model. Table 5.3 shows the internal consistency of our different European solutions, described in the Chapter 4, based on days 060–157 of 1998.

The main conclusions that may be drawn from Table 5.3 are that ambiguity fixing mainly improves the repeatability of the east component of the coordinate estimates. Lowering the elevation cut-off angle improves both, the horizontal and vertical repeatabilities. The estimation of tropospheric gradients improves the results if low elevation tracking data is available. In Table 5.3 this fact is obscured because the repeatability is dominated by the "bad" stations which do not have low elevation tracking. Finally, the introduction of global troposphere zenith delay estimates in the regional solutions improves the repeatabilities of the height component. More detailed information about the research using our European solutions may be found in *Springer et al.* [1997] and *Rothacher et al.* [1997*b*]. Based on the results from this European network the elevation cut-off angle for the CODE global solutions was lowered from 20^o to 10^o in October 1997. At the same time also the tropospheric mapping function was changed (Niell) and elevation-dependent weighting ($\cos^2 z$) was implemented. Similar improvements, as seen for the European solutions, were observed for the global solutions [*Rothacher et al.*, 1998].

We demonstrated that ambiguity fixing has a significant impact on the quality of geodetic parameters estimated using GPS. Currently ambiguity fixing, at CODE, is limited to baselines with a length below 2000 km. This means that there are several baselines in the global network (Figure 4.3) where no ambiguities are fixed. Both, a reduction of the average baseline length, by including more stations in remote areas, and an increase of the minimal baseline length for the ambiguity fixing, would result in a higher percentage of fixed ambiguities. This would strengthen the solutions significantly. As a test, since May 1998, we fix ambiguities on all baselines for the CODE rapid orbits. For baselines longer than 2000 km we use the Melbourne-Wübbena linear combination (see eqn. (2.21)) to determine the wide-lane ambiguities. In a second step we use the ionosphere-free linear combination (eqn. (2.12)), where we resolve the narrow-lane ambiguities (eqn. (2.16)).

The results of the CODE AC have improved significantly thanks to a large number of processing changes. However, the jumps caused by some of the processing changes, give significant problems in, e.g., the multi-annual solutions, station coordinate time series, and the 2-hourly pole estimates. Therefore, the continuous improvements of the processing strategies make it mandatory to reprocess the "old" data using a (more) uniform processing strategy. The large improvements achieved in recent years, will make such a reprocessing very promising and, most probably, very rewarding.

5.2 Open Issues

5.2.1 The Geocenter Y-Shift

The geocentric Y-shift of the orbits of individual ACs w.r.t. the IGS combined solution, was discovered already in 1994 in the IGS orbit combinations. It soon became clear that these shifts changed when the orbit modeling changed. Figure 5.8 shows the translation in the Y-direction of the orbits of two IGS ACs (CODE and JPL) relative to the combined IGS orbit.

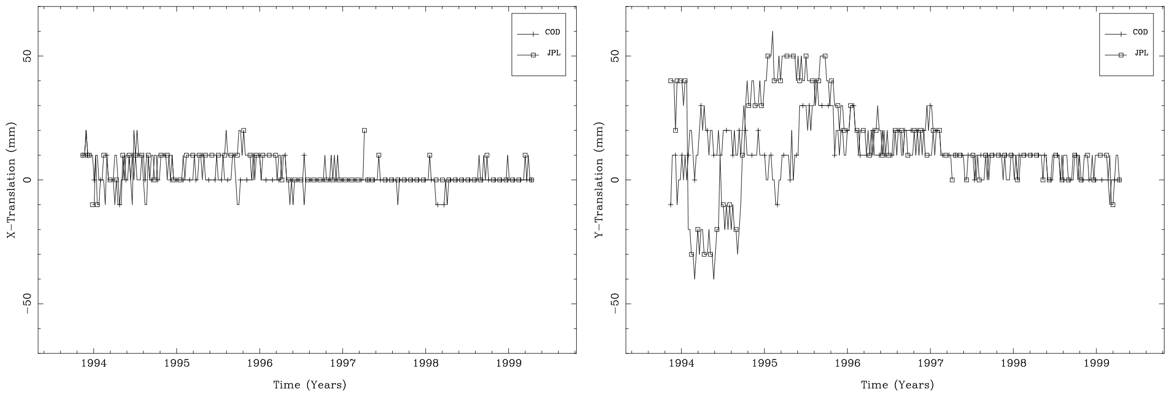

(a) X-Translation

(b) Y-Translation

Figure 5.8: Orbit translations relative to the IGS combined orbits.

For reference the X-translation of the orbits for the same two ACs and the same time period is also given. In 1994 two jumps of approximately 70 mm may be observed in the JPL results. These jumps are related to the changes in the stochastic orbit model used by JPL. By the end of January 1994 JPL stopped solving for stochastic pulses, a strategy change related to the fact that AS was turned on. Later in 1994, JPL reactivated the estimation of the stochastic pulses. In mid 1995 a similar, but smaller jump may be observed in the CODE results, when CODE started estimating small velocity changes for all satellites. The reduced size of the jump for CODE is most likely caused by the usage of 3-day arcs which seems to reduce the size of the Y-shift compared to short-arc solutions. The Y-shift observed for the orbits is also visible in the geocenter estimates as was shown previously, see Figure 5.7(a). Notice that no jumps can be observed in the X-component for both, the orbit and the geocenter.

It was thought that insufficient orbit modeling might cause a geocenter Y-shift due to the weak geometry of the IGS tracking station network and especially of the 13 fixed reference stations. We decided to study the impact of different orbit models on the geocenter location. For this purpose the CODE final orbit positions for the year 1997 were used as pseudo-observations in an orbit determination process. Note that our reference orbits do not show a Y-shift, i.e., the geocenter by definition agrees with the ITRF origin. In the orbit determination process only two radiation pressure parameters were estimated, in addition to the six initial conditions. This parameterization is similar to what was done for the CODE products prior to June 1995. These estimated orbits were then compared to the original orbits through a seven parameter transformation exactly as it is done in the IGS orbit combinations. The comparison was performed separately for the six different orbital planes, using all satellites in the plane. Figure 5.9 shows the observed X- and Y-shifts of the estimated orbit w.r.t. the original orbit. One curve is drawn for each of the 6 orbital planes (A–F), and one curve is drawn for the complete satellite system (ALL). The daily values were smoothed to obtain a clearer picture.

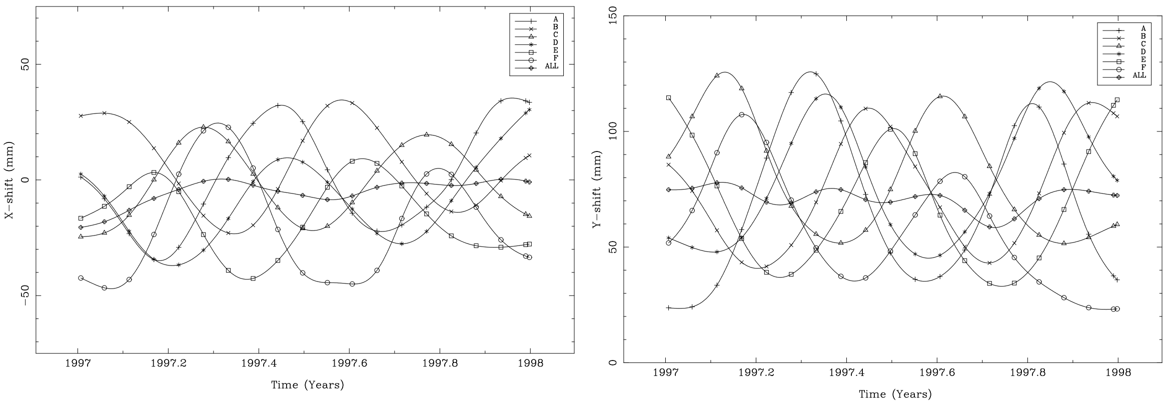

(a) Orbit X-shift

(b) Orbit Y-shift

Figure 5.9: Effect of the orbit model on the satellite positions.

The Y-translation, shown in Figure 5.9 for the individual orbital planes, has a mean offset of approximately 75 mm. On top of this, semi-annual variations are observed for each orbital plane, with an amplitude of approximately 55 mm. The maximum Y-shift is observed during the eclipse season of the orbital plane. A similar picture is observed for the X-translation which, however, has a zero mean offset but a semi-annual variation with an amplitude of 40 mm. The minimum X-shift is observed during the eclipse season of the orbital plane. We conclude that the observed geocenter and orbit Y-shifts are caused solely by the orbit model and have nothing to do with the geometry of the IGS tracking network. The procedure, fitting a good orbit using a bad model, knows nothing about the geometry of the tracking stations. This raises the question why an orbit modeling problem causes a geocenter shift. It is interesting to note that a geocenter shift causes a periodic (once per revolution) perturbation in the satellite orbit.

5.2.2 Antenna Phase Center Offsets

One of the major remaining problems in GPS data processing are the locations of the satellite and receiver antenna phase centers. The recently observed bias (1 meter!) in the phase center location of the first block IIR satellite (PRN 13) has made it clear that the position of the satellite phase center offset is not well known [*Bar-Sever*, 1998]. Also, the elevation-dependent phase center variations of the receiver antennas is a major error source. The phase center offsets are also highly correlated with the estimated tropospheric zenith delays and the terrestrial scale.

To study the effects of the antenna phase center offsets we generated a series of test solutions using different processing strategies. The solutions should give a better understanding of the correlations between the phase center offsets, the phase center variations, the tropospheric zenith delays, and the terrestrial scale. The following four processing options were modified in the solutions:

- Constrained or free terrestrial scale. The "constrained" solutions are generated by constraining the coordinates of 37 reference stations to 1 mm. The free solution is generated by using minimal constraints (3 rotational constraints).

- The satellite phase center offset (Z-offset) is either fixed, artificially changed, or estimated. We call this a Z-offset because the direction of the vertical satellite phase center offset corresponds with the Z-axis of the satellite-fixed reference frame. The Z-axis is the axis pointing from the satellite to the geocenter.

- Either relative receiver antenna phase center variations, relative to the Dorne Margolin antennas [*Rothacher et al.*, 1996*b*], or absolute variations using the anechoic phase chamber values [*Rocken et al.*, 1996] are used.

- Different elevation cut-off angles (10^o, 15^o, or 20^o) are used.

Combinations of these processing options were tested and the results are summarized in Table 5.4. The reference solution was a minimally constrained (3 rotational constraints) solution, which means in particular that the terrestrial scale was free. The other processing options of the reference solution were identical with those of our official IGS solution, i.e., 10^o cut-off angle with elevation-dependent weighting, relative phase center variations introduced, and no Z-offset estimated. The normalized RMS of the one-way L_1 phase observations of this reference solution was 1.46 mm. The first column of Table 5.4 identifies the processing option which was changed w.r.t. the reference solution. The next three columns show the mean difference between the test solution and the reference solution, in terrestrial scale, tropospheric zenith path delay, and estimated satellite antenna offsets. The last column gives the normalized RMS of the one-way L_1 phase observations.

We first wanted to know whether there were significant differences between the solutions with a fixed or free scale. No significant differences were found. Secondly, we tested the influence of the elevation cut-off angle by changing it from 10^o to 15^o and 20^o. Here a change of 1.0 ppb in the terrestrial scale was observed going from a 10^o to a 20^o cut-off angle. This change corresponds to a 6 mm height change of the station heights. The formal errors of the height estimates, however, were 3–5 mm and 3–6 mm for the 10^o and 20^o solutions, respectively. Thus a 1.0 ppb scale change is practically within the 1σ formal error, and therefore not significant. It is interesting to note that the noise of the normalized observation residuals (RMS) seems to decrease with increasing elevation despite the fact that we use elevation-dependent weighting for the observations.

We then artificially changed the satellite phase center offsets of all satellites by one meter. In Table 5.4 we see that this change has a large impact on both, the terrestrial scale and the tropospheric zenith delays. The scale changed by 8 ppb (50 mm in station height) and

Differences w.r.t. Reference Solution				
Solution Description	Scale (ppb)	Tropos. (mm ZPD)	Z-off (m)	RMS (mm)
Scale Fixed	0.1	0	-	1.46
Scale Free, 15^o cut-off	-0.3	1	-	1.40
Scale Free, 20^o cut-off	-1.0	4	-	1.36
Scale Free, Z-off. +1 meter	-8.3	5	(+1.0)	1.46
Scale Fixed, Z-off Est.	1.5	-1	-0.2	1.44
Scale Free, Z-off Est.	13.2	-7	-1.6	1.44
Scale Free, Z-off Est. 15^o cut-off	17.0	-12	-2.0	1.39
Scale Free, Z-off Est. 20^o cut-off	22.8	-18	-2.5	1.34
Scale Fixed, Abs. P.C. Var.	8.5	-10	-	1.57
Scale Free, Abs. P.C. Var.	14.3	-18	-	1.53
Scale Fixed, Abs. P.C. Var., Z-off. Est.	-1.4	-9	2.1	1.49
Scale Free, Abs. P.C. Var., Z-off. Est.	-29.7	9	5.5	1.46

Table 5.4: Influence of small processing changes on the terrestrial scale, tropospheric zenith delay, and satellite antenna offset.

the zenith delays were changed by 5 mm (15 mm in station height). A comparison of the station coordinate estimates showed that they agreed at the few mm level after a 7 parameter transformation. Apart from the scale change of 8 ppb the coordinate transformation showed a significant translation in the Z-direction of 5 mm. A comparison of the orbit estimates, without any parameter transformation, showed that they agreed on the mm level, which is remarkable considering the relatively large changes in the other parameters. These results underline the strong correlation between the satellite antenna phase center offset, the terrestrial scale, and the tropospheric zenith delays.

We then made the attempt to estimate the phase center offset of the satellites by estimating one offset for each individual satellite. It should be mentioned that the observability of this offset is rather poor due to the fact that the "observation angle" between the satellite–receiver and satellite–geocenter vectors is at maximum 14^o. This means that the major part of the Z-offset is a range bias which may be absorbed by ambiguities or clocks. In this context the test, where we changed the Z-offset by one meter, is quite convincing. Only 70 mm of the one meter change showed up in the results.

The remaining effect of the Z-offset will have an elevation-dependent signature because the observation angle increases with decreasing satellite elevation. This elevation-dependent signature explains the correlation between the Z-offset and the estimated tropospheric delays. In addition, it is well known that the tropospheric delays correlate with the station heights and therefore also with the terrestrial scale. The results of the four tests which were performed with Z-offset estimation are quite remarkable. If the scale of the terrestrial network is constrained the results look quite reasonable. However, as soon as this scale is freed the results differ quite significantly from the reference solutions with changes of 22 ppb in scale, 18 mm in zenith delay, and more than 2 m in satellite antenna phase center offset. Notice that the formal errors of the station heights (3–6 mm) and the tropospheric zenith delays (1–2 mm) barely change. The formal errors of the Z-offset estimates are a few centimeters only, increasing strongly with growing cut-off angle (from 40 to 70 mm going from 10^o to 20^o). Apart from the scale change the coordinate transformation again showed significant translations in the Z-direction of up to 15 mm. Also the orbits were now different but only by 20 mm in RMS without showing significant orientation differences. The pronounced elevation-dependency of the results is quite disturbing.

At last we introduced the absolute receiver phase center offset and variations from anechoic chamber measurements. Earlier investigations had shown that the introduction of these absolute phase center measurements gave rise to a 15 ppb terrestrial scale in the GPS analysis [*Rothacher et al.*, 1995*b*]. In the earlier tests we noticed that the satellite antenna offsets also cause large scale effects in the terrestrial network. We therefore hoped to find a solution for the satellite antenna offset which would enable us to use the absolute phase center measurements without any residual effects on the terrestrial scale and the estimated tropospheric zenith delays. The results of these tests are also documented in Table 5.4.

The first two solutions, where we introduced the absolute phase center variations, confirm the fact that these give a 15 ppb terrestrial scale change and also large changes in the tropospheric delays. It is remarkable that, in the solution where the scale is constrained, the change of the scale is as large as 8 ppb! Notice also, that the RMS of these solutions is increased.

In the latter two solutions we solved for the satellite phase center offset in addition to introducing the chamber measurements. The solution with the constrained terrestrial scale looks quite acceptable although the Z-offset change of 2 meters is large. However, the minimal constrained solution shows a dramatic scale change of almost 30 ppb (180 mm station height). Also, the estimated Z-offset is very large (5 m). This solution is not acceptable. Obviously we are still not in a position to use the absolute phase center variations.

We conclude that it is not feasible to accurately solve for the satellite antenna offsets in an absolute sense due to the correlation with the terrestrial scale, the tropospheric delays, the receiver antenna phase center offsets, and elevation-dependent variations. However, we are able to solve for these offsets in a relative way, e.g., by adopting a specific value for a single satellite. The offsets of the other satellites may then be determined relative to this adopted value. Significant Z-offset differences were observed between the individual satellites. Two other IGS ACs, GFZ and JPL, which also estimated the satellite antenna offsets, observed very similar differences for individual satellites [*Bar-Sever*, 1998]. We furthermore conclude that biases observed in the terrestrial scale and tropospheric delays, based on GPS microwave measurements, are very likely the result of inaccurately known phase center positions of both, the satellite and the receiver antennas.

Products	Predicted	Rapid	Final	Units	Biases
Orbit	50.0	10.0	5.0	cm	10.0
Clock	150.0	0.5	0.3	ns	?
Pole		0.2	0.1	mas	0.3
LOD		30.0	20.0	μs/d	20.0
Stations Hor.			3.5	mm	10.0
Stations Vert.			8.0	mm	20.0
Troposphere ZPD			4.0	mm	6.0
Geocenter X, Y			7.0	mm	20.0
Geocenter Z			13.0	mm	50.0
Terrestrial Scale			0.4	ppb	15.0

Table 5.5: Estimated quality of the IGS products.

5.3 Summary

In this chapter we have shown that significant improvements, in only a few years time, were observed for many of the IGS products. In Table 5.5 we summarized the “state of the art” of the IGS products. For completeness we included the predicted and rapid products. For more information about these IGS products we refer to [*Kouba and Mireault*, 1998*b*]. The quality assessment of the tropospheric delays is based on the work done by the IGS working group for combination of tropospheric estimates [*Gendt*, 1998]. The left hand part of Table 5.5 lists the different IGS products and their current precision estimate. The precision indications are based mainly on the IGS internal comparisons and on what we have shown in this chapter.

In order to get an idea of the accuracy of the IGS products, we include the column “biases”, containing estimates for systematic effects which are based on other than GPS observations. These values should be viewed as maximum errors which might be present in IGS products. For instance, the orbit Y-shift of 100 mm is listed as bias although it does no longer appear in most of the IGS products. It is included in the table because its origin is still largely unexplained. Also the terrestrial scale bias (15 ppb) is not really observed in the IGS products. It occurs, when the phase center variation measurements from anechoic chamber tests are introduced, in a correct way, in the processing. The uncertainties for the station positions reflect the systematic effects observed in the coordinate time series, some of which are caused by multipath, giving rise to yearly signals in the residuals. Other effects are caused by minor changes at the site like, e.g., antenna or receiver replacements, cabling changes, antenna radomes, infrastructure changes.

We have seen that the internal consistency between the IGS ACs has reached the 30–50 mm level for orbits, 3–8 mm for station positions and 0.1 mas for polar motion. However, significant biases exist between the AC solutions. Differences of 0.5 ppb (10–15 mm) in the scale of the orbits, 3 ppb (15–20 mm) in the terrestrial scale, and 100 mm in geocenter are observed in internal comparisons.

Biases also show up in comparison with other techniques, e.g., VLBI and SLR. In these external comparisons a bias of 0.3 mas for the X-component of the pole is observed as we have seen in the previous section. Furthermore, a persisting 50 mm bias is present between SLR range measurements and the ranges to the GPS satellites derived from the IGS orbits, a topic we will study in Chapter 7.

We have demonstrated that the realization of the terrestrial reference frame, ambiguity fixing, orbit modeling, elevation cut-off angle, and troposphere modeling play an important role in the quality of the IGS products. We are convinced, however, that we have not yet reached the full potential of the GPS system and that we can still significantly improve the precision of the IGS products. Possible improvements for the next years are:

- Improved realization of the (IGS) terrestrial reference frame.
- More fixed ambiguities by performing ambiguity fixing on longer baselines or by reducing the average baseline length.
- Orbit model improvements resulting in a reduction of the number of estimated orbit parameters (see Chapter 6).
- Lower elevation cut-off angle (3^o).
- Troposphere modeling including gradients.
- Antenna phase center calibration.

In addition, we may expect improvements from the inclusion of GLONASS microwave observations mainly thanks to the increased number of satellites. Last but not least, the inclusion of SLR observations from both, the GPS and GLONASS satellites, may have an impact on the results. The use of SLR observations will be discussed in Chapter 7.

6 Solar Radiation Pressure Models

Solar radiation pressure (RPR) is the largest non gravitational acceleration acting on the GPS satellites. Table 3.1 in Chapter 3 shows the effect of different perturbations on the GPS orbits. The size of the perturbation caused by solar radiation pressure is only exceeded by the effect of the Earth oblateness, the gravitational effects from Sun and Moon and the lower harmonics (C_{22} and S_{22}) of the Earth gravity field. Clearly, for GPS satellites the establishment of an accurate solar radiation pressure model is equally important as an accurate gravity model of the Earth.

6.1 Solar Radiation Pressure

The acceleration of a GPS (or GLONASS) satellite due to the radiation pressure of the Sun is difficult to model because of the complicated shape of these satellites. According to *Rothacher* [1992] it may be expressed as follows:

$$\vec{a}_{RPR} = \nu \cdot \left(P_s \cdot C_r \cdot \frac{A}{m} \cdot \frac{a_s^2}{|\vec{r} - \vec{r}_s|^2} \cdot \frac{\vec{r} - \vec{r}_s}{|\vec{r} - \vec{r}_s|} \right) \tag{6.1}$$

where:

ν ... Eclipse factor ($\nu = 1$ if satellite in sunlight, $\nu = 0$ if satellite in the Earth's shadow, $0 < \nu < 1$ if satellite in penumbra).
A ... Cross-section area of the satellite as seen from the Sun.
m ... Mass of the satellite.
a_s ... Astronomical unit (AU).
$P_s = S/c$ ... Radiation pressure for a completely absorbing object at the distance of 1 AU with $A/m = 1$. S is the solar constant and c the velocity of light.
C_r ... Reflection coefficient.
$\vec{r}, \vec{r}_s$ ... Geocentric coordinate vectors of the satellite and the Sun, respectively.

The acceleration $\vec{a}_{RPR}$ always points in the direction Sun–satellite in this model. Whereas for a spherical satellite the ratio A/m remains constant, the total cross-section area A for a GPS satellite is constantly changing due to the changing attitude of the satellite. The pressure exerted by the solar radiation will therefore vary over one revolution as well as over the year because of the changing orientation of the orbital plane with respect to the Sun.

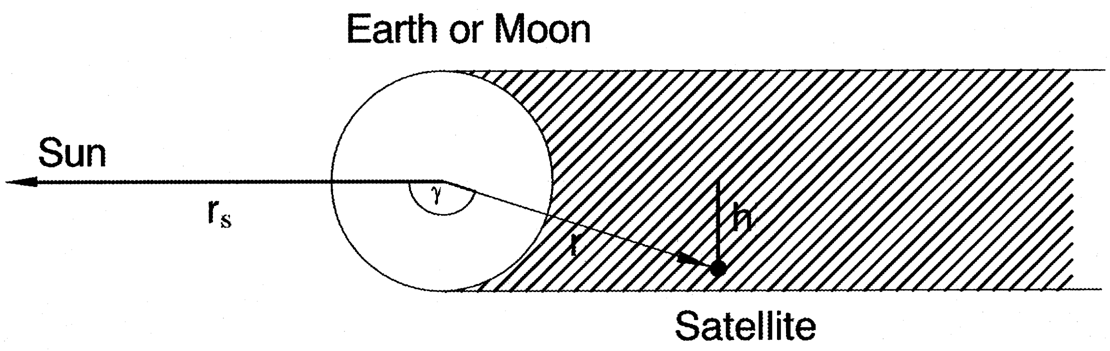

Figure 6.1: Simple cylinder model of the Earth's shadow.

6.1.1 Satellite Eclipses

Because of their high altitude GPS satellites are almost permanently in the sunlight. Only if the vector Sun–satellite lies almost in one of the orbital planes, the satellites of this plane will pass through the Earth's shadow once per revolution. Such "eclipse seasons" happen twice per year for a specific orbital plane and they last for a few weeks. One shadow passage lasts for 55 minutes at the maximum. It is obvious that during the eclipse no solar radiation pressure is exerted on the satellite. According to a simple cylinder model for the shadow of the Earth (see Figure 6.1), the eclipse factor may be computed as:

$$\nu = \begin{cases} 0 \quad \text{if} & \cos\gamma = \dfrac{\vec{r}\cdot\vec{r}_s}{|\vec{r}|\cdot|\vec{r}_s|} < 0 \quad \text{and} \\ & h = |\vec{r}|\,\sqrt{1-\cos^2\gamma} < a_e \\ 1 \quad \text{else} & \end{cases} \tag{6.2}$$

where:

$\vec{r}$ ... Geocentric position vector of the satellite.
$\vec{r}_s$ ... Geocentric position vector of the Sun.
a_e ... Equatorial radius of the Earth.

Figure 6.2 illustrates the body-fixed coordinate system. This satellite-fixed system has its origin in the center of mass of the satellite. The nominal satellite attitude is such that the Z-axis (antenna axis) is pointing to the center of the Earth. The Y-axis, which points along one of the solar panel beams, is perpendicular to the Sun–satellite vector. The X-axis, which is positive toward the half plane that contains the Sun, completes a right-handed system. Earth and Sun sensors monitor the positions of the two celestial bodies. Momentum wheels are used to control the satellite attitude.

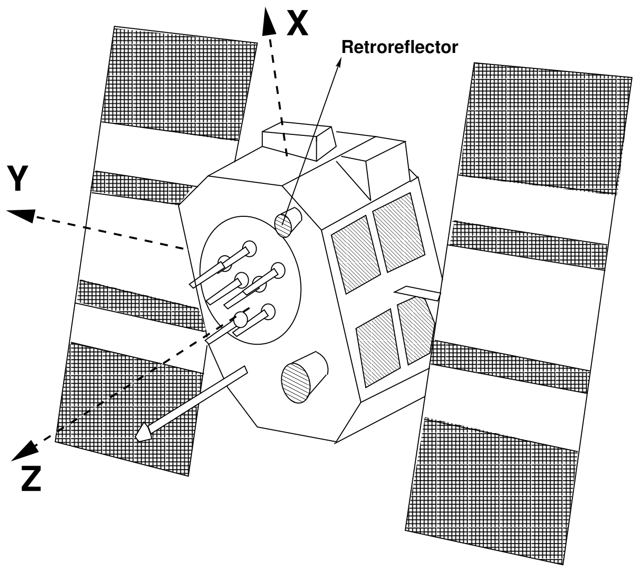

Figure 6.2: Schematic picture of a GPS Block II satellite showing the satellite fixed reference frame.

As soon as the satellite enters the Earth's shadow, maintenance of the correct orientation of the Y-axis becomes impossible. Since June 1994 (see IGSMAIL # 591), the satellites are rotating around the Z-axis with the maximum speed possible (about 0.1 deg/sec) during the shadow passage. Consequently the satellites exit from the Earth's shadow with an almost arbitrary orientation of the solar panels. Until the satellite has regained its nominal attitude, the mis-orientation of the solar panels causes orbit modeling problems. The realignment of the satellite attitude may take up to 30 minutes and causes most of the modeling problems related to the satellite eclipses [*Fliegel and Gallini*, 1996].

6.1.2 Earth Albedo Radiation

The Earth and its atmosphere reflect a large portion of the solar radiation back into space. This re-radiation is called the Earth albedo radiation. The radiation pressure on the satellite due to the albedo of the Earth is very difficult to model due to the distribution of land, ocean, and clouds. According to *Fliegel and Gallini* [1996] the effect of Earth albedo radiation is a function of the Sun–Earth–satellite angle. The maximum albedo radiation is observed during the satellite eclipse season where it may reach 2% of the direct solar radiation pressure. Note that during the eclipse season the satellite sees the Earth in "full phase" for part of its orbital revolution. Up to now Earth albedo radiation has been ignored in GPS orbit determination.

Component	Block I	Block II	Block IIA	Block IIR	GLONASS
Solar panels (m^2)	5.583	10.886	10.886	13.60	23.62
Panel masts (m^2)	0.470	0.985	0.985	0.32	-
Z-side (m^2)	1.510	2.881	2.881	3.75	1.02
X-side (m^2)	1.055	1.553	1.553	3.05	3.18
Mass (kg)	520	880	975	1100	1400

Table 6.1: Dimensions of different GPS and GLONASS satellites.

6.2 The ROCK Models

The most commonly used RPR-models were developed by Rockwell International, the spacecraft contractor for Block I and II satellites [*Fliegel et al.*, 1992]. The computer programs that embody these models became known for Block I as ROCK4 [*Fliegel et al.*, 1985], and for Block II as ROCK42 [*Fliegel and Gallini*, 1989], although they are also known as the Porter models. A distinction is made between the standard S-model and the T-model The latter includes thermal re-radiation of the satellite and is recommended by the IERS Standards [*McCarthy*, 1992].

The ROCK models were derived by first computing the contributions to the radiation pressure from all the major surfaces of the GPS spacecraft taking into account the reflectivity properties of these surfaces. All surfaces are assumed to be either flat or cylindrical. The angular distribution of the reflected sunlight from each surface is approximated as the sum of two "beams", one perfectly diffuse (Lambert scattering) and the other purely specular. Shadowing effects are also accounted for but only to the first order. Figure 6.3 shows the major surfaces of the GPS spacecraft and some of their properties and Table 6.1 lists some of the most important dimensions of the different GPS Block types. The resulting accelerations were represented using relatively simple formulas in a satellite-fixed coordinate system (Figure 6.2). Assuming perfect attitude control the resulting solar radiation force will always lie in the (X, Z) plane. The satellite is oriented such that the Sun is in the satellite's plane of symmetry so that the angle between the Sun and the satellite antennas (Z-axis) is always between 0^o and 180^o. When this angle, α, is less then about 14^o, the satellite is eclipsed. To keep the angle α within the specified range the satellite has to rotate around its Z-axis. During the eclipse period the satellite has to rotate 180^o around its Z-axis in a short time, twice per orbital revolution; once during the actual eclipse ($\alpha = 0^o$) and the second time when it crosses the Sun–Earth plane on the opposite side of the Earth ($\alpha = 180^o$). These rotations are referred to as midnight- and noon-turn, respectively. For the Block IIR satellites the attitude control is changed which will allow the angle α to cover the full range of 0^o to 360^o. This means that there will be no midnight- and noon-turns for these satellites, anymore.

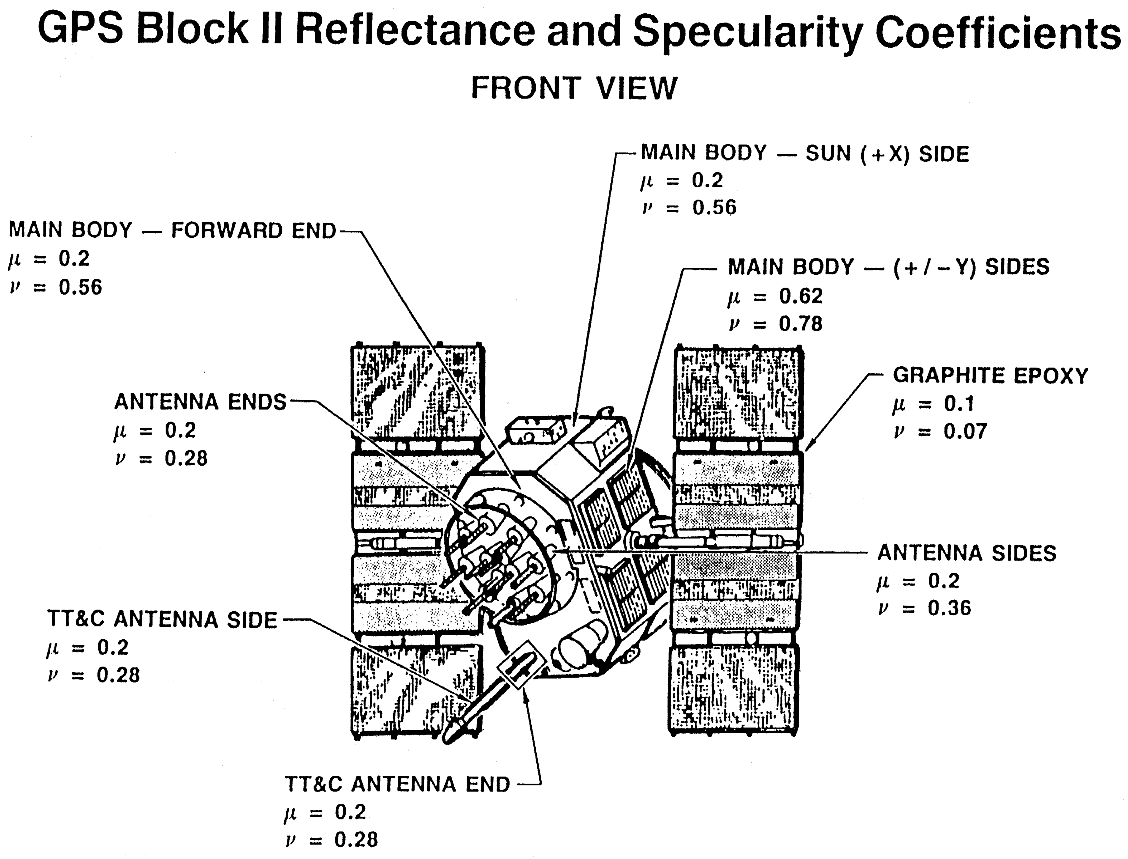

Figure 6.3: GPS Block II surfaces and their properties (from [*Fliegel*, 1993]).

6.2.1 Model Characteristics

The ROCK4 and ROCK42 models, realized originally through two Fortran subroutines, can be represented with high precision as a short Fourier series as function of the angle α. From both models there are two versions, the original or standard versions, S10 and S20, and two versions including the effects of thermal re-radiations, T10 and T20. The "S" and "T" stand for standard- and thermal-model, respectively, the 1 and 2 reflect the Block type, and the "0" indicates that this is the zeroth release of the model. For the new Block IIR satellites the model is called T30. The inclusion of the thermal re-radiation in the ROCK models should have improved the models significantly. Therefore, only the three "T" models will be reproduced and studied here.
The T10 model:

$$\begin{aligned} F_x &= S\,\{-4.55\sin\alpha + 0.08\sin(2\alpha+0.9) - 0.06\cos(4\alpha+0.08) + 0.08\} \\ F_z &= S\,\{-4.54\cos\alpha + 0.20\sin(2\alpha-0.3) - 0.03\sin(4\alpha)\} \end{aligned} \tag{6.3}$$

The T20 model:

$$\begin{aligned} F_x &= S\,\{-8.96\sin\alpha + 0.16\sin 3\alpha + 0.10\sin 5\alpha - 0.07\sin 7\alpha\} \\ F_z &= S\,\{-8.43\cos\alpha\} \end{aligned} \tag{6.4}$$

The T30 model:

$$\begin{aligned} F_x &= S\,\{-11.0\sin\alpha - 0.2\sin 3\alpha + 0.2\sin 5\alpha\} \\ F_z &= S\,\{-11.3\cos\alpha + 0.1\cos 3\alpha + 0.2\cos 5\alpha\} \end{aligned} \tag{6.5}$$

where:

F_x ... Force in the satellite-fixed X-direction ($10^{-5}N$).
F_z ... Force in the satellite-fixed Z-direction ($10^{-5}N$).
α ... Angle between the Sun and the +Z-axis (radians).
S ... Model scale factor. It is advised to estimated a scale factor from the measurements as a quantity that changes slowly over a few weeks.

6.2.2 The Y-Bias

For high precision geodetic work it is advised to estimate a force in the Y-direction, called the Y-bias, in addition to the scale factor (S). Like the scale parameter, the Y-bias should be estimated from the measurements as an acceleration that changes slowly over a few weeks. Although the source of the Y-bias is unknown, its effect on the orbit is significant. The attitude control of the satellites is based on a feedback loop between solar sensors (on the panels) and momentum wheels. Although in theory the Y-axis of the satellites should always be perpendicular to the direction Sun–satellite (to optimize the amount of energy collected by the

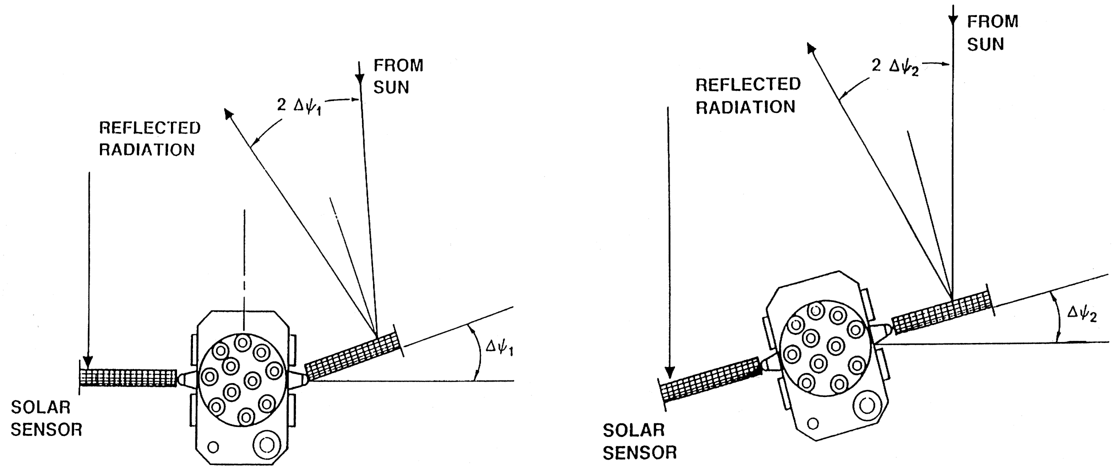

(a) Solar panel misalignment

(b) Solar sensor misalignment

Figure 6.4: Two possible causes of the Y-bias (from [*Fliegel*, 1993]).

solar panels), this is only approximately true in practice. A small mis-orientation of the solar panels will cause an acceleration acting in the direction of the Y-axis. Two possible causes are shown in Figure 6.4, taken from [*Fliegel*, 1993].

The most likely explanation for the Y-bias is the solar sensor misalignment, especially in view of the reported solar sensor biases (see IGSMAIL # 591) which do cause a small misalignment of the satellite. A misalignment error of only 0.5^o would explain the observed Y-bias.

6.2.3 Accuracy of the ROCK Models

Taking the nominal value of $a_{RPR} = 1 \cdot 10^{-7} m/s^2$ for the solar radiation pressure and the claimed accuracy of 3% for the T20 model, the expected error is approximately $3 \cdot 10^{-9} m/s^2$. Furthermore, the size of the Y-bias, which is not included in the ROCK models, is about $1 \cdot 10^{-9} m/s^2$. A similar test as the one used in Chapter 3 to demonstrate the different perturbing effects, was performed to give an idea of the expected orbital errors resulting from the errors in the ROCK model. First a reference orbit was generated by integrating a given set of osculating Keplerian elements over a time period of 24 hours using a standard orbit model. For this purpose the full GPS satellite constellation of January 1, 1998 was used. Next, the same set of osculating Keplerian elements was integrated over the same time period of 24 hours changing the ROCK models by 3% and adding the Y-bias acceleration.

The RMS difference between the perturbed orbit and the reference orbit over the full 24 hour arc is given in Table 6.2. The effects are significant. We have to keep in mind that

Error Source	Magnitude (cm)			
	Radial	Along	Cross	Total
Solar Radiation Pressure (3%)	94	280	11	296
Y-bias	51	364	12	368

Table 6.2: Estimated orbit errors due to ROCK model deficiencies.

the ROCK models were developed for pseudo-range orbit estimation. Using pseudo-ranges the orbit estimates have an accuracy of about 1 meter. For this type of accuracy the ROCK models are adequate provided the scale factor and the Y-bias are estimated. For accuracies routinely achieved by the IGS the residual errors are not acceptable. The estimation of the scale factor and the Y-bias are a minimum requirement for applications of GPS which require highly accurate orbits.

6.2.4 Outgassing

After the launch of a satellite the direct solar radiation estimates of the new satellite exceed the expected values by about 10%. Only after a few weeks the nominal values are approximately reached. Similar effects may also be observed for the Y-bias estimates. The most likely explanation for this phenomenon is the leaking of gas, called outgassing. According to *Fliegel and Gallini* [1996] the multi-layer insulation of the GPS satellites is the most likely candidate to explain the observed effects. The authors also conclude that, because most satellites have a multi-layer insulation, this should affect all satellites in the same way. They therefore predict that the Block IIR satellites should show a similar behavior.

The direct solar radiation (D0) and Y-bias (Y0) estimates of PRN 10 and PRN 13 are given as a function of time in Figure 6.5. PRN 10, a Block IIA satellite, was launched (see Table 2.1) on 16 July 1996, whereas PRN 13, the first Block IIR satellite, was launched on 22 July 1997. Our estimates for PRN 10 clearly show the effects which are supposedly caused by outgassing in both, the direct solar radiation, and the Y-bias estimates. For PRN 13 no such effects may be observed. The conclusions by *Fliegel and Gallini* [1996] is thus not supported by our results.

6.3 The Extended CODE Orbit Model

The experiences gained at CODE during the first year (1992-1993) of IGS operations indicated that the standard orbit model, six Keplerian elements and two RPR-parameters, was not sufficient for 3-day arcs. This was the motivation for the development of an extended orbit model.

In *Beutler et al.* [1994*b*] the Extended CODE Orbit Model (ECOM) is presented and discussed in detail, therefore only the basic characteristics are summarized here. The considerations behind the ECOM are similar to those underlying the Colombo model [*Colombo*,

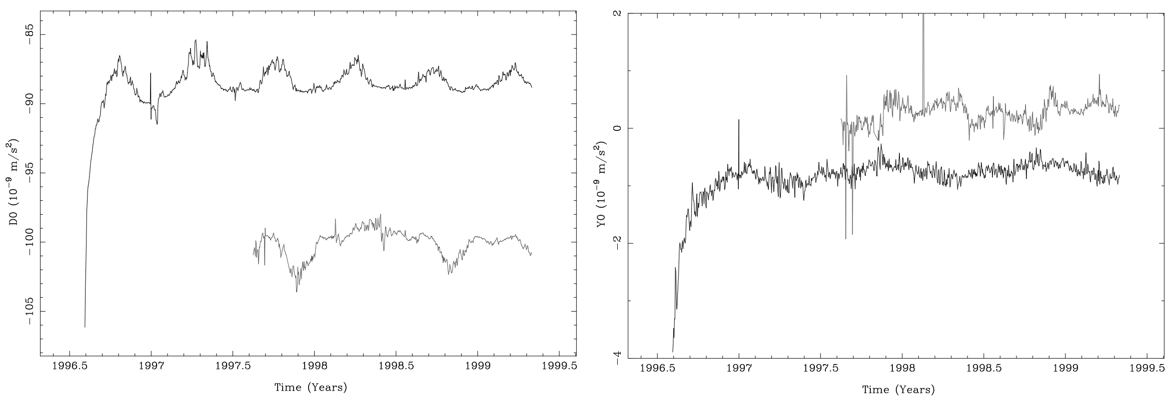

(a) Solar radiation pressure estimates

(b) Y-bias estimates

Figure 6.5: The effect of outgassing on the solar radiation pressure parameters D0 and Y0 for PRN 10 (Block IIA, solid line) and PRN 13 (Block IIR, dashed line).

1989]. The principal difference resides in the fact that the ECOM considers solar radiation pressure as the major "error source" for the orbits, whereas the gravity field of the Earth plays this role in the Colombo model. The Colombo model uses the radial, along- and cross-track directions as the three orthogonal directions whereas the D-, Y-, and B-directions are used by the ECOM. *Beutler et al.* [1994*b*] demonstrated that the performance of the ECOM is superior to that of the Colombo model, which clearly shows that solar radiation pressure is the major error source for GPS satellite orbits. In the ECOM, the acceleration $\vec{a}_{RPR}$ due to the solar radiation pressure (RPR) is written as:

$$\vec{a}_{RPR} = \vec{a}_{ROCK} + D(u) \cdot \vec{e}_D + Y(u) \cdot \vec{e}_Y + B(u) \cdot \vec{e}_B \tag{6.6}$$

where $\vec{a}_{ROCK}$ is the acceleration due to the ROCK models, and

$$\begin{aligned} D(u) &= D0 + DC \cdot \cos u + DS \cdot \sin u \\ Y(u) &= Y0 + YC \cdot \cos u + YS \cdot \sin u \\ B(u) &= B0 + BC \cdot \cos u + BS \cdot \sin u \end{aligned} \tag{6.7}$$

where D0, DC, DS, Y0, YC, YS, B0, BC, and BS are the nine parameters of the ECOM, and

$\vec{e}_D$ … Unit vector satellite–Sun, positive towards the Sun.
$\vec{e}_Y$ … Unit vector along the spacecraft solar-panel axis.
$\vec{e}_B$ … Unit vector defined by: $\vec{e}_B = \vec{e}_D \times \vec{e}_Y$
u … Argument of latitude of the satellite.

The ECOM is a generalization of the standard orbit model which uses only two parameters to account for the solar radiation pressure, namely D0 and Y0. Note that the Y-direction of the ECOM corresponds to the Y-direction of the body-fixed coordinate system.

Although not really a solar radiation pressure model in the sense of the ROCK models, the ECOM does consider the solar radiation pressure to be the major perturbing force acting on the GPS satellites. Therefore, the ECOM provides an excellent tool to study the effects of the solar radiation pressure on the GPS satellites. It allows to detect in which direction the RPR-forces act on the GPS satellites.

There are two methods to study the effects of different ECOM parameters on the orbit. The first, and most reliable method, is to use the ECOM in the orbit estimation procedures using GPS observations, very much like the routine orbit estimation performed at CODE for IGS activities. The second method consists of using the satellite positions as provided by the IGS analysis centers as pseudo-observations in an orbit determination step. This second method is less correct but computationally orders of magnitude more efficient than the first method. The generation of a 3-day arc using pseudo-observations takes typically 3 minutes whereas using real observations takes several hours. In the next sections we will use both methods to study the effect of the different ECOM parameters.

6.3.1 Orbit Estimation Using GPS Observations

In 1996 the ECOM was fully implemented into the Bernese GPS Software and first experiences were gained. It was expected that not all nine parameters of the ECOM can (and should) be estimated with 3-day arcs. Initial tests [*Springer et al.*, 1996] indicated that it is best not to solve for the "B-terms", but to estimate the constant and periodic terms in the D- and Y-directions plus small velocity changes in the radial and along-track directions. A careful analysis of the proposed parameterization caused, however, a significant degradation of the quality of the length of day (LOD) estimates. The correlation between estimated orbit (RPR) parameters and LOD, due to the one to one correlation of the ascending node of the orbit and the rotation of the Earth around its spin axis, is a delicate problem [*Rothacher et al.*, 1995*c*].

It was therefore decided to systematically test the effect of different parameter combinations of the ECOM. In *Springer et al.* [1999*b*] a detailed description of the results from two extensive tests using the ECOM may be found. In the first test series small velocity changes, called pseudo-stochastic pulses, were always estimated (stochastic series) whereas in the second test series they were never estimated (deterministic series). Let us summarize the most important results here.

The "stochastic" series showed that the estimation of the constant and periodic terms in the B-direction, in addition to the constant terms in the D- and Y-direction, significantly improves the orbit quality. The improvement was seen in all estimated parameters, orbit, station coordinates, and polar motion, except for the LOD estimates, where a small degradation in quality was observed. The improvement of the orbits was estimated to be a factor of two to three. As a direct consequence of these tests the estimation of the B-terms was implemented for the generation of the CODE contributions to the IGS on 29 September 1996 (see also Chapter 5).

The results based on our routine orbit procedures using the standard and extended (3 B-terms) orbit parameterizations showed that both, the stochastic and deterministic orbit parameters, were much improved with the new orbit parameterization. Improvement means that the size of the stochastic pulses was significantly reduced and that the variation of the Y0-term became much smaller. This is true in particular for the Y-bias (see Figure 6.6) and the radial pseudo-stochastic pulses (see Figure 6.7). These figures cover the time period from day 217 in 1996 to day 129 in 1999, i.e., almost 3 years. The reduced size of the stochastic orbit parameters underlines the quality of the new orbit model. Tests without estimating the radial pseudo-stochastic pulses showed that with the new orbit parameterization these pulses no longer have to be estimated. Considering the fact that pseudo-stochastic pulses are meant to absorb orbit model deficiencies it is clear that the modeling deficits are significantly reduced in the new orbit parameterization. Note, however, that some signature is observed for the estimated along-track pulses, Figure A.1 in Appendix A. This indicates that even in the new model there remain some orbit model deficits.

The deterministic test series confirmed that, from the three directions in which periodic terms can be estimated with the ECOM, the periodic terms in the B-direction most significantly improve the orbit model. Evidence was presented that the periodic signals in the Y-direction reduce the orbit model deficiencies as well. The periodic signals in the B-direction, however, were shown to be more important than those in the Y-direction.

The deterministic test series further showed that a purely “deterministic” orbit parameterization, consisting of the constant terms in the D- and Y-directions plus the periodic terms in the D- and B-directions, gives excellent orbit estimates. Due to the degradation of the LOD estimates this deterministic orbit model is, however, not used for the IGS activities at CODE.

Let us mention that a similar deterministic test series was performed for the satellites of the GLONASS system based on data from the International GLONASS EXperiment (IGEX). The results showed a similar behavior of the parameters of the ECOM for the GLONASS satellites, i.e., estimation of the direct radiation pressure coefficient, the Y-bias, and the periodic terms in the D- and B-direction (parameters D0, Y0, DC, DS, BC, and BS of eqn. (6.7)) gives the best GLONASS orbit estimates. Again, the periodic terms in the B-direction were found to give a very significant improvement, too.

The regular pattern of the estimated RPR parameters, see Appendix A, and the fact that a good non-stochastic orbit parameterization was found, indicate that it may be possible to derive a more physical RPR model for the GPS satellites. This is the topic of the next section.

6.3.2 Orbit Determination Using GPS Orbits as Pseudo-Observations

The goal of the orbit determination using pseudo-observations was to find the optimal orbit parameterization. For this purpose a “standard test” was developed to compare the results. The test is based on a 7-day arc using the CODE final products, i.e., precise orbits plus their respective Earth rotation parameters. The resulting 7-day arc is extrapolated for 48 hours

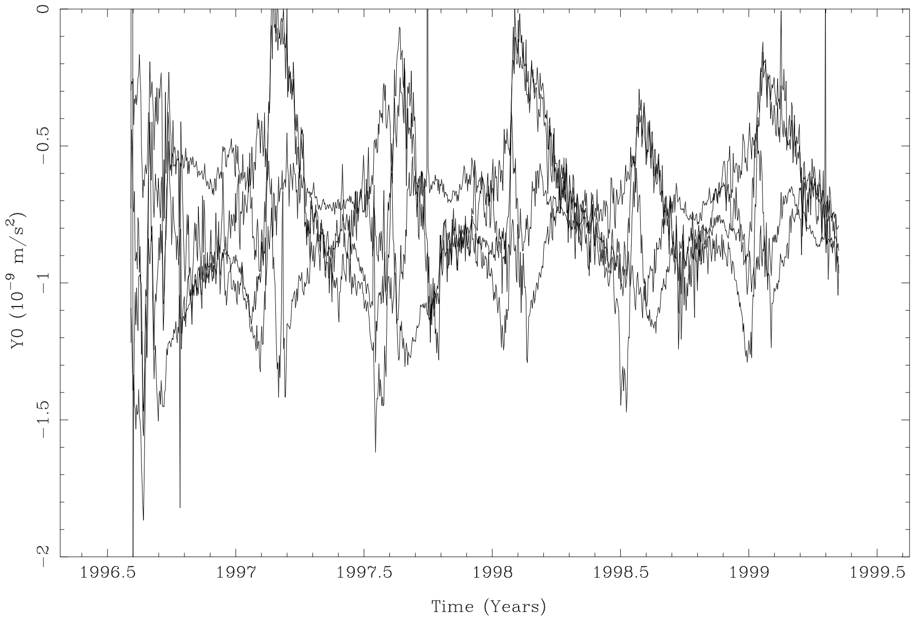

(a) Standard orbit model

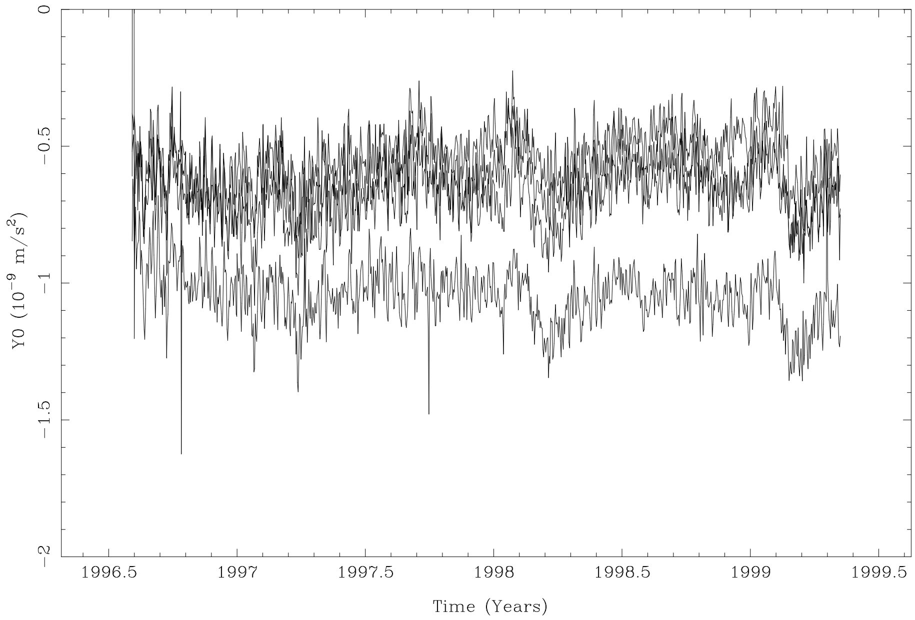

(b) Extended orbit model

Figure 6.6: Estimated Y-bias using the two different CODE orbit parameterizations. Only PRNs 3, 6, 7, and 31 in orbital plane C are shown.

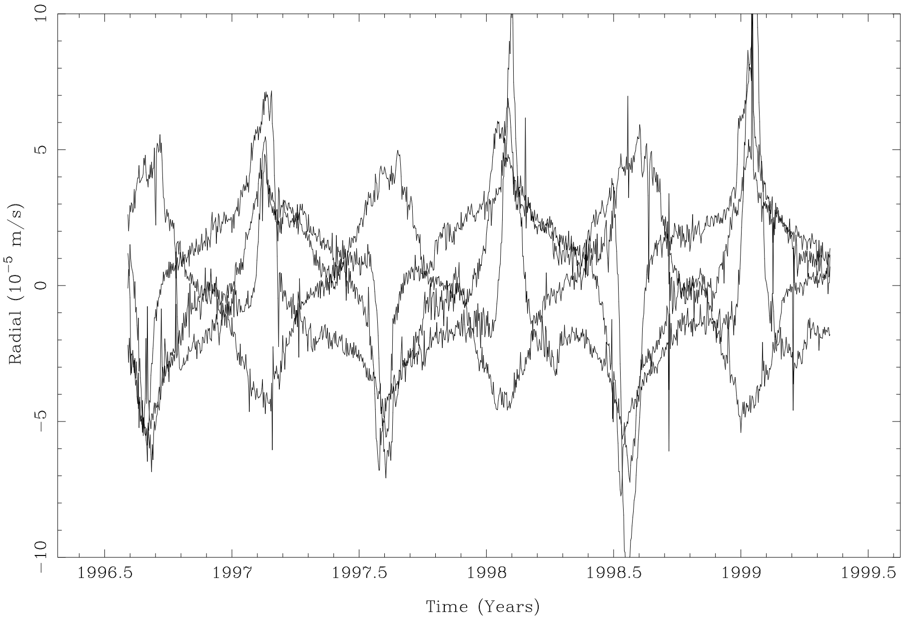

(a) Standard orbit model

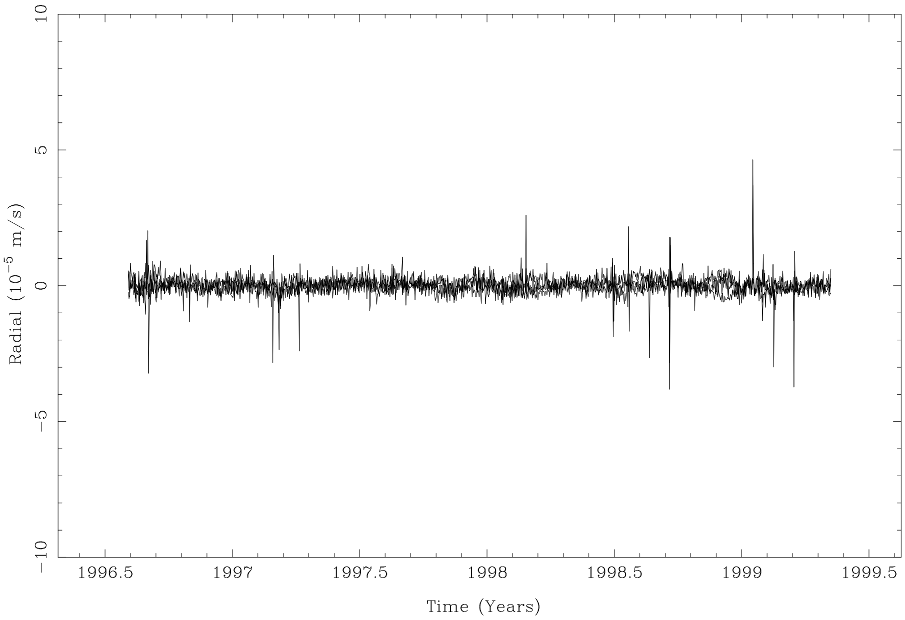

(b) Extended orbit model

Figure 6.7: Estimated radial pulses using the two different CODE orbit parameterizations. Only PRNs 3, 6, 7, and 31 in orbital plane C are shown.

using orbit integration. The last 24 hours of this orbit prediction are compared to the CODE final orbit for that same day. The period from March 13 to March 21 in 1997 was selected as test interval. The following quantities are considered as quality indicators for the orbit parameterization:

- RMS of the residuals of the 7-day fit.
- RMS of the residuals of the predicted orbit relative to the CODE final orbit of the same day.
- Median of the residuals of the predicted orbit relative to the CODE final orbit of the same day.

First, we studied whether the determined orbit gave similar results as the deterministic orbit estimation discussed in the previous section. It was verified that the results were indeed very similar. Only one small anomaly was detected in the estimation of the periodic terms in the Y- and B-directions. Using pseudo-observations the effect of the periodic terms in these two directions are almost identical whereas using real observations a significant difference was observed favoring the periodic terms in the B-direction.

The satellite positions, used as pseudo-observations, are very strong observations for orbit determination. They allow to estimate a large number of orbit parameters. Therefore, our orbit determination program was generalized to estimate periodic terms with periods of one to sex times per orbital revolution. Furthermore, modifications were made to allow for periodic terms in two other coordinate systems: the satellite-fixed reference frame (X, Y, Z) and the "classical" orbit system in radial, along-, and cross-track (R, S, W). In addition, the argument for the periodic terms was slightly changed to account for the position of the Sun with respect to the ascending node. This change is a consequence of the basic assumption that the solar radiation pressure is the major "error source" in GPS orbit modeling. It is therefore logical to relate the time argument of the periodic signals to the position of the Sun in the orbital plane. Thus, the argument of latitude (u) is corrected for the argument of latitude of the Sun in the orbital plane (u_0), see Figure 6.8.

After extensive tests using many different combinations of the available parameters a small set of optimal orbit parameterizations was found. It is interesting to note that model M1 is very similar to the best deterministic orbit parameterization which we found in the previous section. Table 6.3 lists these optimal parameterizations. It is interesting to note that there are no periodic cosine terms listed. This is caused by the fact that the cosine terms are correlated with the estimated D0 terms. All candidate parameterizations were subsequently used in real orbit estimation using one full week of double-difference carrier phase data. These tests confirmed that all 5 parameterizations perform very well apart from some correlation with the LOD estimates. Because of the slightly better performance and its resemblance to the ROCK model, model M5 (Table 6.3) was selected as the optimal orbit parameterization. This optimal parameterization, consisting of six parameters, three constants and three periodic terms,

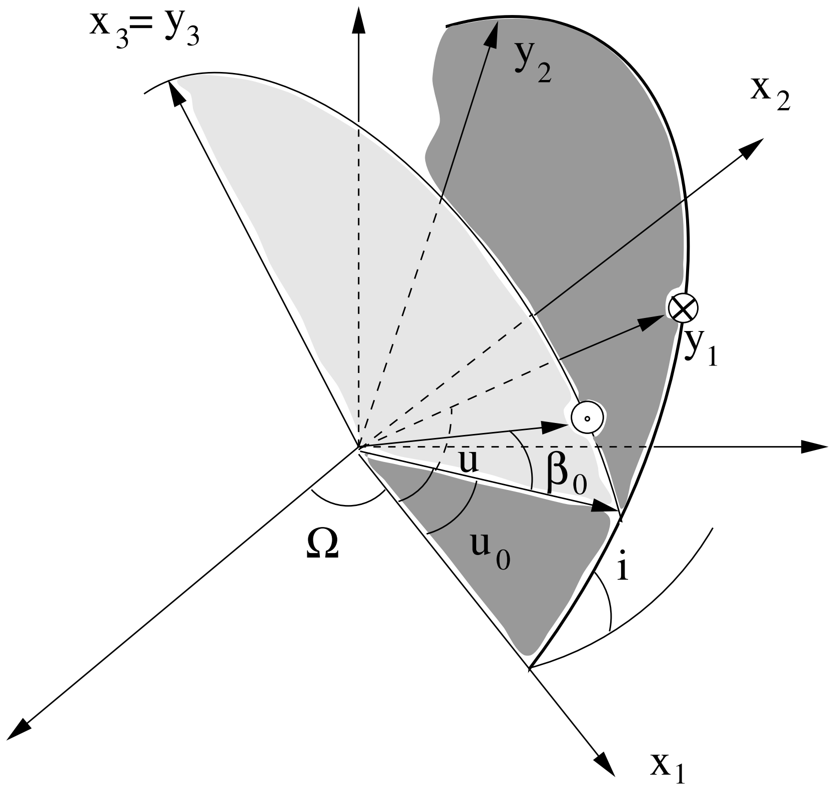

Figure 6.8: Definition of the argument of latitude of the Sun in the orbital plane (u_0) and the elevation of the Sun above the orbital plane (β_0).

Model	Constant Terms	Periodic Terms
M1	D0, Y0, B0	B1 sin($u - u_0$), D1 sin($u - u_0$)
M2	D0, Y0, B0	B1 sin($u - u_0$), B2 sin2($u - u_0$)
M3	D0, Y0, B0	Z1 sin($u - u_0$), X1 sin($u - u_0$)
M4	D0, Y0, B0	Z1 sin($u - u_0$), X3 sin3($u - u_0$)
M5	D0, Y0, B0	Z1 sin($u - u_0$), X1 sin($u - u_0$), X3 sin3($u - u_0$)

Table 6.3: Selected “optimal” orbit parameterizations, see eqn. (6.8).

describes the acceleration $\vec{a}_{RPR}$ due to the solar radiation pressure in the following way:

$$\begin{aligned}\vec{a}_{RPR} &= D0 \cdot \vec{e}_D + Y0 \cdot \vec{e}_Y + B0 \cdot \vec{e}_B + Z1 \sin(u-u_0) \cdot \vec{e}_Z + \\ &\quad \{X1 \sin(u-u_0) + X3 \sin 3(u-u_0)\} \cdot \vec{e}_X\end{aligned} \tag{6.8}$$

where,

$\vec{e}_X$ ... Satellite-fixed X-axis, positive toward the half plane that contains the Sun.
$\vec{e}_Y$ ... Satellite-fixed Y-axis, pointing along the spacecraft solar-panel axis ($\vec{e}_Z \times \vec{e}_X$).
$\vec{e}_Z$ ... Satellite-fixed Z-axis, the vector satellite–Earth, positive towards the Earth.
u_0 ... Argument of latitude of the Sun in the orbital plane, see Figure 6.8.

D0, Y0, and B0 are the three constant terms and Z1, X1, and X3 are the three periodic terms of the model. Note that D0, Y0, and B0 are related to the ECOM, eqn. (6.7), whereas Z1, X1, and X3 are new parameters. Z1 and X1 have a similar behavior as the periodic terms in B and D, respectively.

6.4 Deriving the CODE Solar Radiation Pressure Model

Using the above orbit parameterization (model M5 in Table 6.3) all final CODE orbits with their respective ERPs, as submitted to the IGS since June 1992, were used in an orbit determination step as pseudo-observations. For this purpose an arc-length of 5 days was chosen and no a priori solar radiation pressure model was used. This resulted in a long time series, covering almost 6 years, of estimates for the selected (optimum) set of RPR parameters. It was hoped that, after careful analysis, this time series could be used to derive a new (deterministic) solar radiation pressure model. Figure 6.9 shows the estimated values for the accelerations caused by the direct solar radiation pressure (D0) and the Y-bias (Y0) as function of time over the full 6 years. It should be noted that these estimates are "scaled" to correct for the distance of the satellite to the Sun. Otherwise a clear annual signal would have been observed due to the eccentricity of the Earth orbit.

In Figure 6.9(a) the three Block types can easily be identified. The uppermost curves (smallest D0 values) represent the Block I satellites from which the last one (PRN 12) stopped operations early in 1996. The lowest curves (largest D0 values) represent the Block II satellites. The relatively large difference between the D0 estimates for the Block II and IIA satellites, which are very similar in shape, is caused by the mass difference. The Block IIA satellites are 100 kg more massive (10%) (see Table 6.1). The D0 acceleration should thus be reduced by about 10%, which may indeed be observed in Figure 6.9(a). The increased noise of the D0 estimates as a function of time is caused by those satellites experiencing momentum wheel problems, i.e., PRNs 14, 16, 18, 19, 24, and 29 (see Table 2.1). The D0 estimates for PRN 13 (Block IIR), which may be seen in Figure 6.5, are similar in size to those for the Block II satellites. Figure A.2 in Appendix A shows the D0 estimates for the individual orbital planes. Note that the satellites with momentum wheel problems and solar panel problems (PRN 23) (see Table 2.1), were excluded from Figure A.2 in Appendix A.

Clear jumps may be observed in the Y-bias time series in Figure 6.9(b). Most likely these jumps are related to the "yaw-bias" changes in the attitude system of the GPS satellites. These biases have been kept constant since November 1995 [*Bar-Sever*, 1997]. Prior to November 1995, the GPS operators had routinely changed the sign of the yaw-bias in the satellite attitude control system when the β_0-angle (Figure 6.8) changed sign. Since November 1995 the yaw-bias has been fixed to a value resulting in a yaw-angle of 0.5^o. Furthermore, the eclipse phases can clearly be seen in the Y-bias estimates, which are somewhat anomalous during these phases. Because the eclipse periods of different orbital planes are different, only the satellites in one single orbital plane are shown in Figure 6.9(b). The Y-bias estimates for the six individual orbital planes may be inspected in Figure A.3 in Appendix A. Again the problematic satellites were omitted (PRNs 14, 16, 18, 19, 23, 24, and 29). Figure A.4 in Appendix A also shows the Z1 estimates as function of time for the individual orbital planes.

Figure A.5 in Appendix A shows the effect of the loss of the satellite momentum wheels on the D0, Y0, and Z1 estimates of PRN 14 and PRN 18. Due to this loss the attitude of these satellites is maintained using thruster firings. Because thrusters are never perfectly aligned, this results in a small orbit maneuver which is difficult to model. The estimated orbit parameters thus have to absorb this mis-modeling. Figure A.5 also illustrates why these satellites were left out in the other figures.

A careful analysis of the estimated parameters as a function of time showed that the behavior of satellites within one orbital plane is very similar. This may be seen clearly in Figures A.2, A.3, and A.4 in Appendix A. Annual and semi-annual signals are dominant. Assuming that the Sun causes the observed signals, it is logical to study the behavior of the RPR parameters as a function of the angle β_0 of the Sun above the orbital plane (Figure 6.8). If $|\beta_0| < 14^o$, the orbital plane is partly eclipsed. Due to the obliquity of the ecliptic the variation of the β_0-angle is different for the different orbital planes. The maximum range in the β_0-angle is observed for planes A and F for which $-80^o < \beta_0 < 80^o$. The minimum range is observed for planes C and D, for which $-40^o < \beta_0 < 40^o$. Figure 6.10 shows the variation of the β_0-angle for the different orbital plans for the year 1997.

Figure 6.11 gives the time series for the direct solar radiation pressure and Y-bias accelerations. As opposed to Figure 6.9, where the estimates are given as a function of time, the estimates are now given as function of the angle of the Sun relative to the orbital plane (β_0). For the Y-bias a shorter time interval was selected to exclude the observed jumps from the pre-November 1995 era. All satellites, except the problematic ones, are shown (not only those in one single orbital plane).

The direct solar radiation pressure acceleration and the Y-bias acceleration, as functions of β_0, are very similar for all (Block II and IIA) satellites. This indicates that a simple model may be derived for these parameters. It emerges from Figure 6.12 that the same is true for the constant term in the B-direction and for the once-per-revolution periodic term in the Z-direction. Both periodic signals in the X-direction (X1 and X3) do not show a very clear

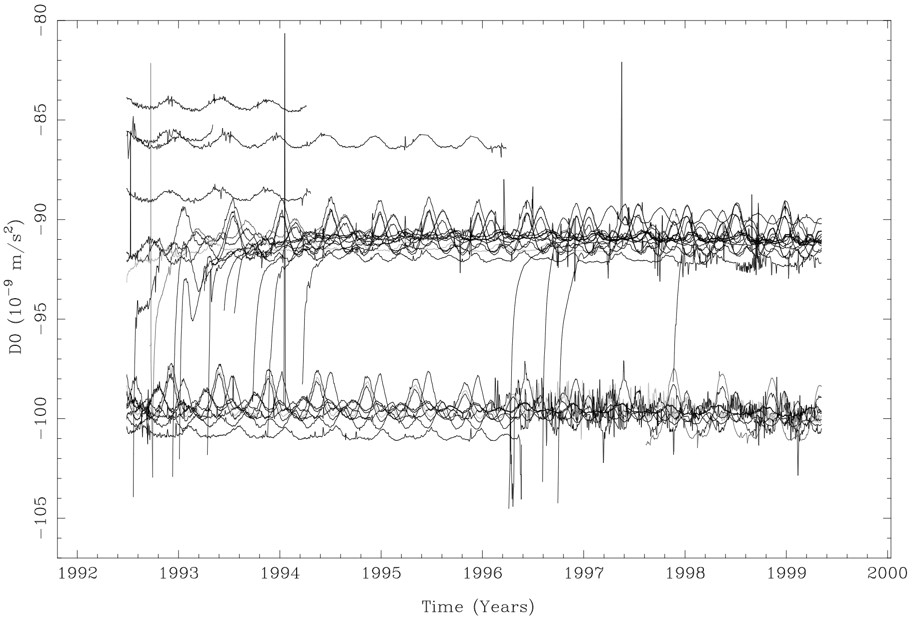

(a) Direct solar radiation pressure acceleration for all satellites

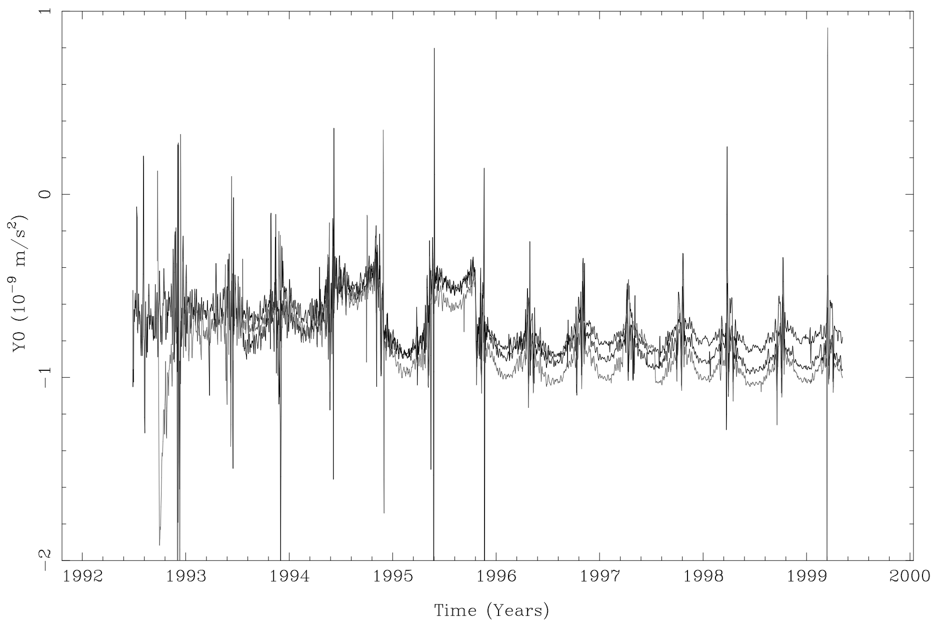

(b) Y-bias acceleration for satellites in orbital plane A (PRNs 9, 25, 27)

Figure 6.9: Estimated direct solar radiation pressure acceleration (D0) and Y-bias acceleration (Y0) as function of time over the interval from June 1992 to May 1999.

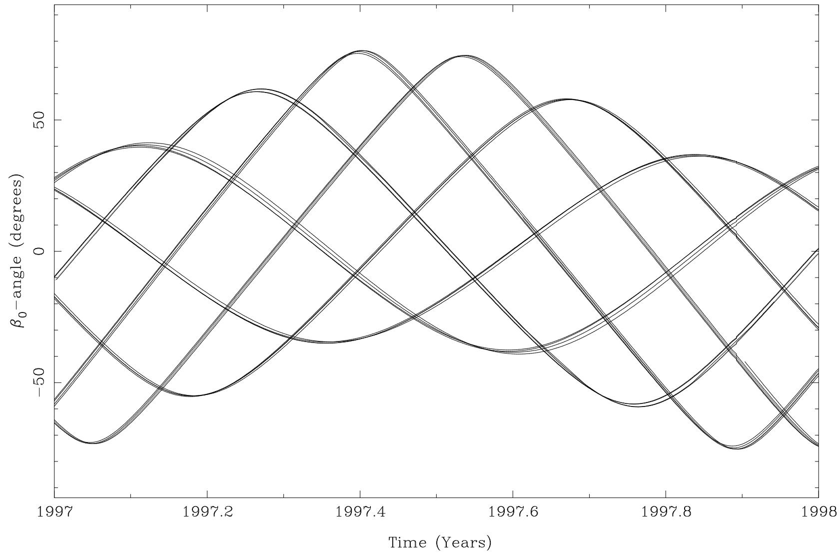

Figure 6.10: Variation of the β_0-angle during the year 1997 for the six individual orbital planes. The first line which reaches its maximum represents orbital plane D. The next maxima represent planes E, F, A, B, and C, respectively.

behavior.

The Block I satellites, represented by the uppermost lines in the D0 estimates shown in Figures 6.9 and 6.11, behave in a slightly different way. Although their behavior is also predictable, no attempt was made to create a model for Block I satellites. Due to the "jumps" in the estimates of the Y-bias, the model for this parameter had to be based on the estimates since 1996 only. It turned out that the performance of the complete model was better if all model parameters were uniquely based on recent results (since 1996). Apparently the modeling improvements made in the previous few years are crucial for our purpose. The "bad" satellites (those experiencing problems with their momentum wheels and PRN 23) were down-weighted in the model estimation to avoid biasing of the model parameters. In addition the estimates from the eclipse periods were also down-weighted, except for the D0 estimates. As can be seen in Figures 6.11 and 6.12 the estimates for the Y0-, B0-, and Z1-terms, are quite different during eclipse seasons. The D0 estimates, however, are not affected by eclipse periods.

The time series since 1996 was used to derive a β_0-dependent function for each of the six parameters of eqn. (6.8). The result may be written as:

$$\begin{aligned} D0(\beta_0) &= D0_0 + D0_{C2}\cos(2\beta_0) + D0_{C4}\cos(4\beta_0) \\ Y0(\beta_0) &= Y0_0 + Y0_{C2}\cos(2\beta_0) \\ B0(\beta_0) &= B0_0 + B0_{C2}\cos(2\beta_0) \end{aligned} \tag{6.9}$$

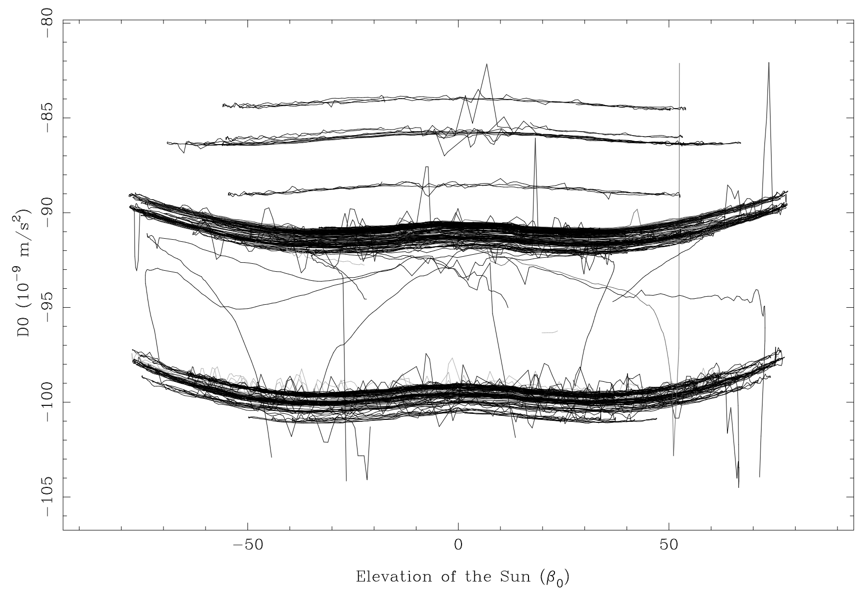

(a) Direct solar radiation pressure acceleration

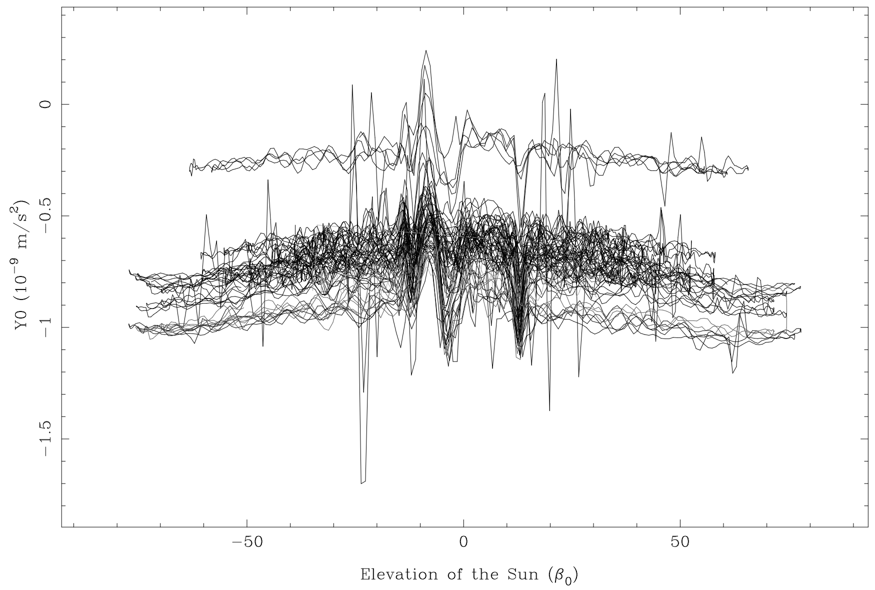

(b) Y-bias acceleration

Figure 6.11: Estimated direct solar radiation pressure acceleration (D0) and Y-bias acceleration (Y0) as a function of the angle of the Sun above the orbital plane (β_0). For D0 the complete interval from June 1992 to May 1999 is shown whereas for Y0 only the last few years (1996–1999) are included.

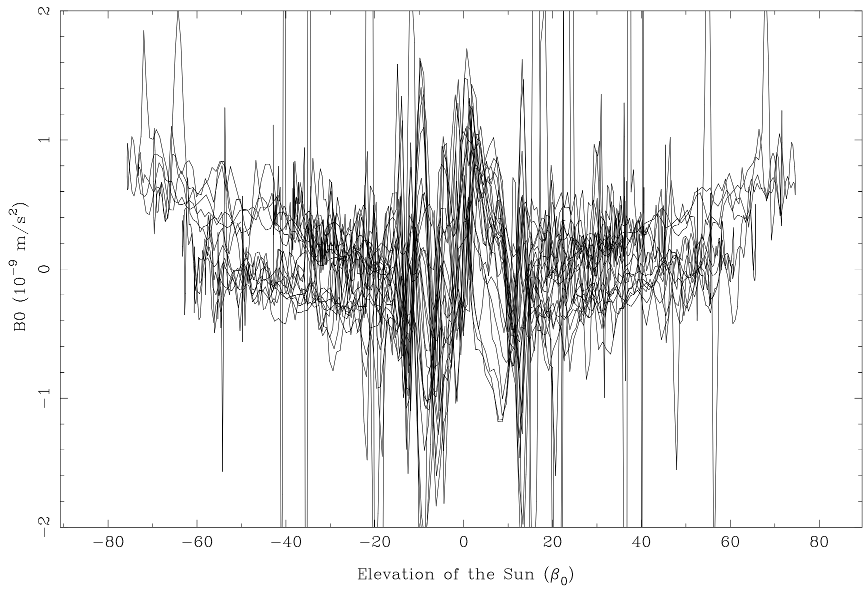

(a) B0 accelerations

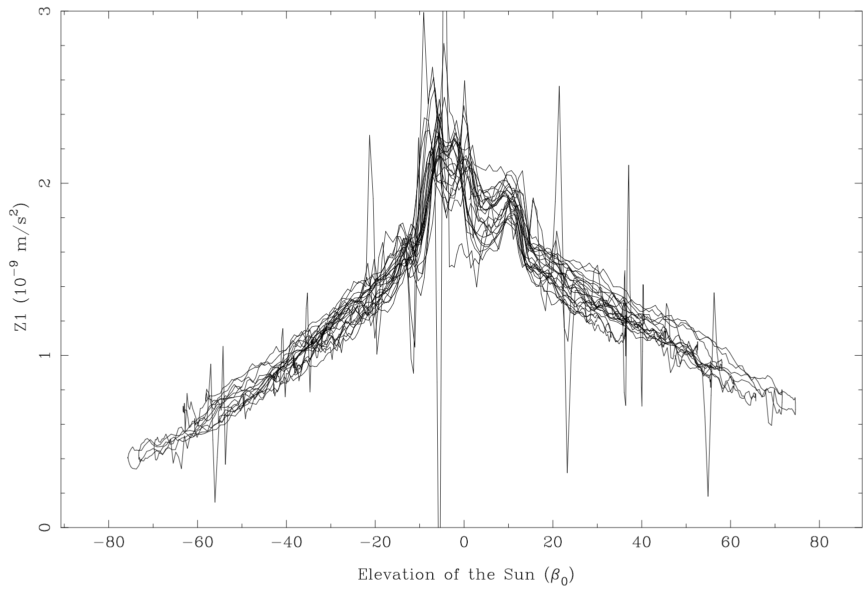

(b) Z1 accelerations

Figure 6.12: Estimated B0 and Z1 acceleration as a function of the angle of the Sun above the orbital plane (β_0). The estimates for PRN 2, 6, 9, 15, and 21, representing orbital planes A–E, are shown. Only estimates of the last few years (1996–1999) are included.

$$\begin{aligned}
Z1(\beta_0) &= Z1_0 + Z1_{C2}\cos(2\beta_0) + Z1_{S2}\sin(2\beta_0) + \\
&\quad Z1_{C4}\cos(4\beta_0) + Z1_{S4}\sin(4\beta_0)
\end{aligned}$$

$$\begin{aligned}
X1(\beta_0) &= X1_0 + X1_{C2}\cos(2\beta_0) + X1_{S2}\sin(2\beta_0) \\
X3(\beta_0) &= X3_0 + X3_{C2}\cos(2\beta_0) + X3_{S2}\sin(2\beta_0)
\end{aligned}$$

Using equations (6.8) and (6.9) the CODE RPR model may now be given in the form:

$$\begin{aligned}
\vec{a}_{RPR} &= D0(\beta_0)\cdot\vec{e}_D + Y0(\beta_0)\cdot\vec{e}_Y + B0(\beta_0)\cdot\vec{e}_B + \\
&\quad Z1(\beta_0)\sin(u-u_0)\cdot\vec{e}_Z + \\
&\quad \{X1(\beta_0)\sin(u-u_0) + X3(\beta_0)\sin 3(u-u_0)\}\cdot\vec{e}_X
\end{aligned} \tag{6.10}$$

Note that the constant terms ($D0_0,\ Y0_0,\ B0_0$) in eqn. (6.9) are satellite-specific and that the $Z1_0$-term is Block-specific. All parameter values are given in Appendix A. Note that the model is only valid for Block II and IIA satellites. Furthermore, the values given for PRN8 should be used with care because this satellite was launched late in 1997 and its short time series is somewhat affected by the "outgassing" effects. The values for satellite PRN23 should be used with care, as well, due to the problems with the orientation of the solar panels. The results indicate, however, that it should be possible to derive a "tailored" RPR model for PRN23. The CODE RPR model has been published in [*Springer et al.*, 1999*a*, 1998]. It was announced by IGSMAIL # 1842.

6.5 Evaluation of the CODE Solar Radiation Pressure Model

Four different investigations were performed to evaluate the new solar radiation pressure model:

- The effect of the parameters of our RPR model on the satellite positions was determined to give an idea of the significance of individual terms.
- Based on the residuals of the RPR series an error budget of the model was derived.
- The model was tested as a priori model in a real parameter estimation process, using one week of GPS observations.
- The model was compared to other RPR models, to check its performance, using our standard test (next section).

The effect of different parameters of the new RPR model on the orbit was estimated by integrating a given set of osculating Keplerian elements over a time period of one day (24 hours),

Parameter	Effect on 1-day arc Radial	Along	Cross	Total	
$D0(\beta_0)$	29	87	3	92	m
$Y0(\beta_0)$	49	350	8	354	cm
$B0(\beta_0)$	2	29	3	29	cm
$Z1(\beta_0)\sin(u-u_0)$	15	32	0	36	cm
$X1(\beta_0)\sin(u-u_0)$, $X3(\beta_0)\sin 3(u-u_0)$	2	11	0	11	cm

Table 6.4: Effect of the individual parameters of the new RPR model on the GPS satellite orbits over 24 hours.

once using the estimated model value for the parameter and once with the parameter value set to zero. The RMS of the difference between the two resulting orbits, over the full 24 hour period, was then computed to get an idea of the size of the effect. The results are given in Table 6.4.

As expected, the D0 (direct solar radiation term) and Y0 (Y-bias) give the largest contributions. However, the contributions of the B0-term and the periodic term in the Z-direction (Z1) are not negligible either. The periodic Z-term has a signature similar to the periodic terms in the B-direction, which are used by CODE to generate the IGS orbit products. The periodic terms in the X-direction have an effect of only 11 cm. The typical RMS of the 5-day fits, used for the model development, is of the order of 5 cm. The 11 centimeters are thus close to the noise level. However, the IGS orbit combinations show an orbit consistency of about 5 cm between the orbits of different ACs; an effect of 11 cm may turn out to be significant.

The CODE RPR model is based on time series of parameters computed by fitting 5-day arcs through the final products from CODE. The RMS of the residuals of the model parameter estimation, after subtracting the estimated RPR model, is used to assess the remaining errors in the model. For this purpose the RMS value was introduced as a "bias" in the corresponding RPR parameter and a 24-hour orbit integration was performed with this bias included. The differences between the biased orbit and the original orbit are a measure of the remaining orbit model errors. The results are given in Table 6.5. The total error budget was setup by introducing the RMS values for all parameters as biases of the respective parameters.

The largest error source stems from the two periodic terms in the X-direction. This is remarkable in view of the small effect these parameters have on the orbit (Table 6.4). The estimated errors from the other parameters are all below the 20 cm level. The total error budget is estimated to be about 80 cm. To verify this, our standard test was used without estimating any parameters (except the 6 osculating Keplerian elements) but introducing our RPR model. The RMS of this 7-day fit may then be compared to the estimated model error. The results are comparable and the error budget seems slightly pessimistic. This may be caused by the relatively large error of the periodic terms in X. The arc length of our standard test (7 days) is longer than the arc length used for the RPR parameter estimates (5 days). Therefore, the remaining orbit model error is estimated to be of the order of only 50 cm for a 7-day arc!

Error Source	RMS of Model Fit ($10^{-9} m/s^2$)	Effect on 1-day arc (cm) Radial	Along	Cross	Total
$D0(\beta_0)$	0.1124	4	11	0	12
$Y0(\beta_0)$	0.0462	2	16	1	16
$B0(\beta_0)$	0.1275	1	8	1	8
$Z1(\beta_0)\sin(u-u_0)$	0.1127	2	4	0	4
$X1(\beta_0)\sin(u-u_0)$	0.1653	6	41	1	42
$X3(\beta_0)\sin 3(u-u_0)$	1.3644	7	54	2	55
Total Error budget		9	77	4	78
RMS of 7-day fit					52

Table 6.5: Estimated model errors based on the RPR parameter residuals.

	D0 Y0 +ROCK	D0 Y0 +CODE	D0 Y0 B0 BC BS +ROCK	D0 Y0 B0 BC BS +CODE
Orbit Overlap (mm)	106	34	31	32
Orbit Comparison (mm)	66	54	50	51

Table 6.6: Results from real GPS data analysis using both, the ROCK and CODE RPR models, as a priori models.

Remember that for the ROCK model the orbit model error was estimated to be of the order of 300 cm for a 24 hour arc!

Finally, the new RPR model was used as a priori model in a real GPS data processing experiment with one full week of double difference carrier phase data (7 days of 3-day solutions). Four different solution types were generated. For the first two solution types our standard (D0, Y0) and extended (D0, Y0, B0, BC, BS) orbit solution types were generated using the ROCK model as a priori model. For the second two solution types the same two orbit solutions were generated but now using the new CODE RPR model as a priori model. The results are summarized in Table 6.6.

A significant improvement may be observed for the standard solution (D0, Y0). In fact, the standard solution using the CODE model has become almost as good as the two extended solutions (D0, Y0, B0, BC, BS). This is important because three orbit parameters (the three B-terms) become obsolete! The slight difference in quality is most likely caused by the eclipsing satellites, which are not treated in any special way in the CODE processing.

6.6 Comparison of Different RPR Models

The JPL analysis center also developed a new RPR model [*Bar-Sever*, 1997]. The performance of different RPR models was tested using our standard test. The CODE products (orbits and

RPR-MODEL	RMS of FIT (cm)	Prediction Median (cm)	RMS (cm)
No Model	75	133	159
T20	76	134	161
T20 Scaled	72	119	151
JPL Scaled	10	45	58
CODE	6	17	31
"BEST" (9 RPR par.)	5	17	22

Table 6.7: Orbit Fit (7 days) and orbit extrapolation (2 days) using different RPR models. Only scale (or D0) and Y-bias estimated.

ERPs) were used as pseudo-observations. Table 6.7 summarizes the results for the different RPR models available, namely ROCK, JPL, and CODE. The RMS of fit of the orbit determination, and the RMS and median of the residuals of the prediction comparison are given. In all cases two solar radiation pressure terms were estimated only; the scale term (or a constant acceleration in the direction Sun-satellite (D0)) and the Y-bias (Y0). Only for the solution labeled "BEST" more RPR parameters (all 9 parameters of the ECOM) were estimated. This latter solution is just given for reference. Furthermore, the ROCK model was used in two different ways. First, it was used as a priori model and the accelerations D0 and Y0 were estimated "on top" of the model (solution: T20), which represents the way the ROCK model is normally used in the Bernese GPS Software. Secondly, it was used by estimating a scale factor for the complete ROCK model and the acceleration in the Y-direction (solution: T20 scaled), which represents the recommended usage of the ROCK model, eqn. (6.4).

Table 6.7 shows that including the ROCK model as a priori RPR model hardly gives any improvement in both, the fit and in the prediction, compared to not including any a priori model at all. Although it was clear for a long time that the ROCK models are not very accurate, this is a surprise. Both the CODE and JPL RPR models perform much better than the ROCK model. The results of the CODE model are close to the "best possible" results. The reduction of the number of estimated RPR parameters (from 9 to 2), does obviously not significantly degrade the accuracy. This reduction of parameters should make the GPS orbit predictions more reliable. This is important because integrity of the predicted orbits is the most crucial factor for real time GPS data analysis [*Martin Mur et al.*, 1998].

7 Orbit Validation using SLR Observations

7.1 Motivation

Two of currently 27 GPS satellites are equipped with a laser reflector array: PRN 5, launched in August 1993, and PRN 6, launched in March 1994. Both satellites are tracked on a routine basis by the satellite laser ranging (SLR) ground station network of the International Laser Ranging Service (ILRS). The main motivation to use the SLR observations of the two GPS satellites has to be seen in the fact that they provide a unique and independent check of the quality of the GPS satellite ephemerides as provided by the IGS and its analysis centers.

In addition, the SLR observations may also be used to study the attitude of the GPS satellites as a function of time during their eclipse phases. Furthermore, the combination of the observations of both techniques, microwave and SLR, will unify the terrestrial reference frame of both techniques and may lead to improved orbits of the GPS satellites. The unification of the terrestrial reference frame will be of advantage for all parameters common to both techniques, i.e., Earth rotation, station coordinates, and geocenter. The SLR observations may also help to determine the actual phase center offset of the GPS satellite antenna which has a large uncertainty (as was discussed in Chapter 5).

7.2 Basics of SLR

A satellite laser ranging system is, in simple terms, an optical radar. Figure 7.1 gives a simplified picture of the SLR measurement principle. The state of the art laser (light amplification by the stimulated emission of radiation) typically operates at a repetition rate between 5 and 10 Hz. It produces ultrashort pulses with a pulse width between 30 and 200 picoseconds and a single pulse energy between 10 and 100 millijoules. The transmitted laser pulse starts a time-of-flight counter, the pulse travels through the atmosphere, is reflected by a retroreflector array on board of the satellite, returns through the atmosphere and is collected on the ground by the receiver telescope. The telescope focuses the reflected pulse onto a photo-detector (e.g., a diode) that stops the time-interval counter. The observation is therefore the time-of-flight of the laser pulse which, when multiplied by the speed of light, directly gives twice the measured range. This range measurement must be corrected for atmospheric refraction effects but, as

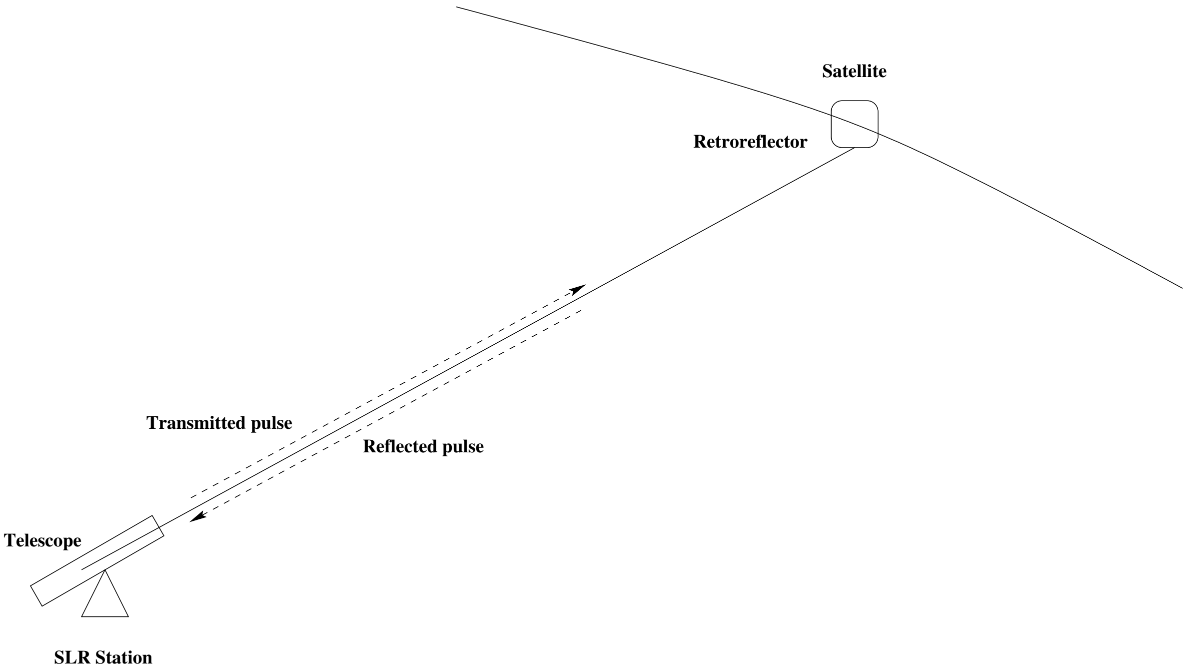

Figure 7.1: Principle of an SLR observation. By measuring the elapsed time between the start time of the transmitted pulse and the reception of the reflected pulse the range to the satellite may be determined.

opposed to to microwave measurements, the optical measurements are insensitive to both, the wet part of the troposphere and the ionosphere. The hydrostatic (dry) part of the troposphere may be modeled accurately (mm level) when local pressure, temperature, and humidity at the observing station are available [*Marini and Murray*, 1973].

The single-shot data from ranging to passive orbiting satellites typically shows an RMS scatter of 6–10 mm for state-of-the-art SLR stations. By averaging individual range measurements over a short time interval (e.g., over 2 minutes) the random errors may be reduced. The RMS scatter of these so-called normal points is at the level of a few mm only. Normal points are formed at the SLR sites after each satellite pass and are transmitted to the SLR data centers.

It should be mentioned that the activities of the SLR ground station network are now coordinated by the International Laser Ranging Service, the ILRS. The ILRS, which may be considered as the SLR equivalent of the IGS, was established in 1997. According to its terms of reference the primary objective of the ILRS is to provide a service to support, through satellite and lunar laser ranging data and related products, geodetic and geophysical research activities and to supply IERS products important for the maintenance of an accurate International Terrestrial Reference Frame (ITRF). The service also develops the necessary standards/specifications and encourages international adherence to its conventions. The ILRS collects, merges, archives and distributes Satellite Laser Ranging (SLR) and Lunar Laser Ranging (LLR) observation datasets of sufficient quality to satisfy the objectives of a wide range of scientific, engineering, and operational applications and experimentation. More information about the ILRS may be found at: http://ilrs.gsfc.nasa.gov/

7.2.1 GPS Retroreflector Array

The retroreflector arrays used on the GPS satellites were built by the Russian Institute for Space Device Engineering in Moscow [*Degnan and Pavlis*, 1994]. The GPS retroreflectors are similar in design to those used successfully on all of the GLONASS satellites. The total reflecting area of the GPS arrays is, however, much smaller due to limited mounting space on the nadir-viewing face of the GPS Block IIA satellites. The GPS retroreflector array, which consists of 32 individual retroreflectors, measures 239 mm by 194 mm, its height is 37 mm and its weight is 1.27 kg. The location of the array on the GPS satellite is indicated in Figure 6.2. The actual distances measured from the center of mass of the satellite are 0.8626, -0.5245, and 0.6584 m in the X, Y, and Z-directions, respectively, of the satellite-fixed coordinate system.

7.3 Validation of GPS-based Orbit Estimates

The SLR observations of the GPS (and GLONASS) satellites provide a unique opportunity to validate the quality of the IGS (and IGEX) orbit determination. Because the IGS orbits are based on the microwave measurements of the GPS, the SLR observations provide a completely independent validation of the orbit quality. Due to the high altitude of the GPS satellites, the angle between the vector from the SLR observatory to the GPS satellite and the vector from the geocenter to the GPS satellite is 14^o at maximum. the SLR observations are therefore nearly in the radial direction, and thus provide mainly information concerning the radial orbit errors [*Watkins et al.*, 1996].

The orbit validation is based on the difference between the observed range, the SLR normal point measurement, and the computed range. The range is computed assuming both, the SLR station positions and the GPS satellite positions, to be known. The SLR station positions may be taken from the ITRF realization, whereas the orbit positions may be obtained from the IGS, in our case the orbits of the CODE analysis center. We also have to use a set of Earth rotation parameters in this orbit validation step which are consistent with the CODE orbits, i.e., the CODE ERP estimates. The tropospheric delays are modeled using the Marini–Murray model [*Marini and Murray*, 1973] in which the temperature, pressure, and humidity measurements, delivered with the SLR normal points, are introduced.

All SLR observations of the two GPS satellites gathered since 1995 are used in our analysis. The network of all 25 SLR sites which have observed the GPS satellites during the time span from January 1995 to July 1999 is shown in Figure 7.2 where the SLR sites are identified by their crustal dynamics project numbers. Figure 7.3 shows the differences between the observed and computed ranges using all SLR observations of the GPS satellites over the

Figure 7.2: Network of SLR stations observing the GPS satellites during the 1995 to 1999 time span.

time span from January 1995 to July 1999. To remove outliers the SLR observations were edited using a 5σ outlier criterium. Less than 2% of the observations had to be removed using this criterium (which effectively removed all residuals exceeding 300 mm). Table 7.1 gives statistical information on of the residuals (which may be inspected in Figure 7.3) sorted by station and satellite.

Two interesting results emerge from Figure 7.3 and Table 7.1. First, we see an average bias of -55 mm between the observed and computed ranges. The negative sign indicates that the observed SLR ranges are shorter than the computed ranges. The occurrence of this bias is quite unexpected and asks for explanations. Secondly, the RMS of the residuals, around the mean, is as low as 55 mm. This result is truly remarkable. It implies that the two independent techniques, microwave and SLR, agree at the level of a few centimeters. Most importantly it also shows that the (radial) orbit error of the IGS orbits is as small as 55 mm. This corresponds quite well to the RMS statistics of the weekly IGS orbit combinations (see Figure 4.4). On the other hand, the 55 mm RMS is well above the noise level of the SLR normal point observations.

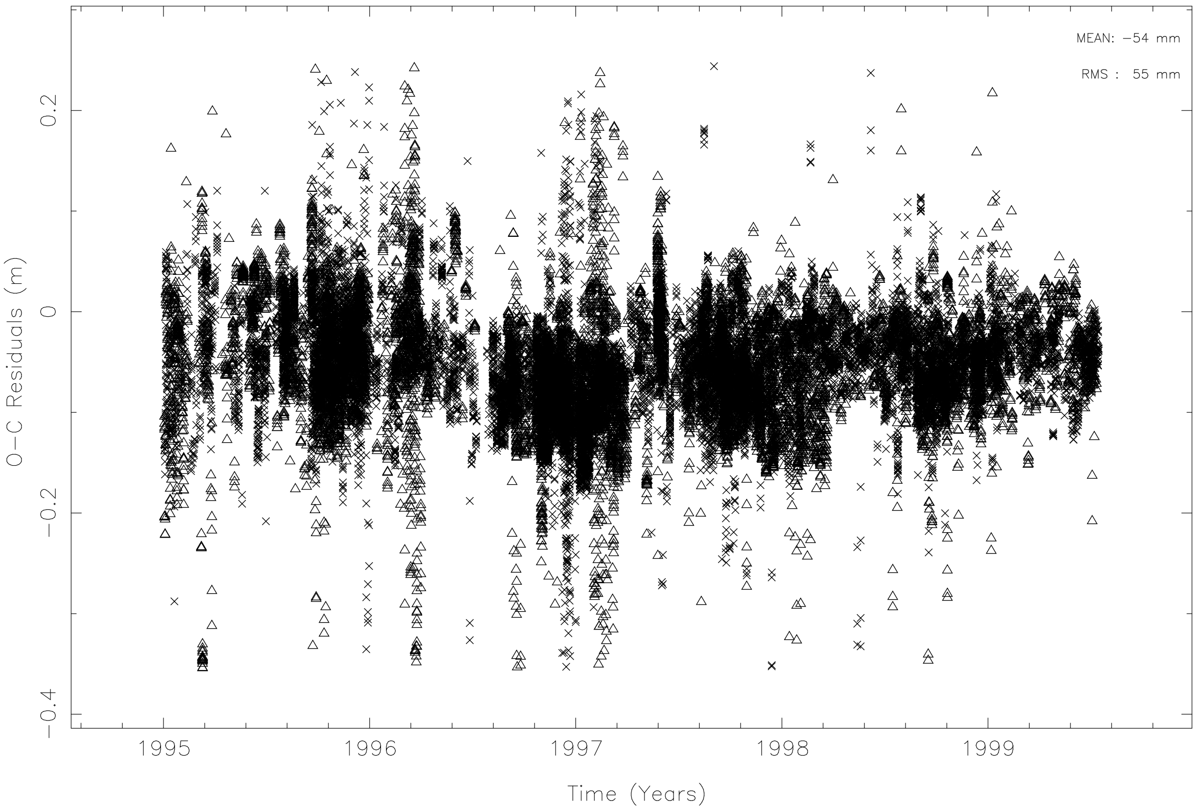

Figure 7.3: Range residuals of the SLR observations from GPS satellites PRN 5 (crosses) and PRN 6 (triangles).

Station	PRN 5 #Obs	PRN 5 Mean (mm)	PRN 5 RMS (mm)	PRN 6 #Obs	PRN 6 Mean (mm)	PRN 6 RMS (mm)
7210 MAUI	3655	-67.1	54.9	2588	-57.2	62.0
7110 MONP	2136	-65.2	40.8	1757	-76.5	59.7
8834 WETT	2226	-25.0	45.8	1389	-37.0	61.0
7090 YARR	1772	-45.5	39.8	1259	-54.7	60.8
7840 HERS	1154	-47.9	32.0	807	-67.2	41.1
7839 GRAZ	951	-49.9	24.4	986	-44.6	42.4
7843 ORRL	925	-14.8	48.2	732	-33.4	59.9
7080 MLRS	658	-91.3	55.7	614	-89.8	43.9
7884 SORNRL	414	-103.7	39.9	349	-38.2	62.1
1884 RIGA	544	-77.5	52.8	186	-42.3	66.4
7845 GRASSE	289	-36.0	28.4	374	-33.4	36.3
7835 GRASSE				28	-53.8	31.3
1864 MAID	214	26.1	79.8	158	12.0	79.1
7918 GREE	109	-79.6	59.0	157	-108.3	46.5
7105 GREE	98	-60.5	29.6	43	-102.5	68.2
7920 GREE				18	-318.2	109.1
7836 POTS	65	-73.3	20.2	5	3.2	123.7
7810 ZIMM	58	-60.0	26.5	47	-79.3	42.2
7849 MTSTROMLO	20	-109.3	85.2	50	-84.6	110.7
1893 KATZ	44	-186.4	54.4	5	-223.2	43.3
1868 KOMS	2	-2.3	173.2	29	-156.1	130.5
7832 RIYADH	29	-28.0	31.5			
7594 WETT_TIGO	10	36.7	49.0			
7109 QUIN	4	-81.0	3.1			
7811 BORO	3	-80.3	27.6			
Total	15380	-53.3	50.8	11581	-56.5	62.0

Table 7.1: Range residuals of the SLR observations from both GPS satellites sorted by station and satellite. We give the number of observations, the mean of the residuals, and the RMS of the residuals around the mean.

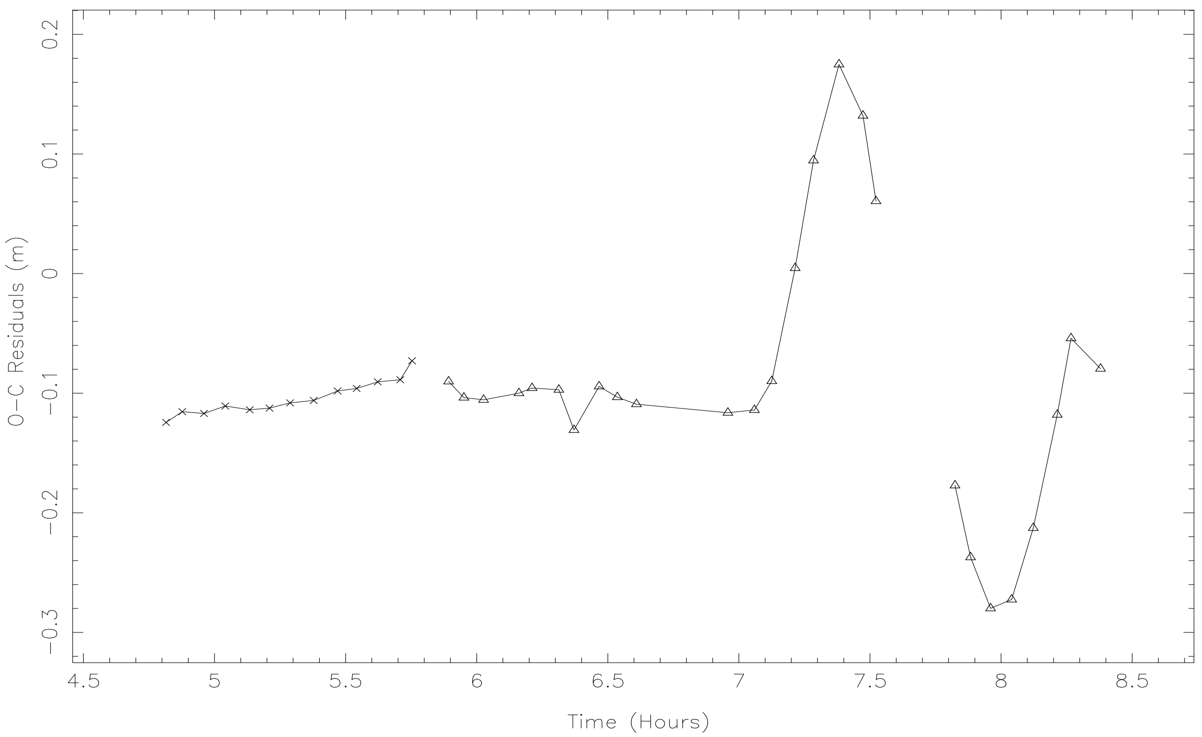

Figure 7.4: SLR range residuals for an eclipse passage of PRN 6 on day 36, 1997. The first two residual tracks are based on observations from station 7210 MAUI which observed both PRN 5 (crosses) and PRN 6 (triangles) on this day. The third residual track is based on observations from station 7110 MONP tracking PRN 6.

7.3.1 SLR Observations of Satellite Eclipses

The larger residuals in Figure 7.3, for instance around the beginning of 1997, are mainly caused by satellite eclipses. Figure 7.4 shows an example of the residuals from observations during the satellite eclipse period of PRN 6 on day 36 of 1997, 5 February 1997. On this day the eclipse period of PRN 6 lasted from 7:08 to 7:55 UTC. After eclipse exit at 7:55 UTC, the satellite takes up to 30 minutes to return to its nominal attitude. During these periods, the eclipse phase and 30 minutes afterwards, the satellite is performing an unpredictable rotation around the satellite-fixed Z-axis. Figure 7.4 demonstrates that the SLR observations may be very useful to study the rotation of the GPS satellites during their eclipse periods. They are particularly useful to validate the quality of the satellite rotation rates as estimated by some of the IGS analysis centers. The rotation effects are very clearly visible in the SLR observations because of the relatively big distance (1 meter) of the SLR reflector array w.r.t. the rotation (Z-) axis. For comparison we mention that the GPS antenna phase center is only at a distance of 0.3 m from the rotation axis.

7.4 Investigating the Microwave–SLR Bias

The observed bias between the ranges based on the microwave orbits and the observed SLR ranges might be explained by an error in the offset of the SLR reflector from the center of mass of the satellite is in error. The orbit estimates based on the microwave observations are not sensitive to errors in the offset between the center of mass of the satellite and the phase center of the satellite antenna. In Chapter 5 it was demonstrated that changing this offset by 1 meter did not have any significant effect on the orbit estimates. Therefore, the IGS orbits may be considered to accurately reflect the position of the center of mass of the GPS satellites. In the case of SLR observations from the GPS satellites any error in the distance between the center of mass of the satellite and the effective reflection center of the laser retroreflector array will show up as an apparent radial bias in the SLR residuals.

In order to verify whether the offset is the explanation for the observed radial bias we solved for this offset using the SLR observations. For this purpose the entire (clean) set of observation over the time span considered was (re-)processed day by day. From each day the normal equation system of the estimated parameters was saved. After having processed all days, the resulting set of 1256 normal equation files were stacked and the parameters of interest were estimated. On the daily level the parameters which were setup in the normal equations are station coordinates, geocenter, and satellite antenna offset. In the normal equation stacking either of these parameters may be estimated. (More information about the normal equation stacking procedures used in the Bernese GPS Software may be found in *Brockmann* [1997].)

Two series of tests were performed to study the effect of the SLR reflector array offset. For the first test series the complete data set from 1995 to 1999 was used. For the second test series only a partial set, starting in 1998, was used. For both series four solutions were computed. The first solution, in which no parameters were estimated, was generated in order to obtain the RMS of the solution. In the second solution only the radial SLR reflector offset was determined, in the third solution all SLR station coordinates were estimated, and in the fourth solution both, the radial SLR reflector offset and all SLR station coordinates, were derived. Table 7.2 summarizes the results of the two test series, where the first test series using the full data set is labeled "F" and the series based on the partial data set is labeled "P". The table gives the RMS of the residuals, and the change in the estimated radial SLR reflector offset (positive toward the Earth). The last two columns give the change in the terrestrial scale based on performing a 7-parameter Helmert transformation between the ITRF-96 coordinates of the SLR stations and the estimated coordinates, and the RMS of the Helmert transformation. Only the scale change is shown here because this was the only significant parameter of the seven estimated parameters. In the Helmert transformation only those stations with more than 200 observations and known ITRF-96 coordinates were used. This means that only the first 10 stations in Table 7.1, not counting SORNRL for which no ITRF-96 position is available, were used. A positive value for the scale means that the estimated SLR station network has a larger scale compared to the scale of the ITRF-96.

The results in Table 7.2 show that the estimation of the SLR reflector offset reduces the RMS of the solution. This was expected because the estimation of this offset is capable of

	RMS (mm)	Offset (mm)	Scale (ppb)	Helmert RMS (mm)
F1	90.8	-	-	-
F2	76.1	55.5	-	-
F3	50.7	-	10.5	34.2
F4	50.6	19.1	6.7	30.9
P1	68.8	-	-	-
P2	49.1	50.0	-	-
P3	35.3	-	11.4	37.1
P4	34.3	83.7	-5.5	25.1

Table 7.2: Selected results from the SLR station coordinates and reflector offset estimation tests.

removing the mean of the observed bias because both, the bias and the offset, are (mainly) in the radial direction. The estimation of the SLR station coordinates reduces the RMS in a much clearer way. This was expected because this estimation allows more degrees of freedom. Besides being capable of absorbing the radial bias by changing the scale of the terrestrial reference frame, it is also capable of absorbing some station-dependent biases. The estimation of the SLR reflector offset "on top" of estimating the SLR station coordinates does not further reduce the RMS. It only influences the terrestrial scale change. The results using the partial data set show that the estimation of the terrestrial scale and the SLR reflector offset are highly correlated. Unfortunately, these results do not allow us to conclude whether or not the SLR reflector offset is incorrect. The estimation of the SLR reflector offset will always absorb any radial bias. We therefore conclude that there might be a 50 mm error in the SLR reflector offset but that the evidence presented here is not very convincing. Although a terrestrial scale change of approximately 10 ppb would also explain the observed bias we do not consider this a realistic explanation. The accuracy of the ITRF scale is believed to be at the 1–2 ppb level.

It is interesting that in Table 7.2 the coordinate estimates of the SLR stations agree at the few centimeter level with the corresponding ITRF-96 coordinates. This means that the reference frame given by the ITRF-96 SLR station positions and the reference frame determined by the GPS orbit and ERP estimates, based on microwave measurements, agree at the few centimeter level.

7.4.1 A Look at the GLONASS SLR Tracking Data

The availability of both, precise GLONASS orbits stemming from the International GLONASS EXperiment (IGEX) [*Willis et al.*, 1998] and GLONASS SLR tracking allows us to study whether a similar range bias may be observed for the GLONASS satellites. For this analysis we used the CODE IGEX orbits for the time period between day 283 in 1998 (start of the

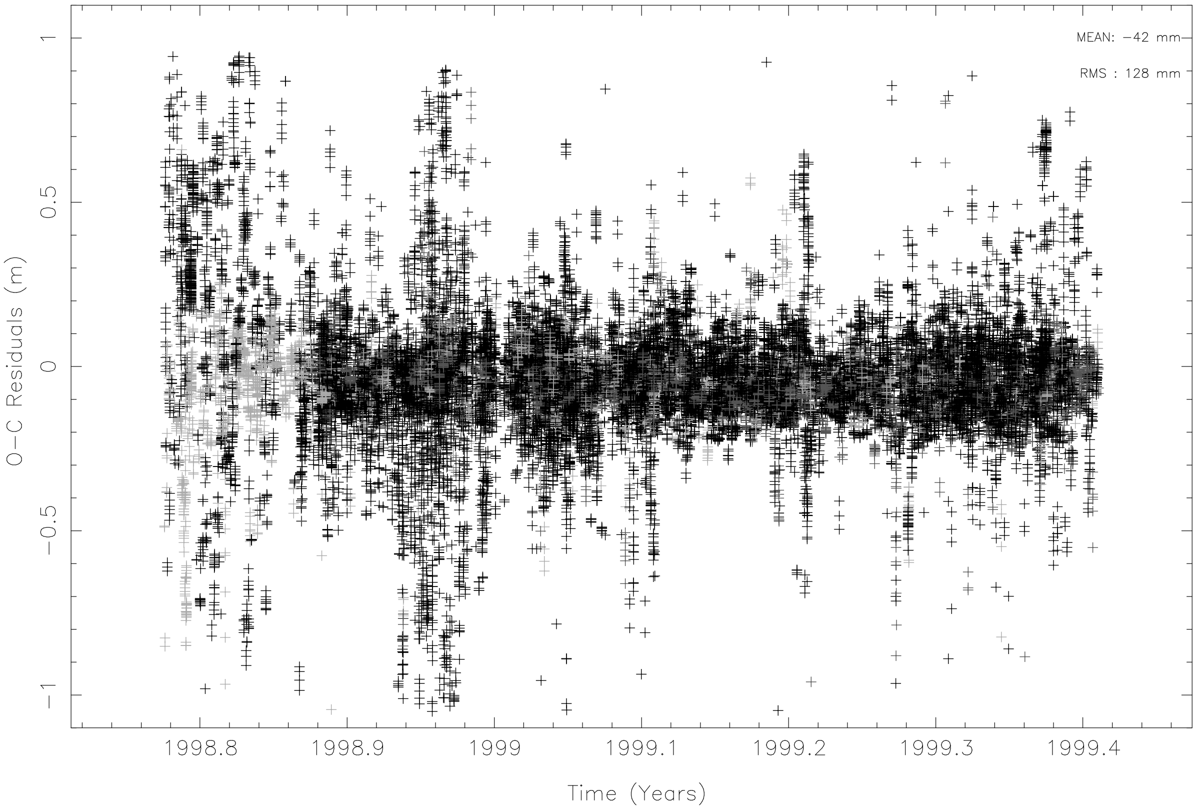

Figure 7.5: Range residuals of the SLR observations from the GLONASS satellites.

IGEX campaign) and day 149 in 1999. For a description of the CODE IGEX activities we refer to *Ineichen et al.* [1999]. Notice that there is much more SLR tracking data for the GLONASS satellites. This is due to the fact that all GLONASS satellites are equipped with SLR retroreflector arrays and that the arrays are much bigger than those on the GPS satellites. The GLONASS array is about 1.2 by 1.2 m compared to the GPS array of only 0.24 by 0.20 m. Therefore, the GLONASS satellites are much easier to track by the SLR stations and consequently more SLR stations are capable of tracking the GLONASS satellites. Figure 7.5 and Table 7.3 show the results of this GLONASS analysis.

Based on the RMS of the SLR observed minus computed residuals, shown in Figure 7.5, we conclude that the quality of the IGEX orbits is significantly worse than the quality of the IGS orbits. The RMS is 128 mm for the GLONASS SLR observations compared to 55 mm for the GPS SLR observations. This difference is mainly explained by the fact that the GLONASS microwave tracking network is relatively poor compared to the current status of the IGS network. Considering this important limitation, the GLONASS orbits are of a remarkable quality.

The bias observed in the SLR residuals turns out to be very similar for both, the GLONASS and GPS SLR observations. The bias is -42 mm for the GLONASS SLR residuals compared to -54 mm observed for the GPS SLR residuals. The fact that the offsets for both satellite

	GPS			GLONASS		
Year	#Obs	Mean (mm)	RMS (mm)	#Obs	Mean (mm)	RMS (mm)
1995	6051	-33.9	54.6			
1996	6070	-66.2	62.0			
1997	8071	-65.0	55.6			
1998	5081	-53.3	43.0	10678	-32.4	156.6
1999	1636	-38.4	35.7	24763	-45.7	113.0
Total	26909	-54.4	55.1	35450	-42.0	128.0

Table 7.3: Range residuals of the SLR observations from both, the GPS and GLONASS satellites, sorted by year.

systems are so similar practically rules out the possibility of an error in the SLR reflector offset because it is unlikely that a similar error was made in computing the center of mass correction for the retroreflector arrays on both systems. We should note, however, that the GLONASS orbits are derived by fixing the GPS orbits. Therefore, the GLONASS orbits are not independent from the GPS orbits and the same might be true for the GPS and GLONASS biases. We should point out, however, that the retroreflector arrays on both systems are very similar, the only difference being the size of the GPS and GLONASS retroreflector arrays. The observed bias might thus have something to do with the reflectors. However, given the small size of the reflectors, (height of only 37 mm) a 50 mm error is hard to imagine.

7.4.2 The Residuals

Let us study the residuals in order to further investigate the observed bias between the microwave orbits and the optical ranges. First, we look at the residual statistics per year for the almost 5 years of GPS results and the 1 year of GLONASS results. These annual residual statistics are shown in Table 7.3 which shows that the bias for the case of GPS is quite consistent over the 5 years varying from -34 to -66 mm. Table 7.3 further reveals that the bias is also constant for the 2 partial years of GLONASS data and that the bias observed for GLONASS is very similar to that observed for GPS. These results indicate that the observed bias is highly significant.

Table 7.3 reflects, to a certain extent, the improvement in the CODE final GPS orbit quality over the years. As described in Chapter 5, significant orbit modeling improvements were achieved over the time frame from 1995 to 1999. From 1995 to 1996 a small increase of the RMS of the SLR residuals is observed which is somewhat unexpected considering the improvements which were achieved in 1995 like, e.g., the introduction of stochastic orbit parameters. However, from 1996 onwards the RMS of the SLR residuals decreases steadily from 62 mm in 1996 to only 36 mm in 1999. These results are in agreement with our expectations considering the consistent improvements in our microwave processing algorithms.

The GLONASS results in Table 7.3 show that significant improvements were achieved in the orbit modeling of the GLONASS satellites over the relatively short time period of the IGEX campaign. The RMS of the SLR residuals decreases from 156 to 113 mm from 1998 to 1999.

Another way to look at the residuals is to plot them as a function of elevation. We should, however, remind ourselves of the fact that the SLR observations of the GPS satellites are mainly in the radial direction of the satellite orbit. At 20^o elevation the deviation from a perfectly radial observation is only approximately 10^o. Therefore, no real elevation dependence of the residuals due to orbit errors are expected. However, station related biases like, e.g., troposphere or coordinates, may cause clear elevation dependent effects. Figures B.1 and B.2 in Appendix B show the residuals as a function of elevation for GPS PRN 5 and PRN 6 for the first 6 stations from Table 7.1 contributing the most SLR observations over the time span considered. Although significant differences in the residual patterns between the stations exist, no significant elevation dependences may be observed. It is interesting to note the different elevation ranges of the observations which depend on the telescope mounting and the geographical location of the station. Although the residuals of some of the stations show some interesting signatures, none of the observed residual patterns may explain the observed 50 mm bias.

7.4.3 SLR-based Orbit Estimates of the GPS Satellites

To study whether the bias is caused by an error in the GPS orbit estimates based on the microwave observations we should compare the "microwave orbits" with orbit estimates based on SLR observations only. It is a problem that there is very little tracking data of the SLR stations and the geometry of the SLR network (see Figure 7.2) is very poor. This means that the "SLR only orbits" have to be computed with relatively long arcs, i.e., several days. Until quite recently this would have implied that a large number of orbit parameters has to be estimated. When using the new CODE solar radiation pressure model introduced in Chapter 6 the number of parameters may be reduced significantly. To illustrate this effect an experiment was performed in which a 7-day arc was "fitted" through the daily CODE final precise orbits using 4 different approaches. In the first three approaches only 8 parameters were solved for: state vector, direct solar radiation pressure acceleration, and a Y-bias acceleration. The difference between the three approaches lies in the a priori solar radiation pressure model; either no a priori model, the ROCK-42 model, or the new CODE RPR model was used. In the fourth approach no a priori model was used but all 9 parameters of the extended CODE orbit model [*Beutler et al.*, 1994*b*] were estimated. This last approach was chosen to have some reference for the quality achievable for this 7-day orbital arc. After estimating the orbits, using data of the first quarter of 1997, the middle days of the resulting 7-day arcs are compared to the original CODE precise orbits for the days in question. The results of this comparison, shown in Figure 7.6, give an idea about the quality with which the model was capable to represent the GPS orbits over the relatively long arc.

Figure 7.6 shows the significant improvement when using the CODE RPR model (CODE) gives compared to using no (NONE), or the ROCK-42 (ROCK) a priori RPR models. Applying the CODE RPR model the quality of the 7-day arc is comparable to the quality of the 7-day

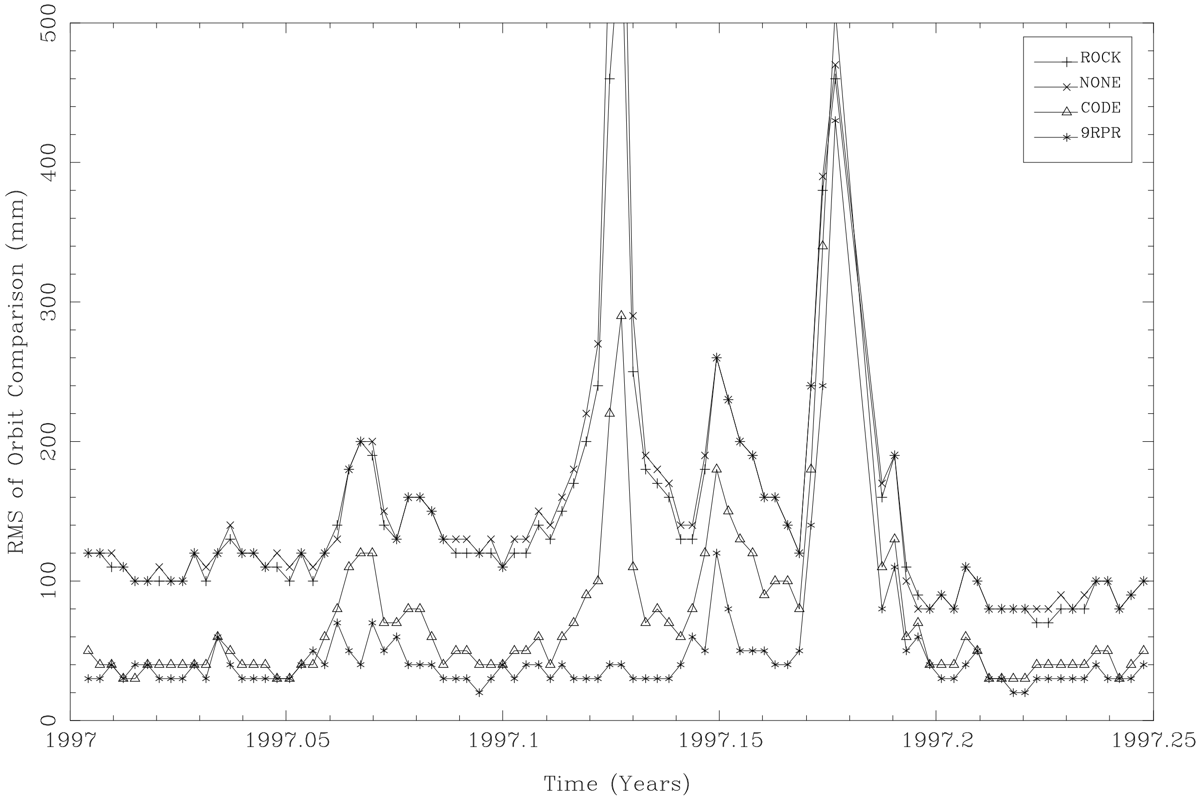

Figure 7.6: RMS of orbit comparison after fitting a 7-day arc through the daily CODE precise orbits.

arc where 9 RPR parameters had to be estimated. With the CODE RPR model only 2 RPR parameters were estimated. This difference in the number of parameters is significant when processing the SLR observations because of the sparse tracking data and the poor geometry of the SLR tracking network. These results indicate that, provided enough SLR tracking is available, it should be possible to get reasonably accurate orbits based on SLR observations of the GPS satellites only. These SLR orbits might be able to indicate whether the 50 mm bias is stemming from the microwave data analysis.

SLR-based orbits were derived for the entire year of 1997 using 7-day arcs. The two GPS satellites were modeled using the CODE RPR model and estimating the satellite state vector, the direct solar radiation pressure acceleration, and the Y-bias acceleration. The middle days of the resulting 7-day arcs were compared to the CODE precise orbits for the corresponding days. Two different orbit estimations were performed. For the first type of orbit estimation, an orbit was estimated using the seven CODE precise orbits (FIT), as was described earlier. The second type of orbit estimation was based on the SLR observations (EST). Figure 7.7 shows some of the results of this orbit comparison, for GPS weeks 922 to 930, for both types of estimates. The time frame from GPS week 922 to 930 was selected because it contains the largest amount of SLR tracking data.

Figure 7.7 shows (a) the RMS of the orbit comparison, which is performed using a seven parameter Helmert transformation, and (b) the Z-translation of this similarity transformation. It shows the results from both types of orbit estimations. The quality of the SLR-based orbits is excellent, at the level of 200 to 400 mm. This is remarkable in view of the sparse tracking (typically only a few hundred observations are available for these 7-day arcs) and the poor geometry of the SLR tracking network (typically only a few stations, mostly located in the Northern hemisphere) are providing data. This shows the potential of the SLR technique to generate reasonable results with very limited data. In Figure 7.7 we observe an interesting mean bias in the Z-translation of the SLR orbit compared to the microwave orbit. This Z-translation implies that the geocenter of the SLR-based orbits lies approximately 50 mm below the geocenter of the GPS-based orbits. The question is whether the Z-translation is the cause of the observed microwave–SLR bias or if this bias is the cause of the Z-translation. Because the majority of the SLR tracking stations lies in the Northern hemisphere the radial bias could alias into a Z-translation. Because the SLR measurements are smaller than the expected ranges this would mean that the orbits are "pulled" in the negative Z-direction. It is impossible to draw any sound conclusions at present.

For GLONASS a similar analysis as presented above would be much easier to perform due to the larger amount of SLR tracking and the better geometry of the SLR stations capable of tracking the GLONASS satellites. However, the quality of the GLONASS orbits based on the microwave observations, the IGEX orbits, is currently limited to the 150-300 mm level. Despite this limited orbital accuracy we were able to observe the 50 mm bias quite well with the GLONASS IGEX orbits. Therefore, we estimated GLONASS orbits based on SLR observations only using one week of GLONASS data, namely GPS week 992 starting on 10 January 1999. For this week the Z-translation observed for the GLONASS orbits varies between the 60 and 120 mm, whereas the RMS of the orbit comparison varies between the 200 and 300 mm.

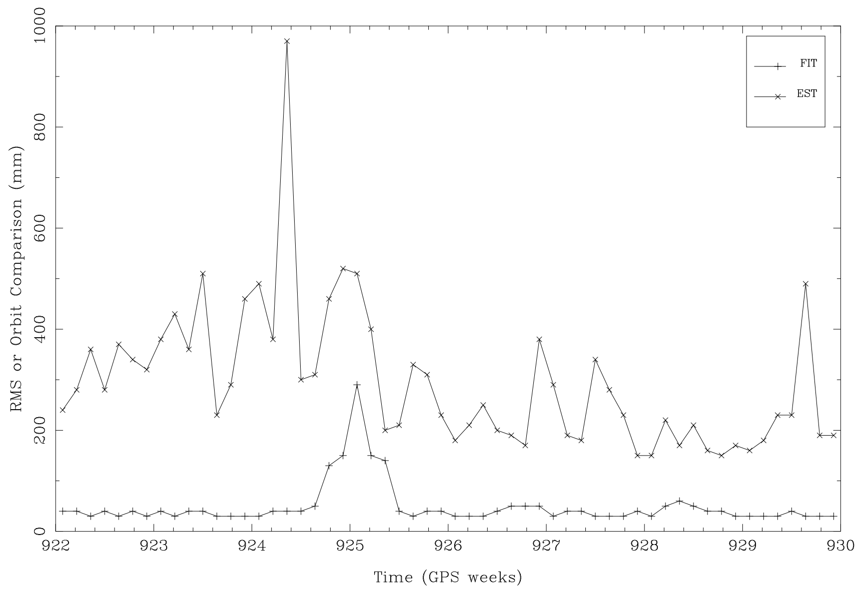

(a) RMS of orbit comparison of middle day of the 7-day arc

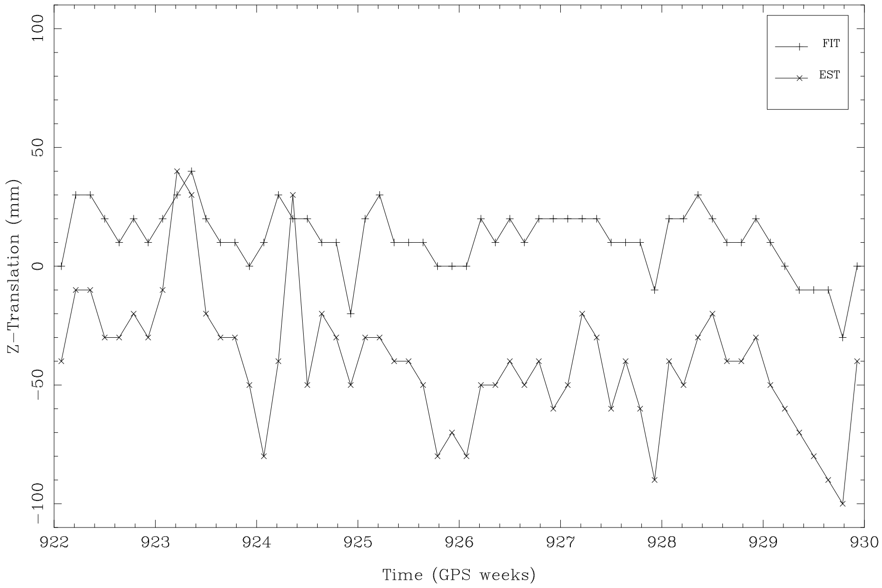

(b) Z-Translation of the middle day of the 7-day arc

Figure 7.7: RMS and Z-translation of orbit comparison after estimating a 7-day arc through the daily CODE precise orbits. The curves labeled "EST" represent orbit estimates based on SLR observations. The curves labeled "FIT" represent orbit estimates based on precise orbit ephemerides.

The results of the Z-translation agree very well with the results from the GPS system. The RMS of the orbit comparison is quite small. As a matter of fact, the RMS values are similar to the expected IGEX orbit quality.

It should be mentioned here that both, a radial bias and a Z-translation, were observed between the SLR- and DORIS-based orbit estimates compared to the GPS-based orbits for the TOPEX/POSEIDON satellite altimetry mission. For this mission the radial bias was "solved" by applying a correction to the height of the GPS antenna on board of TOPEX/POSEIDON, i.e., a radial correction. The size of this correction (personal communication with Yoaz Bar-Sever from the JPL) was +50 mm, the sign meaning that the GPS derived TOPEX/POSEIDON orbits were 50 mm higher than the orbits derived by using the SLR and DORIS measurements. The observed Z-translation was at the 20–30 mm level with the GPS-derived geocenter lying "above" the SLR/DORIS geocenter. Both these effects agree very well with the results presented here.

7.5 Summary

The combination of the observations from both techniques, microwave and SLR, would allow to unify the terrestrial reference frame of both techniques, and a successful combination should result in improved products. In the case of GPS the expected improvements would be small, however, because of the sparse SLR tracking data. As opposed to GPS, the improvements for the GLONASS system may be expected to be significant. Currently, the combination of the two techniques is impossible because of the observed radial bias of 50 mm, which deteriorates the combined products rather than improving them. Several tests in which we tried to combine the two techniques on the observation level did not lead to an improvement of results. In the case of GPS, only very small changes in the results were observed if the SLR station positions were estimated. If the SLR station positions were fixed to their ITRF coordinates in the combination, a noticeable degradation of the results was observed. In the case of GLONASS significant degradations were observed when combining the observations of the two techniques. A meaningful combination of the techniques is therefore currently impossible.

One explanation of the observed bias would be an error in GM, the product of the gravitational constant of the Earth times its mass. Double difference phase observations, the basic GPS observable, see Chapter 2, contain practically no radial orbit information. they rather observe range rates. The double difference phase observations rather observe radial orbit changes, and thus may be considered to accurately measure the orbital revolution period. The revolution period U of a satellite around the Earth may be computed from [*Beutler et al.*, 1996*a*]:

$$U = \frac{2\pi}{n} \tag{7.1}$$

where the mean motion n is computed from:

$$n^2 \cdot a^3 = GM \tag{7.2}$$

This is in fact the physical explanation of Kepler's third law. This shows that if U is observed, e.g., using GPS double difference carrier phase observations, the semi-major axis of the satellite orbit (or its radius when the eccentricity is close to zero as is the case for the GPS satellites) is given by the adopted value of GM. The currently adopted value of GM is $398600.4415 \cdot 10^9\ m^3 s^{-2}$. To explain a 50 mm radial bias in the GPS (and GLONASS) satellite orbits, GM would have to be changed to $398600.4400 \cdot 10^9\ m^3 s^{-2}$. The estimated accuracy of GM, however, is $0.0001 \cdot 10^9\ m^3 s^{-2}$ which means that the required change is 15 times larger. Such a big change of GM is unrealistic.

8 Processing Undifferenced GPS Data

In Chapter 2 we demonstrated that by forming differences one has the advantage that the number of unknown parameters is greatly reduced. The consequence is, however, that no estimates for the eliminated parameters will be available. Over recent years there has been a growing interest for GPS-based receiver and satellite clock estimates. The interest for GPS satellite clock estimates is mainly driven by the fact that it allows for precise point positioning, using data from one single station together with the IGS orbit and satellite clock estimates. The interest for the receiver clock estimates is driven by the fact that it allows for highly precise frequency and time transfer between different (atomic) clocks. In fact, GPS is already a widely accepted technique for time transfer using the so-called "common-view" method. This C/A-code based method does, however, not exploit the full potential of the GPS.

In order to be able to estimate the satellite and receiver clocks we have to abandon double difference observations. Because there is interest in both, the receiver and satellite clock estimates, we will use the undifferenced data processing approach. If only receiver or satellite clocks are of interest a single difference approach is more appropriate, and more efficient, as well.

8.1 Cleaning Undifferenced GPS Data

The main problem when processing undifferenced GPS data is to reliably and automatically detect outliers and cycle slips in the observations. The data cleaning of differenced GPS data is much easier because many common error sources may be removed by forming the differences, in particular station and satellite clocks. However, several programs have been developed which seem to be reasonably successful in cleaning undifferenced GPS data. For the development of our automatic editing algorithm for undifferenced GPS data we have taken a similar approach as that used for the TurboEdit program [*Blewitt*, 1990].

Our algorithm, like the TurboEdit program, requires the use of dual frequency code and phase observations. The major problem with this approach resides in the fact that it depends heavily on the quality of the code observations. For TurboEdit the noise of the code observations is assumed to be below 0.5 wide-lane cycles, i.e., 43 cm. This requirement is easily fulfilled if anti-spoofing (AS) is not active. For most state-of-the-art geodetic receivers the noise of the code observations under those conditions is at the 20 cm level. However, with AS active, the noise is significantly larger because only C/A-code is available on the L_1 frequency and the code on the L_2 frequency is reconstructed using either so-called cross-correlation or W-code tracking techniques [*Ashjaee and Lorenz*, 1992].

The input to our program RNXSMT, which stands for RINEX SMooThing, is a single RINEX file. The output is a RINEX file again, hopefully free from outliers and cycle slips. A summary of the actions taken by the program are contained in the log-file. Each RINEX file is processed satellite by satellite. The observations of each satellite are processed in four steps:

1. Screening of the Melbourne-Wübbena linear combination, eqn. (2.21), for outliers and cycle slips.

2. In case cycle slips are detected in the first step the geometry-free linear combination, eqn. (2.17), is checked in order to determine the size of the cycle slip on both frequencies. This information can be used to connect the observation before and after the cycle slip. Currently only data pieces (arcs) the smoothed code observations may be "connected". The phase observations are never connected over a cycle slip.

3. Screening of the difference between the code and phase ionosphere-free linear combinations, eqns. (2.12 and 2.13); i.e., $L_3 - P_3$. This screening is performed to remove bad observations which were accepted in the Melbourne-Wübbena screening.

4. Smooth the code observations using the code and carrier phase data of the clean observation arcs.

Below, each of these steps is discussed in detail.

8.1.1 Melbourne-Wübbena Data Screening

The Melbourne-Wübbena combination eliminates the effects of the ionosphere, geometry, clocks and the troposphere (see eqn. (2.21)). Apart from the wide-lane ambiguity the remaining signal should be pure noise, with an RMS error of approximately 0.7 times the RMS of the code observations on the L_1 frequency. If the noise of the Melbourne-Wübbena combination has an RMS error below 0.5 wide-lane cycles (43 cm) it is almost trivial to detect all cycle slips and outliers. Only very few epochs are needed to estimate the wide-lane ambiguity, jumps and outliers can easily be detected. Of course, only the difference between the cycle slips on the two frequencies is detected ($n_5 = n_1 - n_2$), see eqn. (2.20). Note that in the very unlikely case where the integer number of cycle slips on the two frequencies are identical (i.e., $n_1 = n_2$) no cycle slip will be detected ($n_5 = 0$).

However, under AS the noise of the Melbourne-Wübbena combination for most geodetic receivers exceeds the RMS of 0.5 wide-lane cycles. Figure 8.1 shows the effect of AS on the Melbourne-Wübbena combination. It shows a single pass of a single satellite (PRN 18) for the same station on two different days. On the first day, day 40, 1998, AS was not activated. On the second day, day 60, 1998, AS was active. The different noise level on the two days is quite obvious. The beginning and the end of the observation arc illustrate that for low elevations

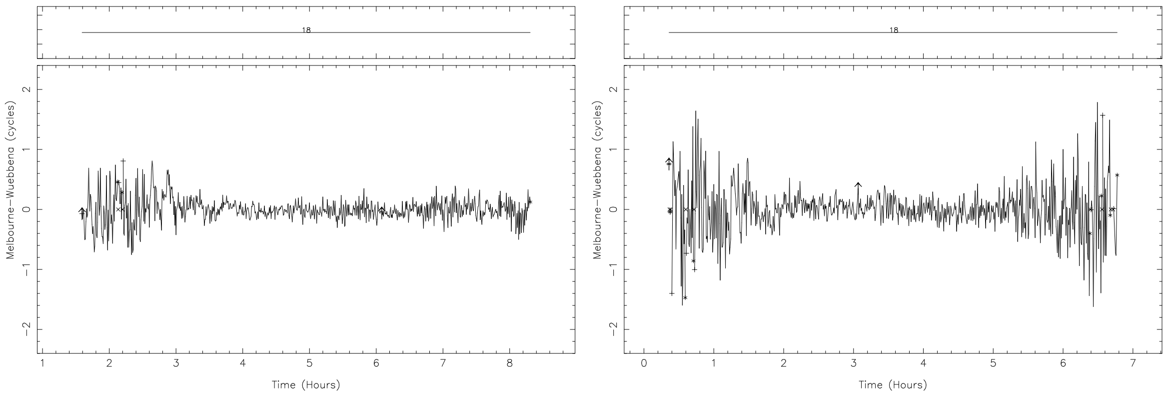

(a) AS turned off (day 40)

(b) AS turned on (day 60)

Figure 8.1: Noise of the Melbourne-Wübbena combination under different AS conditions. The data from the same station (Wettzell, Germany) are show for two days in 1997.

a much more pronounced increase of the noise level is observed for “AS on” as compared to “AS off”. For low elevations it will thus be more difficult to detect small outliers and cycle slips. It will be impossible to detect outliers of one or two wide-lane cycles (86–172 cm). It is also interesting to note the shift in time of the observation arc of this satellite. On day 40 the satellite was first tracked at approximately 1:30 hours, whereas on day 60 the first data of the satellite were observed at approximately 0:10 hours. This is caused by the 4 minute shift per day of the satellite–station geometry.

The only way to improve the reliability of screening data from one station is to generate as long arcs as possible. So, instead of using a running average, as it is done in the TurboEdit algorithm, we make the attempt to use all observations within one satellite pass. An arc is defined by specifying a minimum number of observations and a maximum time for data gaps. Typical values are a minimum of 10 data points per arc and a maximum of 3 minutes without observations before starting a new arc.

After defining the arcs, the RMS error of the observations in the arc is computed. If the RMS exceeds a user-specified maximum the observation arc is screened for cycle slips. In the cycle slip detection the observation arc is split-up into two equally long parts. It is assumed that the part with the larger RMS contains the cycle slip(s). Both parts are edited for outliers, using as outlier level four times the RMS (4σ) of the observations in the arc with a maximum RMS value specified by the user. In this step outliers are only temporarily removed. The difference between the two (clean) parts is estimated and the whole arc is connected using the estimated cycle slip. All points that were considered outliers during the cycle-slip detection are included again. The RMS is recomputed to check whether there are more cycle slips in this observation arc.

After the detection of all cycle slips, the observations are screened for outliers. Outliers are removed until the RMS of the observation arc is below the specified maximum. Outliers are those points which exceed a value of 4σ. The specified maximum RMS is typically 0.4–0.6 wide-lane cycles (34–52 cm). If an outlier is detected, all four observation types (code and phase on two frequencies) are rejected.

8.1.2 Geometry-Free Data Screening

Only those observation arcs in which cycle slips have been detected are screened using the geometry-free combination of the phase observations (see eqn. (2.17)). At this stage the size of the wide-lane cycle slip ($n_1 - n_2$) is known. The geometry-free linear combination (L_4) allows us to compute the size of the n_1 and n_2 cycle slips because it gives us: $L_4 = L_1 - L_2$. To determine the size of the cycle slip on the L_4 linear combination two linear polynomials are fitted through n points, "n" defined by the user, before and after the cycle slip. The difference between the two polynomials at the time of the cycle slip is computed. If the fractional part of the difference is smaller than a user specified limit the n_4 cycle slip is accepted and the n_1 and n_2 cycle slips are computed. Typically a value of n=10 is used and a difference smaller than 10 mm. This procedure is only executed to be able to connect the code observations during the code smoothing step. Because cycle slips occur rarely, no attempt is made to connect the phase observations. For the phase observations a new ambiguity is setup at the epoch of the detected cycle slip.

8.1.3 Ionosphere-Free Data Screening

When developing the program it became evident that sometimes the data was not cleaned successfully due to systematic errors in the Melbourne-Wübbena combination. These systematic errors are most likely caused by the filtering and smoothing procedures employed in the receivers. Therefore, an additional data screening step was added to the program.

In this step we build the difference between ionosphere-free linear combinations for the phase and code observations, eqns. (2.12 and 2.13), i.e., $L_3 - P_3$. As in the case of the Melbourne-Wübbena combination this linear combination should consist of noise only. The disadvantage is the amplified noise (about 3 times the noise of the P_1 observations). The noise is thus about 4 times larger than the noise of the Melbourne-Wübbena combination. Nevertheless, the check is useful for removing errors caused by systematic effects. The check consists of an outlier rejection scheme, which is very similar to the one used for screening the Melbourne-Wübbena combination. The starting value for the maximum RMS is larger (typically 1.6–1.8 meters), to account for the higher noise of these observations.

8.1.4 Code Smoothing

The final step consists of the smoothing of the code observations. The previous program steps have hopefully cleaned both, code and phase observations. This enables us now to smooth the code observations, using the carrier phase observations, for the continuous data arcs. For code smoothing it was decided to actually replace the code observations in a clean observation arc by the phase observations shifted by the mean difference code-phase in the arc. We have to account for the opposite sign of the ionospheric effect for the code and phase observations. The smoothed code at epoch t is written as:

$$
\begin{aligned}
\tilde{P}_1(t) &= \phi_1(t) + \bar{P}_1 - \bar{\phi}_1 + 2 \cdot \frac{f_2^2}{f_1^2 - f_2^2} \cdot ((\phi_1(t) - \phi_2(t)) - (\bar{\phi}_1 - \bar{\phi}_2)) \qquad (8.1)\\
\tilde{P}_2(t) &= \phi_2(t) + \bar{P}_2 - \bar{\phi}_2 + 2 \cdot \frac{f_1^2}{f_1^2 - f_2^2} \cdot ((\phi_1(t) - \phi_2(t)) - (\bar{\phi}_1 - \bar{\phi}_2))
\end{aligned}
$$

where:

$\tilde{P}_F(t)$	...	Smoothed code measurement at epoch t and frequency F.
$\phi_F(t)$	...	Carrier phase measurement at epoch t and frequency F.
$\bar{P}_F - \bar{\phi}_F$	...	Mean difference between over all the accepted code and phase measurements in the current observation arc on frequency F.
$\phi_1(t) - \phi_2(t)$	...	Ionospheric delay at the current epoch.
$\bar{\phi}_1 - \bar{\phi}_2$	...	Mean ionospheric delay over all the accepted phase measurements in the current observation arc.

Figure 8.2 shows the effect of code smoothing. Shown are the residuals of a point positioning procedure, estimating only the receiver clock offset for each observation epoch and using the CODE final orbit and satellite clock estimates. The RMS error of the residuals in Figure 8.2 are 1.53 and 0.17 meters for the code residuals and the smoothed code residuals, respectively. The code smoothing has been quite successful. The smoothed code residuals show systematic errors of up to one meter. The size of these biases is a function of the noise of the code observations and the number of observations used in the smoothing interval. One may consider smoothed code observations as ambiguity-fixed phase observations where the ambiguities were fixed only approximately.

8.1.5 Reliability and Possible Enhancements

RNXSMT has been used routinely since January 1997 for the estimation of receiver and satellite clock offsets using a network of 80 stations. In addition, the program was also used for all the time transfer experiments with our two time transfer terminals. The time transfer observations are also processed on a routine bases, with a few interrupts, since January 1997. In both applications the program proved to be very reliable and successful.

There is still room for improvement, however. One possible improvement would be to use the geometry-free combination of the phase observations for data screening and not only to correct cycle slips. Currently, data screening is based on code observations; both, the Melbourne-Wübbena and the ionosphere-free data screening, use code observations. Therefore, the data cleaning is heavily depending on the quality of the code observations. Without AS turned on this is not too much of a problem, but with AS turned on the quality of the code

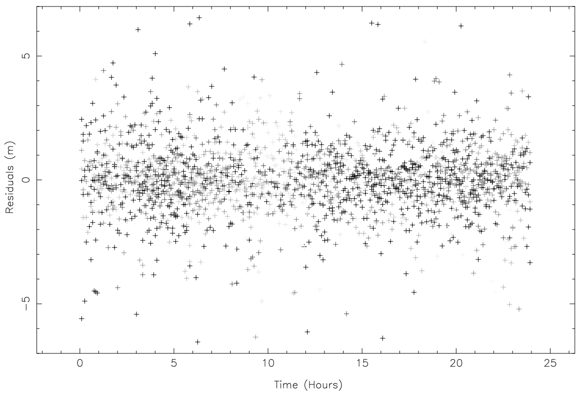

(a) Normal code residuals

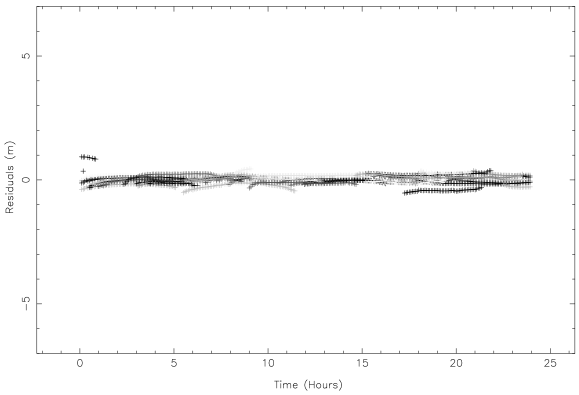

(b) Smoothed code residuals

Figure 8.2: Code residuals from point positioning. Data from a receiver installed at USNO were used for day 133 of 1999.

deteriorates significantly in particular for low elevation data. It is therefore possible that a significant amount of low elevation observations is removed from the data in the outlier rejection process. The use of phase observations in the cleaning process may help to reduce the number of rejected phase observations.

Furthermore, the use of code observations also implies that small outliers in the phase cannot be detected safely. With a typical RMS of 0.4 cycles for the Melbourne-Wübbena combination the 4σ outlier detection level is about 140 cm. All (carrier phase) outliers below this level will not be detected. They will have to be detected by screening the observation residuals after a parameter estimation step.

Another improvement would consist of weighting the observations with $\cos^2 z$, z being the elevation angle. The clear elevation angle dependence of the data quality, in particular of code observations, could then be taken into account. Such a procedure requires additional information like, e.g., receiver and satellite positions. The current procedure requires no external input, except for the RINEX file. An other possibility to weight the observations is by using the signal to noise ratio of the observations. This information is available in the RINEX files and therefore does not require any external input.

8.2 Time Transfer using the GeTT Terminals

8.2.1 Motivation

Until quite recently GPS time transfer was mainly realized using the so-called common-view (CV) technique. In this method the time of arrival of the same C/A-code signal from one satellite is registered at two stations with respect to their local reference clock [*Ashby and*

Weiss, 1980]. The main limitation of this method is the use of only the C/A-code signal of the GPS satellites transmitted on L_1. The achievable accuracy, on short baselines, is limited by the noise of the C/A-code signal, which is at the meter level or, in units of time about 3 ns. Errors in the satellite positions (usually only broadcast ephemerides are used) and ionospheric delays (only one frequency is used) will further decrease the accuracy depending on the distance between the two stations. The typical accuracy of the CV time transfer is about 5 ns.

The achievements of the IGS (Chapter 5) let us believe that this modest accuracy may be improved significantly! The combined IGS satellite clock estimates have a precision of about 0.3 ns. The same kind of precision is expected for the receiver clock estimates. These considerations indicate that the use of code and phase dual-frequency observations stemming from state of the art geodetic GPS receivers may improve the GPS time transfer accuracy by an order of magnitude. The main advantages of the "geodetic time transfer" compared to the CV method lie in the use of all satellites in view, of code and phase observations on both frequencies, and of precise orbits. Furthermore, the accuracy is not (very much) depending on the baseline length and the technique is not limited in the number of stations! In addition, the relatively high sampling rate (e.g., 30 sec.) of the IGS network also allows for frequency transfer with a very high precision. The baseline length dependence of the results is mainly caused by the quality of the GPS satellite orbits. As we have demonstrated in Chapter 4, the quality of the orbits of the IGS analysis Centers is now at the 30–50 mm level. This means that the results will deteriorate very slowly with increasing baseline length.

Two Way Satellite Time and Frequency Transfer (TWSTFT) is another method allowing time transfer. TWSTFT performs better than the CV method but at the price of complex sending and receiving equipment. TWSTFT is typically performed only once every two to three days because of its high cost [*Kirchner*, 1991; *Hackman et al.*, 1995].

In 1991 a common project of the Swiss Federal Office of Metrology (OFMET) and the Astronomical Institute of the University of Berne (AIUB) was started in order to develop time transfer terminals based on geodetic GPS receivers. The goal is to perform time transfer with sub-nanosecond accuracy and frequency transfer on the level of 10^{-15} over one day. Optimum use should be made of the GPS code and phase measurements using only geodetic-type GPS equipment [*Schildknecht et al.*, 1990]. The emphasis in this project is put on the comparison of external (as opposed to receiver internal) clocks. Calibration of delays in cables, temperature dependent delays, etc., are of major interest in the context of this joint OFMET/AIUB project. We emphasize that the control of these delays is crucial and absolutely mandatory for time transfer. The requirements are much less stringent for frequency transfer.

Two prototype geodetic time transfer terminals (GeTT terminals) were built and are available today. An additional terminal is under construction. The terminals are based on modified Ashtech Z-12 receivers. These receivers have a 20 MHz and a 1 PPS input allowing to completely replace the internal clock by an external (laboratory) clock [*Overney et al.*, 1997]. These modified receivers were marketed as Ashtech Z12-T and an upgraded version is available under the name Ashtech Z12-Metronome. More information about the time transfer project and the GeTT terminals may be found in [*Schildknecht and Springer*, 1998; *Overney et al.*, 1998; *Dudle et al.*, 1998, 1999].

8.2.2 Clock Estimation

In principle, clock estimates may be extracted directly from processing a global network including orbit estimation in solutions similar to our routine IGS process. Clock estimates may also be derived from a dedicated campaign using only a subset of the global network. Because our global IGS solutions are based on double differences this second approach is more efficient in our case. We make optimal use of the results from our global IGS solutions by introducing our orbit, station position, and tropospheric zenith delay estimates as known for the time transfer processing.

GPS is a differential technique. This implies that we cannot solve for the offsets of all clocks in the network. We either have to fix (assume as known) one single reference clock (either a receiver or a satellite clock) or we have to fix the mean of an ensemble of clocks. For other than clock parameters the specific choice of the reference clock is of no importance as long as this reference clock is synchronized to GPS time below the millisecond level. Because all geodetic receivers are synchronized to GPS time at the millisecond level this condition is always met. For time transfer it is preferable to use a stable oscillator as a reference clock, or an ensemble of stable oscillators, because the behavior of the reference clock will be visible in all other clock estimates. We also need information about the positions of the receivers and the satellites. For longer baselines we have to account for the effects caused by tropospheric refraction.

The receiver positions may be obtained from different sources, e.g., from the ITRF or the IGS if the station is part of the IGS network. If the position of the receiver is not available its position must also be estimated in addition to the receiver clock. Day to day changes in the position estimates may influence the clock estimates. This effect is probably not significant in view of the typical day to day repeatabilities of the station position estimates of better than 10 mm (33 ps). Nevertheless, it is more meaningful to estimate the position of the station prior to performing the time transfer. Therefore, the station positions may be assumed known for time transfer purposes.

The satellite positions may be derived either from the broadcast ephemerides or from the IGS precise orbits. Due to the substantial quality difference the broadcast orbits are only suited for short baselines, i.e., baselines of the order of a few km. For longer baselines the IGS orbits should be used to obtain high accuracy.

When processing long baselines we have to solve for parameters to account for tropospheric refraction. We may, however, also use the tropospheric zenith delay estimates from our routine IGS solutions for those stations which are used in both, our global and our time transfer network solutions. Apart from reducing the number of unknown parameters this procedure improves the results as we have demonstrated for our European solutions in Chapter 5.

For time transfer we solve for the receiver and satellite clocks (except one reference clock) and the tropospheric zenith delay parameters (typically 4–12 per day) for those stations which were not included in our global IGS processing. Tropospheric zenith delays are only estimated for baselines longer than a few kilometers. If phase observations are used, a (large) number of ambiguity parameters has to be estimated (about 60 ambiguities per receiver per 24 hours of observations). In order to achieve highest quality the phase observations should be used. If the absolute value of the clock estimates is of importance, i.e., for time transfer, the (smoothed) code observations should also be used but with a much lower weight than that of the phase observations.

8.2.3 Zero and Short Baseline Tests

Initially the two GeTT terminals were operated on short (or even "zero") baselines. We speak of a zero baseline if the two receivers are connected to the same antenna. The usage of zero or short baselines has as advantage that many common error sources are significantly reduced like, e.g., orbit, ionosphere, troposphere errors. A zero baseline eliminates these errors completely and, in addition, it eliminates multipath effects. Furthermore, both receivers may be run on the same clock which means that the clock difference between the two receivers is zero apart from the receiver delays. The resulting clock differences have to be attributed to delays in antennas, cables, and receivers.

For calibration purposes the zero and short baseline tests provide an excellent environment. Therefore, the first tests with the GeTT terminals were performed using short baseline setups either at the observatory in Zimmerwald or in Wabern, the location of the OFMET near Berne. Using the observations of these short baselines we were able to develop and test the GeTT terminals and study the delays coming from the antennas, cables, and the receivers. In addition, we were able to study the temperature dependence of these delays [*Overney et al.*, 1997].

The short baseline tests also allowed us to develop the capability to process undifferenced data with the Bernese GPS Software package. The first step was made in September 1995 enabling zero-difference processing using code observations. In January 1997, with the RNXSMT program, the capability to process undifferenced phase observations was added to the Bernese GPS Software package.

Three observation types may be used today for time transfer, code, smoothed code, and phase observations. The quality of the clock estimates based on these observation types is illustrated in Figure 8.3. The clock estimates from a short (180 m) baseline are shown using data from two receivers at USNO for day 318 of 1998. One receiver is a GeTT terminal, the other the official IGS receiver at USNO. These two receivers were running on two different hydrogen masers. The estimates, shown in Figure 8.3, are based on code observations (P3), smoothed code observations (S3), and carrier phase observations (L3), respectively. In all cases the ionosphere-free linear combination was used. When processing the carrier phase observations the smoothed code observations are also used. Because the phase observations do not contain any absolute information the clock estimates will have an arbitrary (but constant) offset. This is why the code observations must be included in the processing (with a low weight). In this way the absolute value of the clock estimates is based on all code observations over the full observation interval. The variation of the clock estimates over the observation interval is, however, based on the phase observations. The length of the observation interval is limited by complete losses of lock to all satellites. Because usually there are no tracking inter-

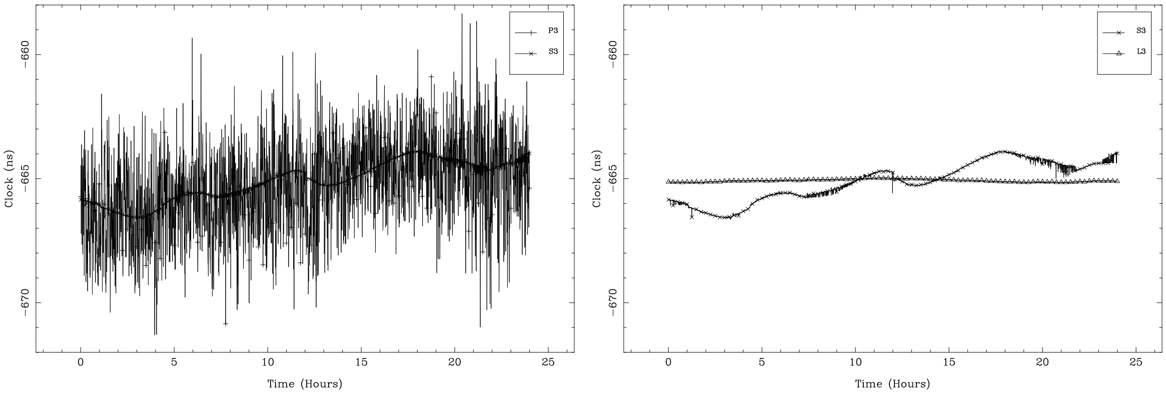

(a) Using code (P3) and smoothed code (S3) observations

(b) Using smoothed code (S3) and phase (L3) observations

Figure 8.3: Clock estimates on a short baseline based on different observation types.

rupts the observation interval is limited to 24 hours due to the current practice of processing GPS observations in 24-hour "batches". This leads to small jumps in the clock estimates at day boundaries.

The RMS of the clock estimates in Figure 8.3 is 1.82, 0.77, and 0.05 ns for the P3, S3, and L3 observations, respectively. These results demonstrate that the phase observations give the best results. It is interesting to see that the smoothed code solution tracks the code solution very well and that its behavior is indeed "smoothed". The variations observed in the code and, in particularly, smoothed code estimates are most likely caused by multipath effects which are much more pronounced for code observations than for phase observations. Another explanation for the observed variations may be the temperature dependence of the GeTT terminal (antenna, cables, receiver) delays. These effects are more pronounced for the code observations [*Overney et al.*, 1997].

Figure 8.4(a) magnifies the time interval between 10^h and 11^h UT of Figure 8.3. In addition, the so-called Allan deviations [*Allan and Weiss*, 1980] are shown in Figure 8.4(b) for the three observation types (P3, S3, L3) in Figure 8.3. It is interesting to point out that the performance of the CV time transfer method is, at best, comparable to that of the code estimates (P3) in Figure 8.3 and Figure 8.4. We say "at best" because we used all satellites in view simultaneously whereas the CV method (in most cases) uses only one single satellite. On average we have six satellites in view which means that the RMS of our estimates is roughly a factor of $\sqrt{6}$ lower compared to the RMS of the CV estimates. Our approach provides estimates every 30 seconds for the full 24 hours per day whereas CV gives estimates only within limited time intervals. Figure 8.4(b) nicely shows the different quality of the three observation types. The first point of the Allan deviations, at $\tau = 30$ sec, shows the noise of the clock estimates which should be comparable to the noise of the observations. The noise may be computed by

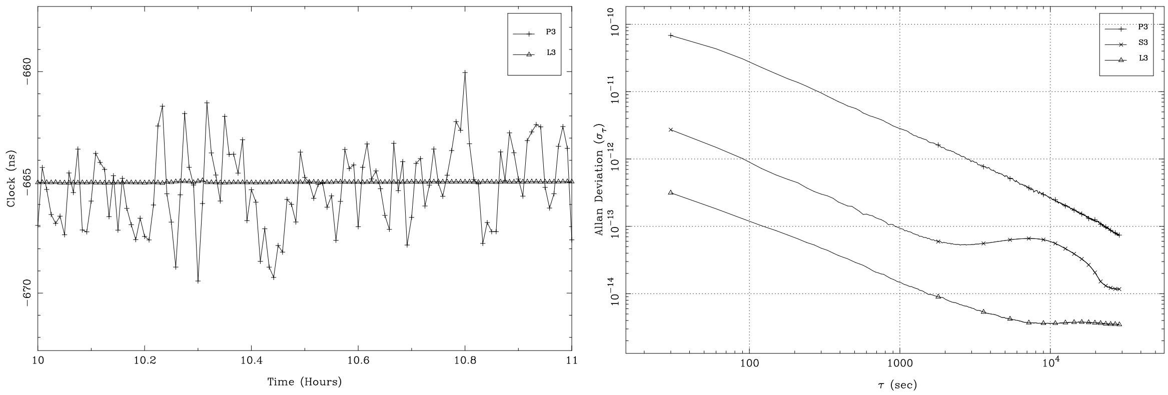

(a) Estimates based on code (P3) and phase (L3) (b) Allan deviation of the three observation types

Figure 8.4: Clock estimates using different observation types and their respective Allan deviation.

multiplying the value of τ with the value of the Allan deviation, e.g., for the code observation we find an Allan deviation of $7 \cdot 10^{-11}$ at 30 sec. This gives $30 \cdot 7 \cdot 10^{-11}\ s = 2.1$ ns for the noise of the clock estimates which corresponds to 630 mm. This reflects the noise of the code observations under AS conditions and also agrees with the observed RMS of the clock estimates over the full day (1.8 ns). Similarly we find a noise level of 27 and 2.7 mm (90 and 9 ps) for smoothed code and phase observations, respectively. Notice that for the smoothed code and the phase observations the Allan deviation at 30 seconds gives a much lower noise estimate than was determined for the clock estimates over the full day, i.e., 770 and 50 ns compared to 90 and 9 ns. This is caused by the fact that systematic effects, which are clearly visible in the S3 estimates, influence the RMS but not the Allan deviation at $\tau = 30$ sec. This is an important characteristic of the Allan deviation.

If the residuals of the clock estimates would be "white phase noise", the Allan deviation given in double logarithmic scale, as in Figure 8.4, should show a slope of -1 (for $\tau < 1000$ sec). This slope decreases to -0.5 if the estimates are "white flicker noise". The Allan deviations of GPS based clock estimates are expected to show white phase noise (i.e., show a slope of -1), if they are connected to a stable oscillator. In Figure 8.4 we observe that the slopes of the three curves are indeed close to -1 for low values of τ. For larger values of τ the effect of multipath, in the S3-curve, and also the characteristics of the two masers, in the L3-curve, show up around $\tau = 3000$ sec. Notice that Allan deviations may only be (reliably) computed for a time interval of approximately $1/3$ of the actual observation interval, i.e., for a full day of observations (86400 sec) the maximum τ for which the Allan deviation may reliable be computed is approximately 30000 sec.

Although much more pronounced in the code observations the phase observations also suffer from multipath. This may be observed in the clock estimates shown in Figure 8.5 where

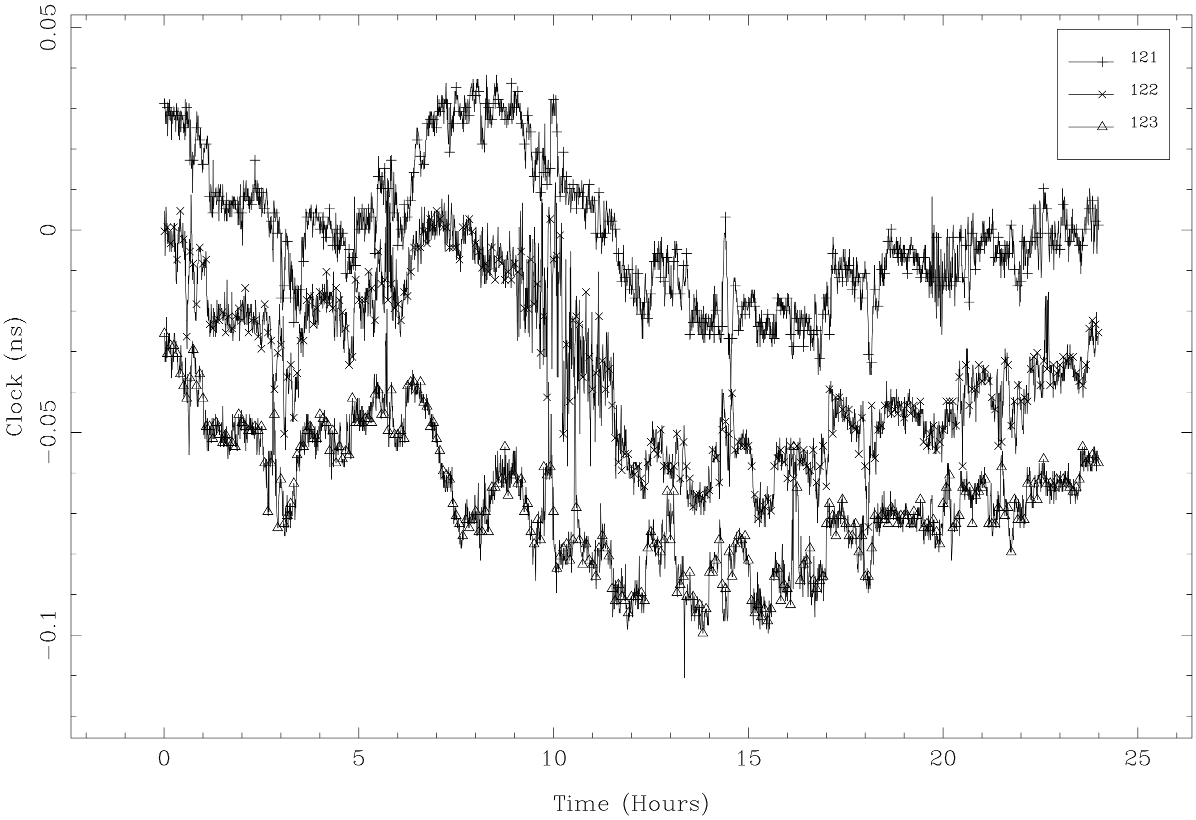

Figure 8.5: Clock estimates on three consecutive days. A mean value was removed from the daily estimates and the three curves are offset by approximately 30 ps.

the observations from our two GeTT terminals deployed on a short baseline in Wabern are used. Both receivers were driven by the same external clock. The results stem from processing the phase (L3) observations, including the (smoothed) code observations. Figure 8.5 shows the clock estimates for three consecutive days, days 121–123 of 1998. A mean has been removed from the estimates, and the days have been offset for display purposes. The mean for all three days was approximately 25 ns. Because both receivers were running on the same external clock, this 25 ns may be attributed to the delays in the GeTT systems (antenna, cables, and receiver).

Except for an offset (caused by different delays) and the measurement noise, the three clock estimates should lie on horizontal lines because both receivers are running on the same clock. This is not the case! Deviations of up to 20 ps RMS are observed. The similarity of the clock variations on the three days is striking. Both, the general behavior and some of the short term variations, are similar. Whereas the general behavior may also be caused by the temperature dependence of some of the delays, especially from the cables, the similarity in details cannot be explained by delay changes. The only plausible explanation for these variations is multipath of phase measurements. A Fourier analysis of the clock estimates on this short baseline indicates that these (multipath) effects give rise to clock estimate variations on the level of 10–20 ps with periods around 8, 12, and 24 hours. The 24 hour period might perhaps be caused by small jumps at the day boundaries. The multipath effect on the code observations is much larger as we have seen in Figure 8.3. This code multipath may result in small jumps at the observation interval boundaries, usually the day boundaries, which in turn may show an annual variation due to the annual period of the satellite–station geometry. These effects may be as large as 1–2 ns.

Figure 8.6 shows the Allan deviation over 1 and 14 days, respectively. The observations from days 121–158 of 1998 on the short baseline in Wabern were used. During this time period (38 days) the receivers were running on the same clock. Due to different tests performed during the time period only 14 days could be used for the establishment of the Allan deviation. The Allan deviation based on one day of estimates shows the difference between using the observations on different frequencies, i.e., L_1, L_2, and L_3. As mentioned in Chapter 2, the L_2 and L_3 phase observations have a higher noise than the L_1 phase observations. This is clearly reflected by the starting point of the Allan deviations at $\tau = 30$ sec. The noise of the clock estimates based on the three observations types is roughly at the 6–9 ps (2–3 mm) level. After one day the results from the three observation types are almost identical. Figure 8.6 demonstrates that, on short baselines, the GeTT method allows frequency transfer at the 10^{-15} level within one day of observation. The 10^{-14} level is reached after about 2000 sec. With 14 days of observations the 10^{-16} level may be reached for frequency transfer. The strange behavior of the Allan deviation in Figure 8.6(b) around $\tau = 90000$ sec, approximately one day, may be explained by the unequal spacing of the clock estimates (only not consecutive 14 days of a 38 day interval were used). The small excursion observed between $1000 \leq \tau \leq 80000$ may be caused by multipath effects. The slope of the Allan deviation is close to the expected value of -1.

8.2.4 Long Baseline tests

European Baselines

After the successful performance of the GeTT terminals on short baselines it was decided to test the two terminals on longer baselines. The first GeTT terminal was transferred to the National Physical Laboratory (NPL) in the United Kingdom while the other GeTT terminal remained at OFMET in Switzerland. Later on, after about 50 days, the second GeTT terminal was moved from Wabern to the “Physikalisch-Technische Bundesanstalt” (PTB) in Germany. The length of both baselines, NPL–OFMET and NPL–PTB, is approximately 750 km.

The baseline NPL–OFMET was basically used to verify that the receiver at NPL was working properly. At the same time it was used to test our processing strategy for the longer baselines using IGS orbits, station positions, and previously estimated tropospheric zenith delays. Apart from studying the Allan deviation, the results of the GeTT terminals were compared to results stemming from the CV method. Notice, that on this baseline the external

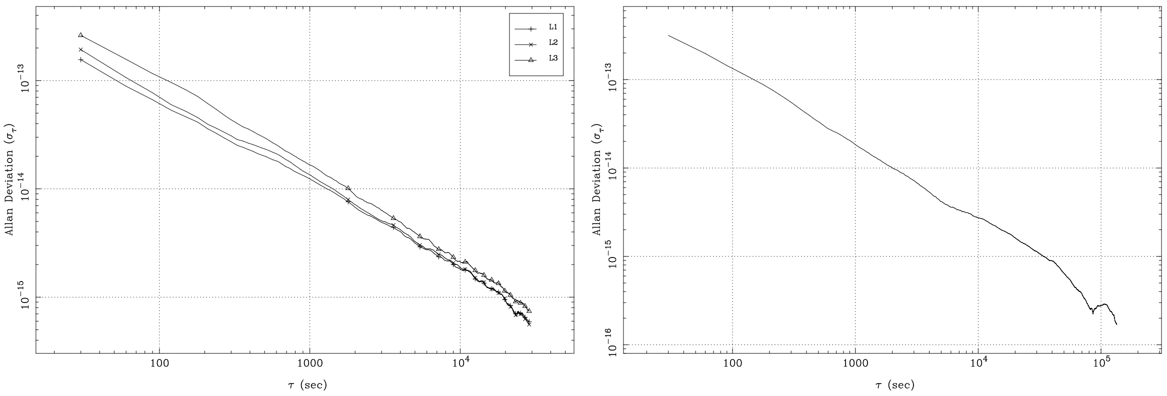

(a) Allan deviations of day 143, 1998 for L_1, L_2, and L_3

(b) Allan deviation over 14-days for L_3

Figure 8.6: Allan deviations of clock estimates from a short baseline with two receivers running on the same clock.

clocks were a hydrogen maser at NPL and a cesium at OFMET, which means that the Allan deviations reflect the short term stability of the cesium standard.

On the second baseline, NPL–PTB, the external clocks on both ends were hydrogen masers. On this baseline a strange effect was observed in the Allan deviations. After some investigations a sinusoidal signal with a period of 724 seconds and an amplitude of 50 ps was observed in the estimates. Test showed that neither the GeTT terminals nor the maser at PTB were causing the problem. One year later the cause of the problem was verified to lie at NPL [*Clarke et al.*, 1999]. This effect never could have been detected with the CV or the TWSTFT method. The CV method would not have been accurate enough (the signals amplitude is only 50 ps) whereas the TWSTFT would not have had the required time resolution (the period being only 724 sec). This demonstrates the high quality of the GeTT method for time and frequency transfer. For more information concerning these European baseline tests we refer to [*Overney et al.*, 1998].

Transatlantic Network

In a next step the receiver from NPL was moved to the United States Naval Observatory (USNO) in Washington, DC. The baseline length between USNO and PTB is approximately 6275 km. Because of this long distance the two stations cannot observe many satellites simultaneously. Therefore, auxiliary stations were included in the process to fill the gap between the two GeTT terminals. It was decided to process a small transatlantic network of 14 stations, but a larger number of stations were selected to make sure that always 14 stations would be available. The stations were selected based on a predefined order with our two GeTT terminals

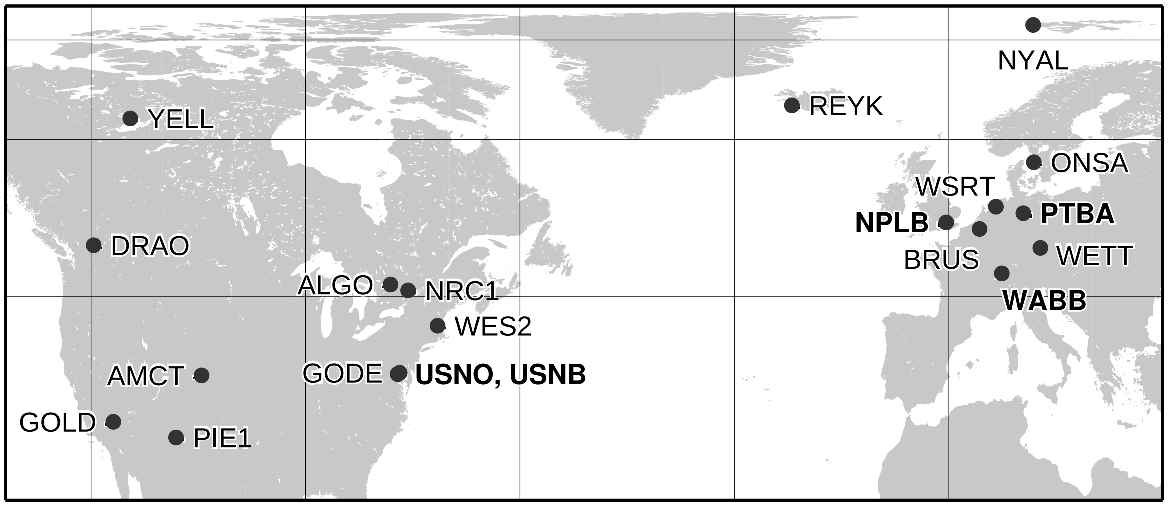

Figure 8.7: Network of time stations used for the transatlantic baseline tests. Only 14 of the available sites are used on any particular day.

having the highest priority. The complete set of stations used in this transatlantic network is shown in Figure 8.7. Notice that there are two receivers located at USNO. The receiver labeled USNO is the official IGS receiver whereas the receiver labeled USNB is our GeTT terminal. Our other GeTT terminal located at the PTB is labeled as PTBA. The receiver at the NPLB site is an Ashtech-Z12T receiver owned by the NPL.

The transatlantic baseline test started on day 200, 1998 and is still in progress. Today, we have almost 300 days of transatlantic time and frequency transfers using the GeTT (and other) terminals. The first topic addressed was associated with the baseline length. With the European baseline tests we found that the slope of the Allan deviations was closer to the value of -0.5 than to the expected value of -1. However, due to the problems with the maser at NPL these results were not fully reliable. In order to study the impact of the baseline length the same set of data was processed using once the GeTT terminal at PTB and once the GeTT terminal at USNB as reference clock. From the results of both solutions the Allan deviations were computed for all (stable) oscillators in the network. Figure 8.8 shows the Allan deviations of the two solutions. The clock estimates are produced with a sampling of 5 minutes (300 sec). Consequently the Allan deviation plots start at $\tau = 300$ sec. Figure 8.8 shows that the noise of the clock estimates for $\tau = 300$ sec lays between the 12 and 30 ps (2–9 mm) which is excellent.

The Allan deviation for USNO, in the solution where the maser at USNB was selected as reference clock, is better (slope close to -1 for $\tau < 2000$ sec) than all others. This is explained by the length of 180 m of the USNO–USNB baseline. This result is comparable to the results for the same baseline in Figure 8.4(b). For the other baselines, with quite big differences in length, no significant baseline length dependence was observed, but the slopes of all curves is close to the value of -0.5. It is unclear why the slopes of the Allan deviations are not closer to a value of -1 for the longer baselines. Possible explanations are remaining systematic effects due to troposphere, ionosphere, station model, and orbit model inaccuracies.

Figure 8.8(a) shows a very similar behavior for all Allan deviations when using the PTB maser as reference. This indicates that the Allan deviations in Figure 8.8(a) are dominated by the behavior of the PTB maser. This finding is confirmed by the results where the USNB clock was used as reference. For frequency transfer, the effect of the reference clock may be eliminated a posteriori by forming differences between the clock estimates. We may, e.g., take the results stemming from the solution where the PTB maser was used as reference and compute the differences between the clock estimates for USNB and all other stations. The Allan deviations obtained from these clock (double-) differences are practically identical with those of the solution where the USNB maser was used as reference. For time transfer this procedure will be more elaborate due to different delays at different sites.

In order to study the effect of the orbit error we processed 21 days of the transatlantic data using both, our CODE rapid and final orbit products. Figure 8.9 shows the Allan deviations of the two sets of 21 days (notice the increased range for τ). No significant difference between the results is observed. Obviously, the quality of the rapid and final orbits is not a limiting factor. The results also demonstrate the high quality of the CODE rapid orbits. In both cases the slope of the Allan deviation is again nearer to a value of -0.5 rather than to -1.

Figure 8.10 shows the clock estimates over the time period from day 200, 1998 to day 129, 1999, a total of 294 days, for four selected stations with very stable oscillators. Notice that the station of AMCT shows up twice in the figure because the receiver and antenna setup was changed. The clock estimates relative to the PTB maser all show a similar pattern. This indicates that the variations are due to the PTB maser. As opposed to the clocks at the other four sites the maser at PTB is not steered. There are only manual interactions in the case of the PTB maser but there is no continuous steering. Some of the manual interactions may be observed at the end of 1998 and the beginning of 1999.

The other four masers are not only steered, they are also synchronized. The masers at USNO are compared locally, the masers at USNO and at AMCT by using the TWSTFT. TWSTFT is usually performed once per day, but on the USNO–AMCT baseline it is performed on an hourly basis. AMCT is the “USNO Alternate Master Clock”, the backup realization of UTC(USNO). The maser at NPL is also synchronized to USNO using TWSTFT but with at a much lower rate. The results using the USNB as reference, obtained by differencing the clock estimates rather than by reprocessing the 294 days, shows the quality of the synchronization of the clocks over the 294 day period. The RMS of the resulting time series are 1.0 and 3.9 ns for the two time series of AMCT, 16.2 ns for NPL, and 1.3 ns for USNO. Note that these values include some undetected jumps, especially for the second part of the AMCT series. In the NPL results we seem to observe an annual variation with an amplitude of about 30 ns. It must be mentioned, however, that many problems were encountered with the NPL data due to the problems with the setup at the NPL. The annual period may not necessarily be attributed

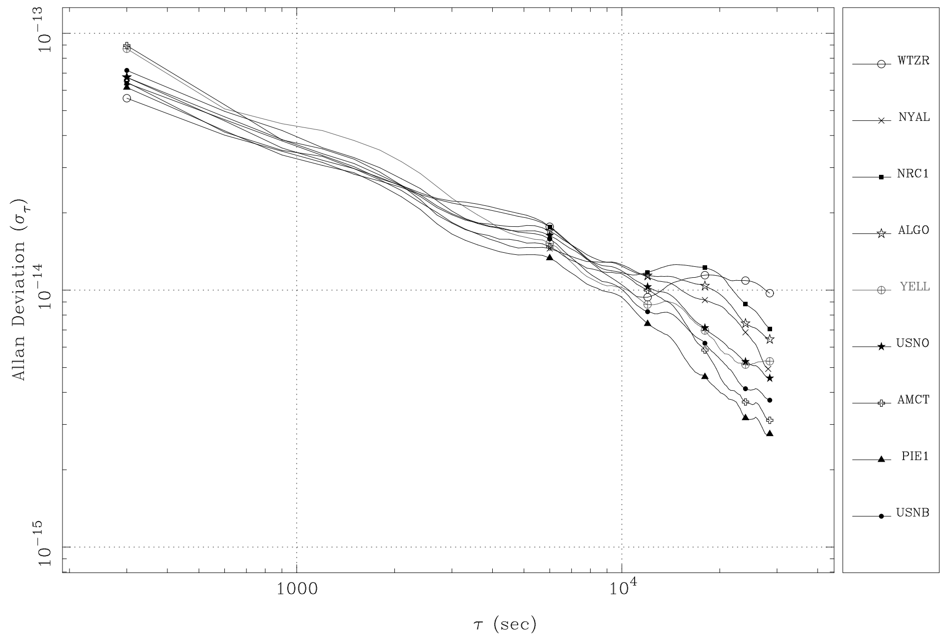

(a) Using the maser at PTB as reference

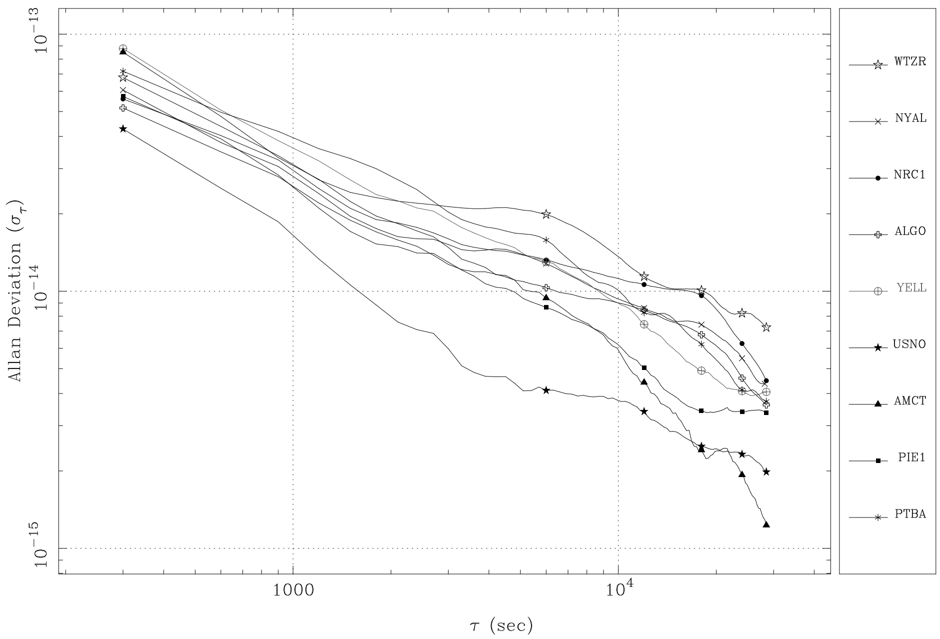

(b) Using the maser at USNB as reference

Figure 8.8: Effect of baseline length on the clock estimates, based on data from day 129, 1999.

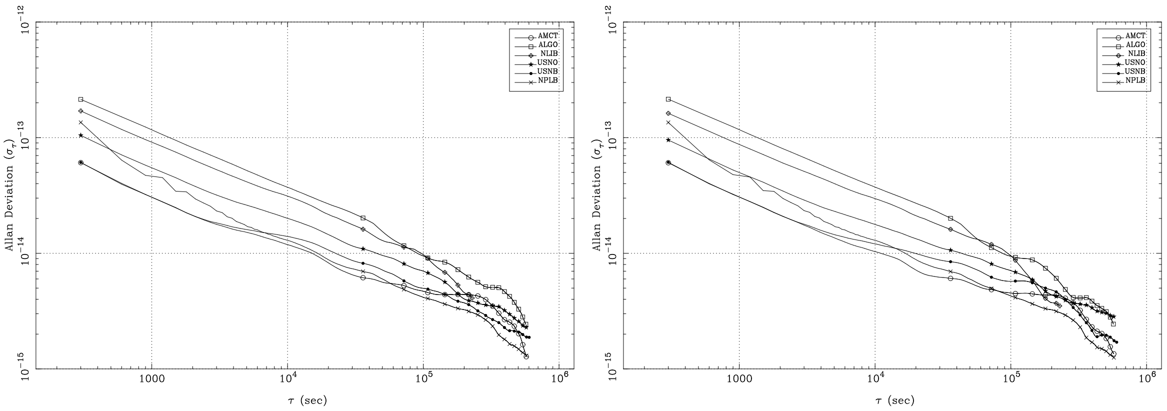

(a) Using rapid products

(b) Using final products

Figure 8.9: Effect of orbit quality on the clock estimates, using transatlantic baselines. Based on data from days 40–60, 1999. The maser at PTB was chosen as reference.

to the maser at NPL and its synchronization to UTC.

Figure 8.11 shows the Allan deviation over the 294 days using USNB as reference. Based on the Allan deviation the noise of the clock estimates is at a level of 12–60 ps ($\tau = 300$ sec). Only the slope for the short baseline, USNO–USNB, seems to be close to a value of -1 for $\tau < 1000$ sec. For the other baselines it is again close to a value of -0.5. We believe that this behavior might be explained by our handling of the tropospheric effects. We estimated one constant tropospheric zenith delay for each 6 hours time interval. During these time intervals the troposphere conditions may vary considerable. This might have an impact on the clock estimates. The signal in the Allan deviation for USNO for $10^4 < \tau < 10^5$ may be caused by multipath effects or it may reflect the stability of the two masers used to steer the two receivers. Notice that the flattening of the Allan deviation for USNO around $\tau = 10^4$ sec was also observed in Figures 8.4 and 8.8. For larger τ the Allan deviation shows the steering of the masers.

A major challenge of using GPS for time transfer consists of the elimination (or at least reduction) of the jumps at the day boundaries (caused by processing the data in 24 hour batches). These jumps are clearly visible in Figure 8.12 where the estimates from four consecutive days of our transatlantic network are shown. An offset and a drift have been removed for all stations and the results have been offset for better visibility. We observe jumps of up to 1 ns (300 mm) caused to a large extent by systematic effects in the code observations (compare Figure 8.3).

One way to reduce this "jump" problem is by using overlapping data spans. These overlaps may be as short as 1 hour or as long as a few days. A more difficult, but also more correct solution would be to make the observations continuous over the day boundaries. This may be done by transferring the ambiguities from the previous solution to the latter solution. The

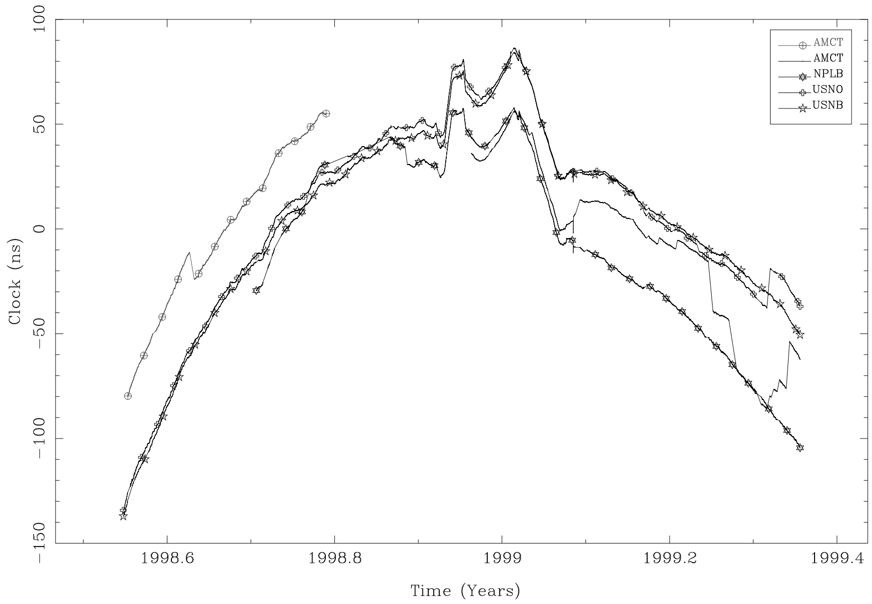

(a) Using PTB as reference

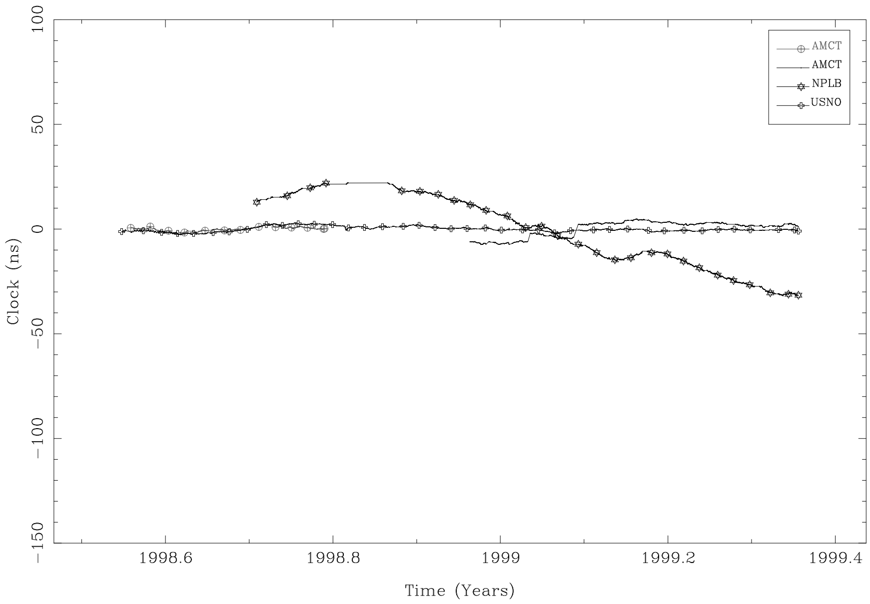

(b) Using USNB as reference

Figure 8.10: Clock estimates over the time period from day 200, 1998 to day 129, 1999. Large jumps and an offset were removed for each station.

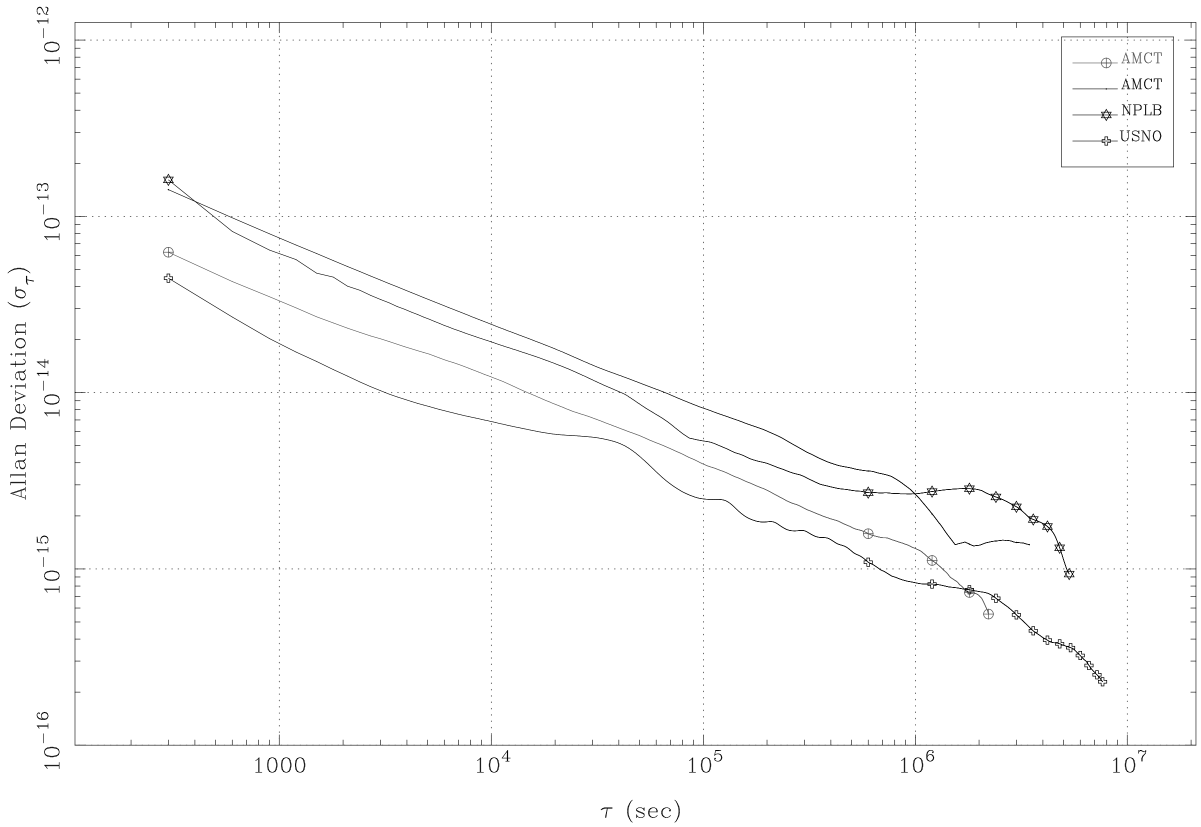

Figure 8.11: Allan deviation of the clock estimates over 294 days using the time period from day 200, 1998 to day 129, 1999. Large jumps and an offset were removed for each station. USNB was used as reference.

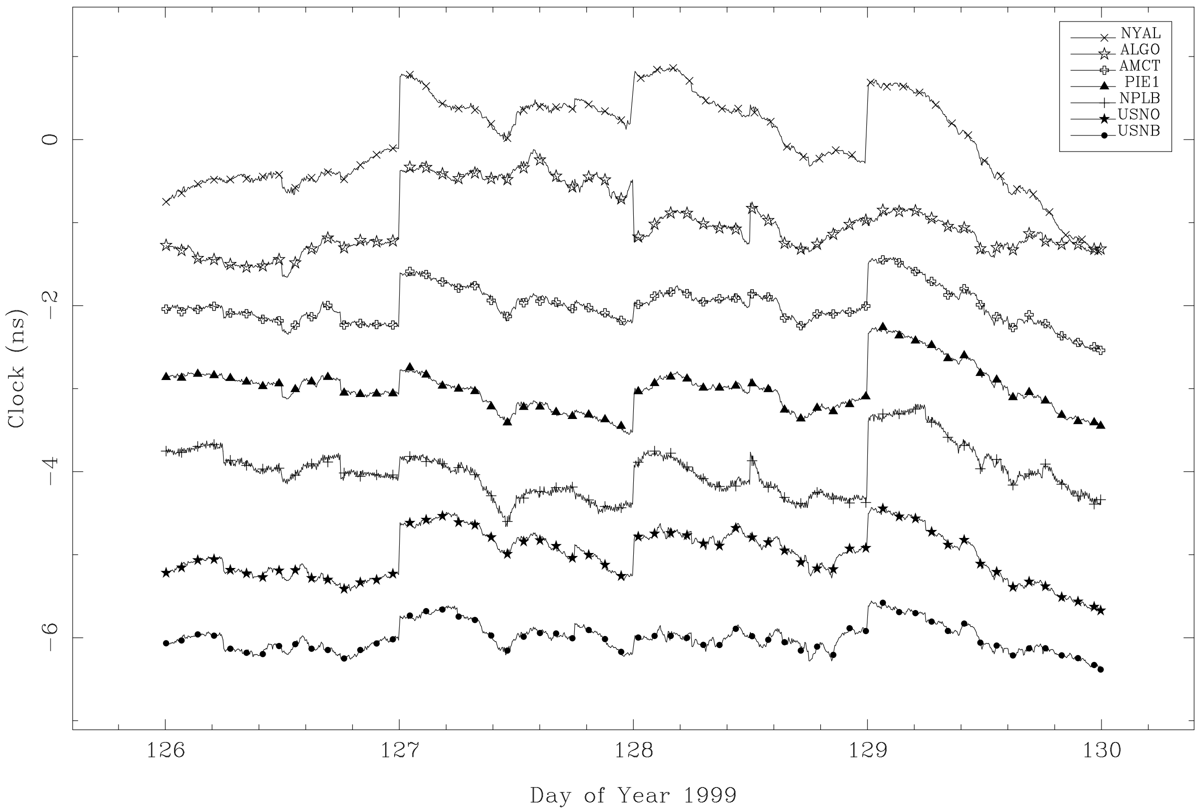

Figure 8.12: Jumps at the day boundaries shown for four consecutive days in 1999. Offset and drift were removed for all stations and PTB was used as reference. The curves were offset for display purposes.

continuity at the day boundary would be guaranteed by such a procedure. We expect the differences between the two approaches to be small.

8.3 IGS Satellite Clock Estimates

At CODE the satellite and station clock estimation is done after having estimated all global parameters using double difference observations. In the clock estimation step optimum use is made of all previously determined parameters. Orbits, Earth rotation parameters, coordinates, and tropospheric zenith delays are taken over from the global solution for the clock estimation. Clock estimation is based on undifferenced data. First, a receiver connected to a stable external oscillator is selected as reference. The clock of this station is then synchronized to GPS time by estimating an offset and a drift for the local oscillator. In this procedure the GPS broadcast ephemerides are used to obtain the clock offsets of the GPS satellites for the synchronization. After the alignment of the clock of the reference receiver the clocks of all stations and satellites, except the reference clock, are estimated. In the clock estimation step we use 80 stations.

CODE started estimating GPS satellite clocks in September 1995. At that time the procedure was based on code observations only. The quality of the clock estimates was at the 1.4 ns level as was shown in Chapter 5. Since January 1997 the satellite clock estimates are based on smoothed code observations and the quality improved to the 0.5 ns level. The achieved quality was close to that of the other IGS Analysis Centers (based on the weekly IGS combination, see Figure 8.13(a)) at that time. After an improvement of the IGS clock combination early in 1998 it became clear that there is a significant quality difference between our clock estimates, based on smoothed code, and the clock estimates of the other ACs which are based on phase and code observations. Smoothed code observations are noisier than phase observations, but this should be partly compensated by the fact that we use almost twice as many stations in our procedure as the other ACs providing clock estimates. The reason for the higher RMS of our clock estimates is caused by systematic effects in the (smoothed) code observations. This is nicely demonstrated in Figure 8.13(b) where the difference between satellite clock estimates based on (smoothed) code and phase observations is displayed. The same data set was used to estimate the satellite clocks using two methods, once using smoothed code observations only, and once using both, the smoothed code and phase observations. Clearly, the clock differences are dominated by systematic effects rather than by noise. The RMS of these clock differences over the full 24 hours is 0.7 ns which corresponds quite well with the RMS for our clock estimates in the IGS clock combination.

As mentioned in the previous sections we may also use phase observations to estimate clocks. However, due to hardware and software limitations we are limited to processing a network of 30 stations when processing undifferenced phase measurements. This is due to the big number of ambiguity parameters which have to be estimated in this case, about 60 per station per 24 hours, i.e., 1800 ambiguity parameters in the case of 30 stations. Due to this large number of ambiguity parameters the processing of the phase measurements requires

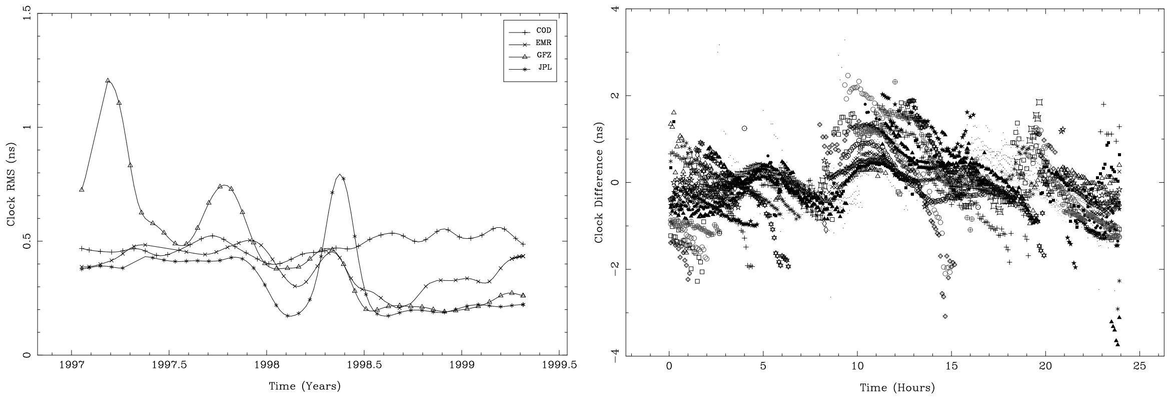

(a) Quality of AC satellite clock estimates

(b) Difference between smoothed code and phase clock estimates

Figure 8.13: Quality of AC satellite clock estimates compared to IGS final combined clocks (left). Difference between satellite clock estimates based on smoothed code and phase observations (right). Different symbols represent different GPS satellites.

more CPU time. We have therefore not switched to using the undifferenced phase observations except for 4 days in GPS week 960. The RMS of the clock estimates for these days in the IGS clock combination were 0.1–0.2 ns, which is comparable to the clock estimates of the other ACs. Due to the limited use of the satellite clocks, especially for double difference processing schemes, we have refrained from switching to phase based satellite clock estimates.

8.3.1 Precise Point Positioning

One of the most important applications of the IGS satellite clock estimates is precise point positioning [*Zumberge et al.*, 1997*b*]. In this approach the satellite positions and clocks are used together with the code and phase data of one single receiver. The position of this station may then be determined with a precision comparable to that of the global solution. Precise point positioning thus provides a very efficient tool to access the terrestrial reference frame. In Figure 8.14 the daily position estimates for the station PTB in Germany (our GeTT terminal) are shown over a time period of 100 days. Once the station positions were estimated using the "classical" double difference approach and once the station positions were estimated using precise point positioning. In the double difference approach the station of Wettzell (400 km distance to PTB) was used to form differences and Wettzell was fixed to its ITRF coordinates. In the case of precise point positioning the satellite clock estimates from our transatlantic time transfer project were used. Our clock estimates based on smoothed code are less precise than the phase-based satellite clock estimates from the transatlantic campaign. In both solutions the same parameters were estimated, i.e., the position of PTB, ambiguities, and 12 tropospheric

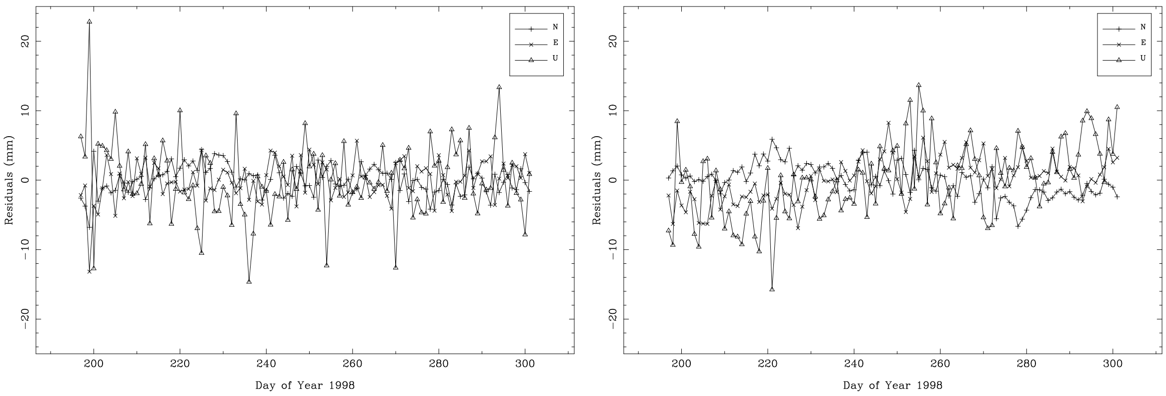

(a) Double difference solution

(b) Precise point positioning solution

Figure 8.14: Daily position determinations over 100 days using different processing strategies.

zenith delay parameters per 24 hours. In addition 12 tropospheric zenith delays for Wettzell had to be estimated in the double difference approach, whereas for the point positioning approach the clock offsets of the station PTB had to be estimated (288 parameters at a 5 min sampling). The RMS of the variations in the daily station coordinate estimates for both approaches is 2, 3, and 6 mm for the north, east, and up directions, respectively. This shows the high precision which may be obtained with the point positioning technique. It is interesting to point out that both approaches have reached the same repeatability as the European solution without fixed ambiguities, see Table 5.3.

The main disadvantage of the point positioning strategy is the impossibility to fix ambiguities (ambiguities may only be fixed on the double difference level). Whereas the results from the double difference approach may be improved by fixing the ambiguities, as we have shown for our European solutions in Table 5.3, this will not be possible in the case of precise point positioning. There are two additional disadvantages of precise point positioning. First, it has to rely on undifferenced data cleaning which is more difficult than cleaning double difference data. Secondly, it is of the utmost importance that the models used in generating the GPS orbit and clock estimates are consistent with the models applied when using these estimates in point positioning. Nevertheless, point positioning provides a very efficient tool for determining station positions with a precision which will be sufficient for the vast majority of the GPS users. Only users who want to get the best possible results from the GPS system will not be satisfied with the results from point positioning.

9 Summary and Outlook

We have shown the significant improvements, in only a few years time, for many of the IGS products and have presented the “state of the art” of the IGS products. We have seen that the internal product consistency between IGS Analysis Centers has reached the 30–50 mm level for orbits, 3–8 mm for station positions and 0.1 mas for polar motion. Significant biases exist between individual analysis center solutions. Differences of 0.5 ppb (10–15 mm) in the scale of the orbits, 3 ppb (15–20 mm) in the terrestrial scale, and 100 mm in geocenter estimates are observed in internal comparisons. Biases also became apparent when comparing results from different techniques, e.g., GPS, SLR and VLBI. In these comparisons a bias of 0.3 mas for the X-component of the pole was observed. Furthermore, a persisting bias of approximately 50 mm is observed between SLR range observations and the ranges to the GPS satellites derived from the IGS orbits and the SLR station positions. A bias of approximately the same size was observed for the GLONASS satellites.

We could demonstrate that the new CODE solar radiation pressure model is superior to the ROCK RPR models. The remaining model error was estimated to be about 50 cm for the CODE RPR model for a 7-day arc. For the ROCK model the remaining error was shown to be approximately 300 cm for a 24 hour arc. The implementation of the CODE RPR model improves the quality of orbit estimates. The number of orbit parameters that have to be estimated is considerably reduced when using the new CODE RPR model as a priori model. This fact strengthens the GPS solutions significantly. The generation of so-called “rapid” products may profit from this development. The quality, and in particular the reliability, of predicted orbits may also be improved. Although significant improvements were achieved with the new CODE solar radiation pressure model, it should be considered as a “first attempt” only. In the near future more time and effort will have to be spent on the solar radiation pressure model for the GPS satellites. Different models are required for the different satellite Block types (I, and IIR). The current model is only valid for the Block II and IIA satellites. The behavior of some of the parameters of the CODE RPR model is significantly different, but not erratic, during the eclipse phases. This indicates that special eclipse models should be derived.

The comparison of the observed ranges, based on the SLR tracking data, and the computed ranges, based on the GPS satellite orbits as provided by the IGS and the SLR station positions, revealed an average bias of approximately 50 mm, the observed SLR ranges being shorter than the computed ranges. The reason for this bias must be studied and, hopefully, resolved in the near future. The RMS agreement between the SLR ranges and the GPS orbits, after subtracting the mean bias, was found to be as low as 50 mm. This is a very encouraging result. It shows that the two independent techniques, GPS and SLR, agree at the few cm level. Also, the SLR station coordinates, estimated using only the SLR observations of the GPS satellites, agree at the few cm level with their ITRF values. The usage of the SLR data of the GLONASS satellites offered another possibility to study the observed microwave–SLR bias. For the GLONASS satellites there is significantly more SLR tracking data available because of the much larger retroreflector array compared to the GPS satellites. The IGEX orbits for the GLONASS satellites are of inferior quality compared to the IGS orbits for the GPS satellites. This is caused by the poor geometry of the IGEX receiver network. Nevertheless, the IGEX orbits and the large amount of SLR tracking data revealed a bias of the same size and sign as that observed for the GPS satellites.

The new CODE solar radiation pressure model allows to generate GPS orbits based on only SLR observations. Previously, the limited number of SLR observations and the large number of orbit parameters required to accurately model the GPS satellites made it almost impossible to generate precise GPS orbits based on SLR data alone. With the CODE RPR model we are in a much better position because it allows a 7-day orbit fit through the IGS precise ephemerides at the 6 cm level solving for only two RPR parameters. Using the CODE RPR model we were able to generate relatively precise "SLR-only orbits" which were helpful in studying the bias observed between the SLR observations and the IGS precise orbits. The SLR-only orbits showed a geocenter shift in the Z-direction compared to the microwave orbits of approximately 50 mm. The geocenter of the SLR orbit lying below the geocenter resulting from the microwave orbits. Most likely this Z-translation is caused by the observed bias together with the geometry of the SLR tracking network with most of the stations in the Northern hemisphere.

We furthermore discussed the potential of GPS and IGS for time transfer. The results showed that the IGS is capable of providing clock information on a routine basis to the timing community allowing time transfer on a level of a few 100 ps. It was also demonstrated that the availability of precise IGS orbit and clock estimates for the GPS satellites allows for a very efficient and accurate determination of the station position using data from one single receiver. The accuracy of this so-called precise point positioning technique is sufficient for most GPS users.

The realization of the terrestrial reference frame, ambiguity fixing, orbit modeling, elevation cut-off angle, and troposphere modeling play an important role in the quality of the IGS products. We are convinced that we have not yet exploited the full potential of the GPS and that we can still significantly improve the precision of some of our products. Improvements at CODE may be expected in the near future from improvements in the tropospheric zenith delay estimates by making the estimates continuous in time. The estimation of tropospheric gradients will further improve our global solutions. Ambiguity fixing on longer baselines and the connection of the ambiguities over the day boundaries promise additional benefits. We also expect improvements from the inclusion of GLONASS microwave observations thanks to the increased number of satellites. At the same time this will unify the IGS and IGEX products. We consider this to be an important aspect. Furthermore, the combination of SLR and microwave observations, from both the GPS and GLONASS satellites, may have a significant impact on results. In the combination of microwave and SLR observations we should, however, not limit ourselves to using only the microwave satellites. The typical SLR targets, cannonball satellites like, e.g., ETALON (in orbital planes similar to those of the GLONASS satellites), and LAGEOS (at 6000 km altitude) should also be included when combining the observations of the two techniques.

The developments within the IGS have been relatively difficult to predict because of the amazing speed with which the IGS has developed in its first years. Although there are some indications that the pace of new developments and of precision improvements is slowing down there are still many new projects on the horizon. First of all, in October 1999, the IGS has announced to start a series of so-called "ultra-rapid" products. These products will be made available twice per day at 3:00 and 15:00 UTC. At both epochs a 48 hour orbit is made available containing a 24 hour "real" orbit and a 24 hour predicted orbit. The predicted orbit starts 3 hours before the time of availability of the product, i.e., at 0:00 for the submission of 3:00 UTC, and at 12:00 for the submission of 15:00 UTC. This implies that the average age of the predicted orbits will be 9 hours only. This is a significant reduction compared to the current average age of 36 hours. For orbit predictions the errors grow approximately quadratically as a function of extrapolation time. Therefore, the reduction of the age of the predictions will give a very significant improvement of the orbit prediction quality. This new product adds to the burden of the IGS analysis centers forcing them to compute rapid orbits within 3 hours twice per day. In addition this ultra-rapid scheme is only considered to be a "first step". The aim is to generate hourly products in the near future. This may be of considerable interest for meteorology. The water vapor content in the atmosphere is one of the most important unknown parameters in numerical weather prediction models. The GPS-based tropospheric zenith delay estimates contain information about the amount of water vapor in the atmosphere in the vicinity of the GPS receivers and are therefore interesting for the numerical weather predictions. However, the meteorologists are only interested in the zenith delays if they have access to them in near real-time, typically within a couple of hours.

Another very important future IGS activity is in the field of the Low Earth Orbiting (LEO) satellites. Again, there is a close link to meteorology because several of the planned LEO missions will be used for atmospheric "sounding". A LEO satellite can observe the GPS signals of a "rising" or "setting" GPS satellite, which travel through the Earth's atmosphere. These signals allow, under certain assumptions, to derive atmosphere profiles of temperature and humidity. These profiles are very useful as well in the numerical weather predictions and therefore will have to be available in a timely manner. Other planned LEO missions will focus on, e.g., the Earth's gravity field. These mission are much more interesting from a geodynamical point of view.

Apart from these two new projects there are several active pilot projects currently underway within the IGS like, e.g., the reference frame project, the IGS/BIPM time and frequency project, and the ionosphere and troposphere projects. We conclude that the IGS is still very active and that the CODE analysis center may look forward to many years of interesting and rewarding scientific results based on the activities within the framework of the IGS.

A The CODE RPR-Model

A.1 Time Series of the Parameters of the Extended Orbit Model

It should be noted that all RPR estimates are "scaled" to correct for the distance of the satellite to the Sun. Otherwise a clear annual signal would have been present due to the eccentricity of the Earth orbit.

Figure A.1 shows the estimates of the parameters of the extended orbit model, i.e., D0, Y0, B0, BC, and BS from eqn. (6.7), based on the IGS orbit computations as performed by CODE. In addition, the estimated velocity changes in the along-track direction are shown. Only estimates for the satellites in orbital plane A are shown (PRNs 9, 25, 27). Quite similar estimates are observed for all satellites.

A.2 Direct Solar Radiation Pressure Accelerations

Figure A.2 shows the estimates of the direct solar radiation pressure (D0-term) of the optimal orbit parameterization, see eqn. (6.8). The satellites are grouped according to orbital planes. The problematic satellites were omitted from the figures (PRNs 14, 16, 18, 19, 23, 24, and 29). The estimates are stemming from using satellite positions as pseudo-observations. Very similar estimates are observed for all satellites.

A.3 Y-bias Accelerations

Figure A.3 shows the estimates of the Y-bias (Y0-term) of the orbit parameterization given in eqn. (6.8). The satellites are grouped according to orbital planes. The problematic satellites were omitted from the figures (PRNs 14, 16, 18, 19, 23, 24, and 29). The estimates are stemming from using satellite positions as pseudo-observations. Very similar estimates are observed for all satellites.

A.4 Z1 Accelerations

Figure A.4 shows the estimates of the periodic Z1-term of the orbit parameterization given in eqn. (6.8). The satellites are grouped according to orbital planes. The problematic satellites were omitted from the figures (PRNs 14, 16, 18, 19, 23, 24, and 29). The estimates are stemming from using satellite positions as pseudo-observations. Very similar estimates are observed for all satellites.

A.5 Momentum Wheel Problems

Figure A.5 shows the effect of the loss of momentum wheels on the estimated radiation pressure parameters. Due to this defect the attitude control of the satellite has to be performed with occasional thruster firings. Because the thrusters are never perfectly aligned this will always result in a small orbit maneuver. The estimates are stemming from using satellite positions as pseudo-observations.

A.6 The CODE RPR Model

Tables A.1 and A.2 give the actual parameter values of the CODE RPR model. In addition Table A.3 includes some statistical information.

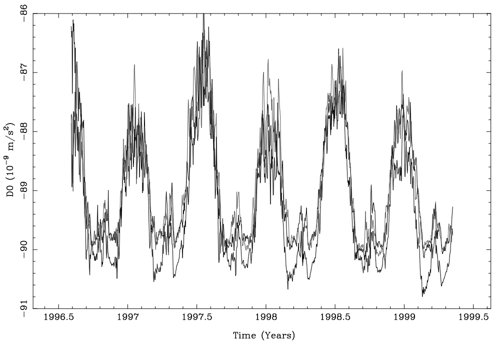

(a) Direct solar radiation pressure acceleration

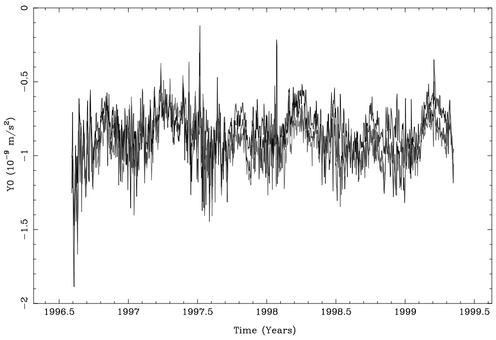

(b) Y-bias acceleration

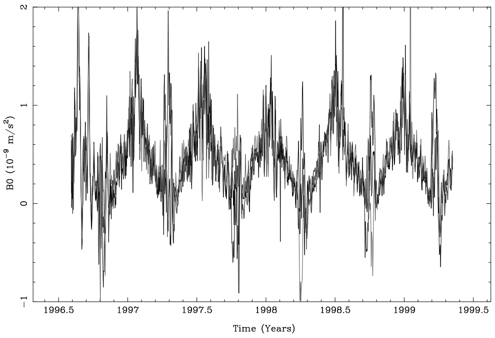

(c) B0 acceleration

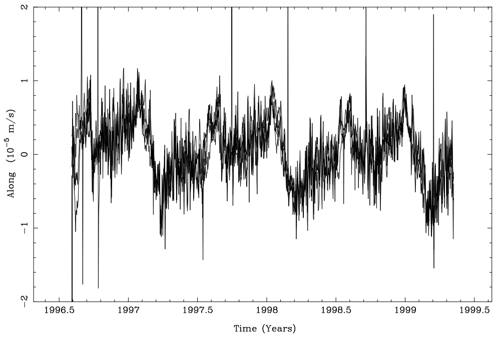

(d) Along-track velocity changes

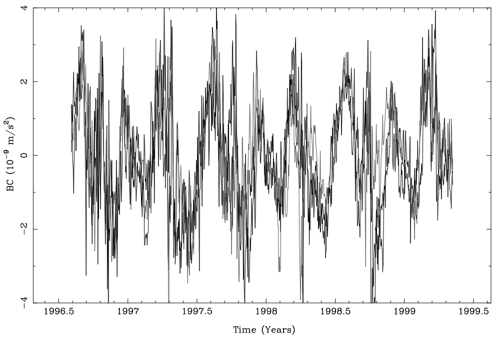

(e) BC acceleration

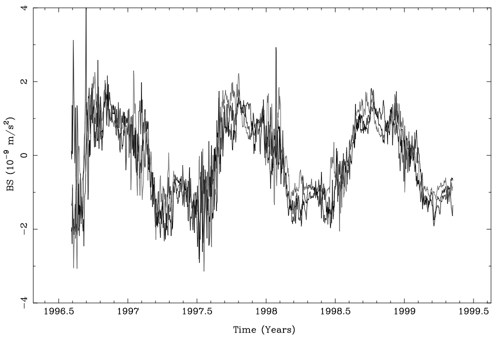

(f) BS acceleration

Figure A.1: Time series of the parameters of the extended orbit model for the satellites in orbital plane A (PRNs 9, 25, 27) from day 217 (August) in 1996 to day 129 (May) in 1999.

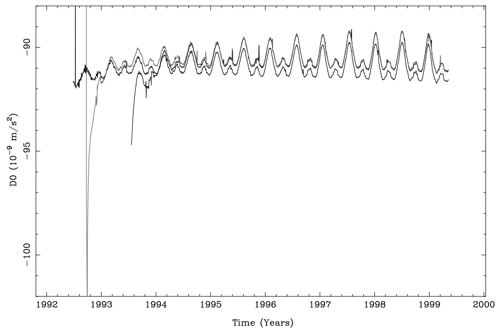

(a) D0 acceleration for the satellites in orbital plane A (PRNs 9, 25, 27)

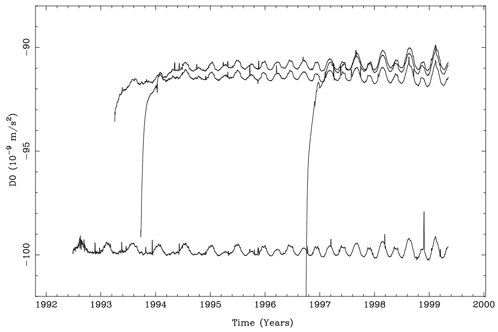

(b) D0 acceleration for the satellites in orbital plane B (PRNs 2, 5, 22, 30)

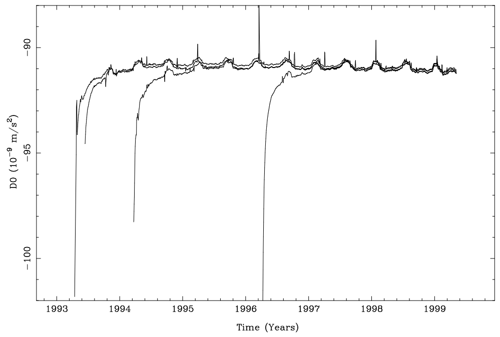

(c) D0 acceleration for the satellites in orbital plane C (PRNs 3, 6, 7, 31)

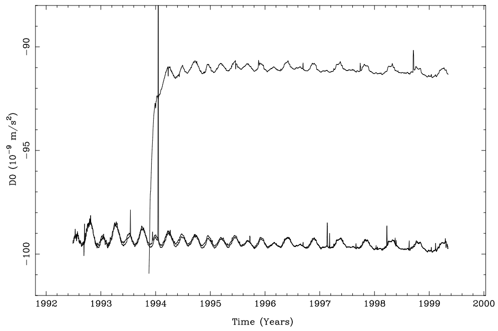

(d) D0 acceleration for the satellites in orbital plane D (PRNs 4, 15, 17)

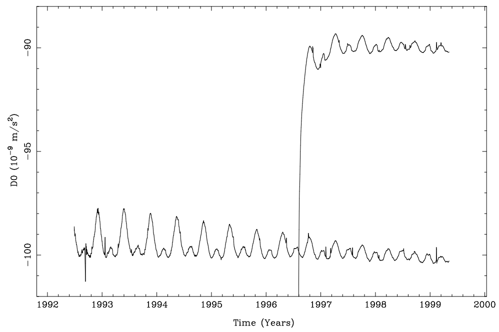

(e) D0 acceleration for the satellites in orbital plane E (PRNs 10, 21)

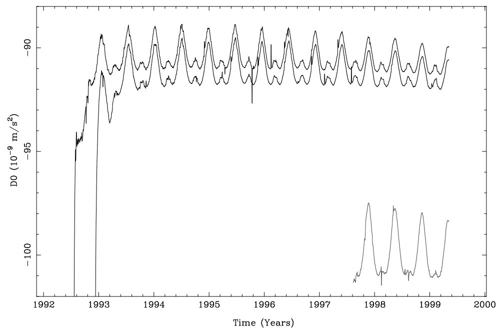

(f) D0 acceleration for the satellites in orbital plane F (PRNs 1, 13, 26)

Figure A.2: Estimated direct solar radiation pressure acceleration (D0), for different orbital planes, from June 1992 to May 1999.

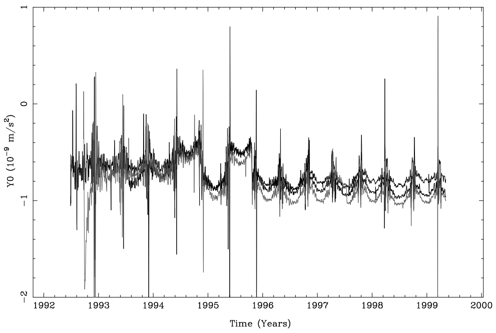

(a) Y-bias acceleration for the satellites in orbital plane A (PRNs 9, 25, 27)

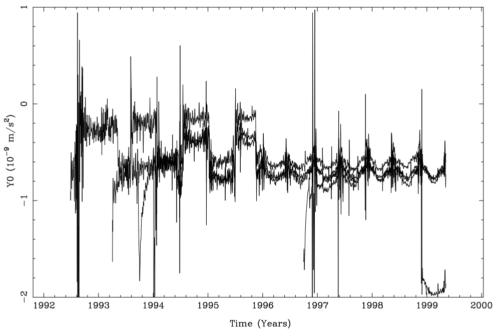

(b) Y-bias acceleration for the satellites in orbital plane B (PRNs 2, 5, 22, 30)

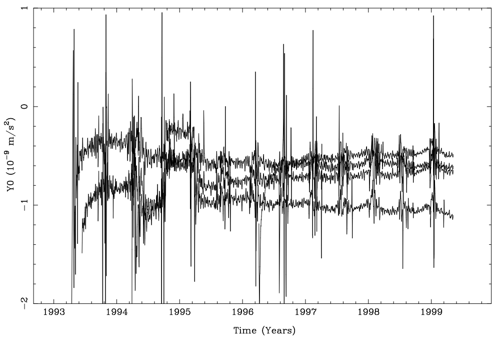

(c) Y-bias acceleration for the satellites in orbital plane C (PRNs 3, 6, 7, 31)

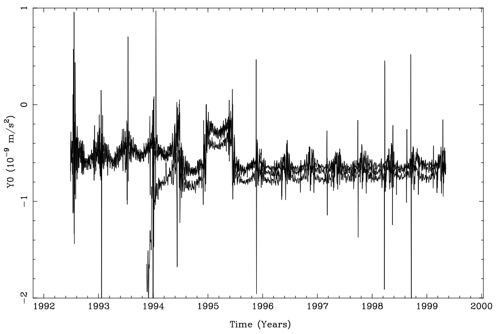

(d) Y-bias acceleration for the satellites in orbital plane D (PRNs 4, 15, 17)

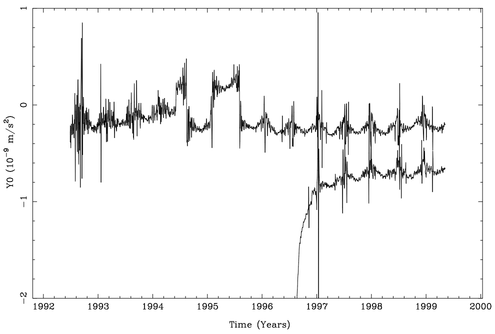

(e) Y-bias acceleration for the satellites in orbital plane E (PRNs 10, 21)

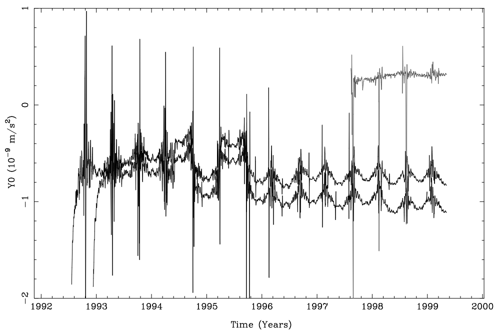

(f) Y-bias acceleration for the satellites in orbital plane F (PRNs 1, 13, 26)

Figure A.3: Estimated Y-bias acceleration, for different orbital planes, from June 1992 to May 1999.

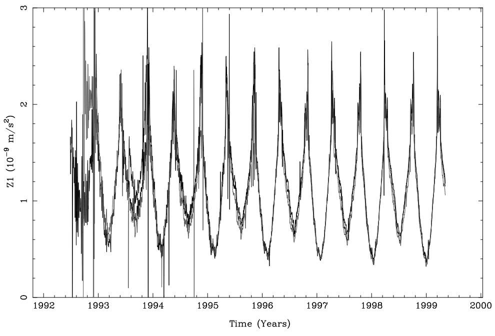

(a) Z1 acceleration for the satellites in orbital plane A (PRNs 9, 25, 27)

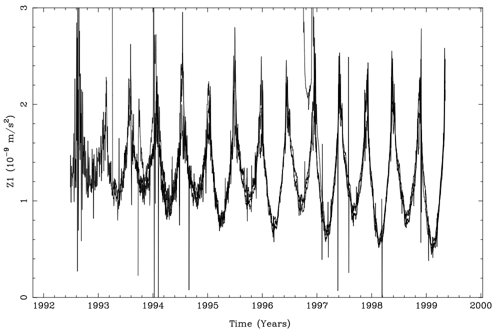

(b) Z1 acceleration for the satellites in orbital plane B (PRNs 2, 5, 22, 30)

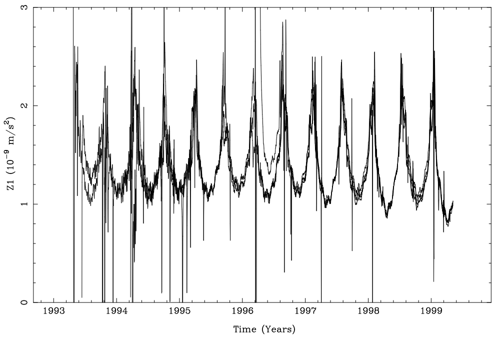

(c) Z1 acceleration for the satellites in orbital plane C (PRNs 3, 6, 7, 31)

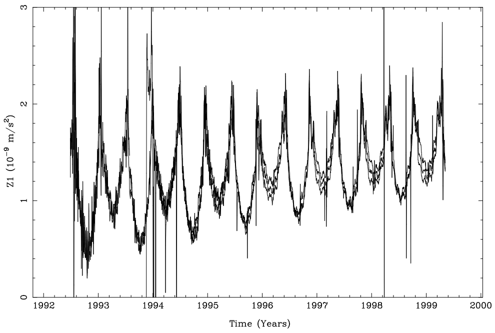

(d) Z1 acceleration for the satellites in orbital plane D (PRNs 4, 15, 17)

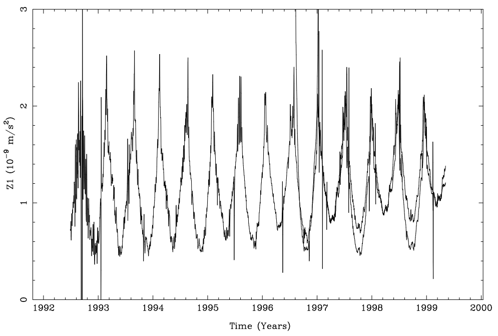

(e) Z1 acceleration for the satellites in orbital plane E (PRNs 10, 21)

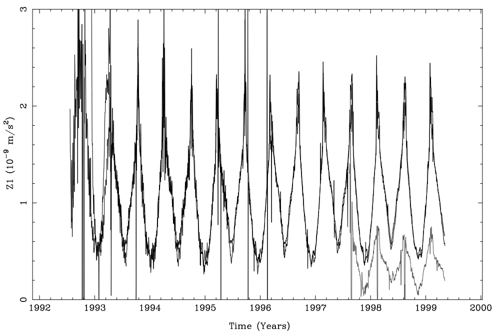

(f) Z1 acceleration for the satellites in orbital plane F (PRNs 1, 13, 26)

Figure A.4: Estimated Z1 acceleration, for different orbital planes, from June 1992 to May 1999.

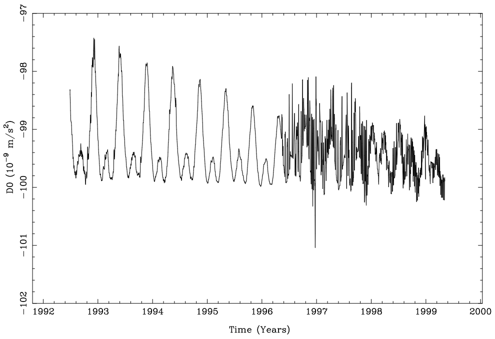

(a) D0 acceleration for PRN 14

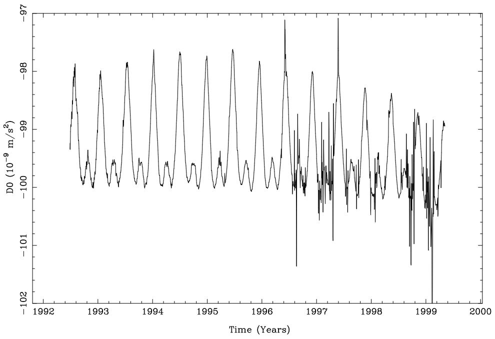

(b) D0 acceleration for PRN 18

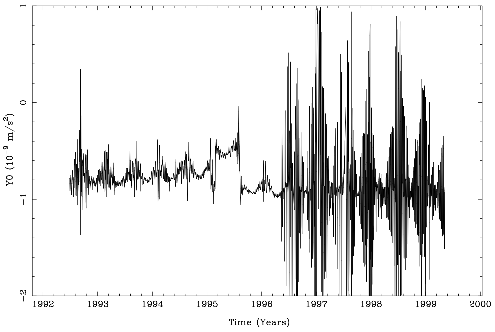

(c) Y-bias acceleration for PRN 14

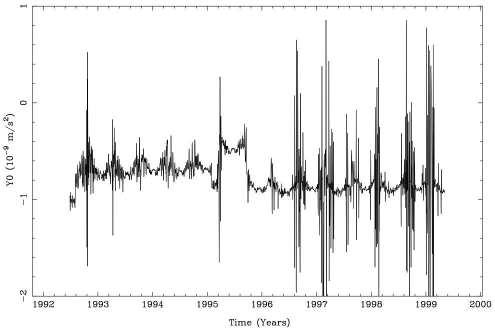

(d) Y-bias acceleration for PRN 18

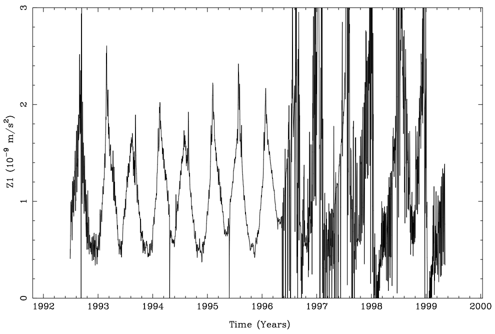

(e) Z1 acceleration for PRN 14

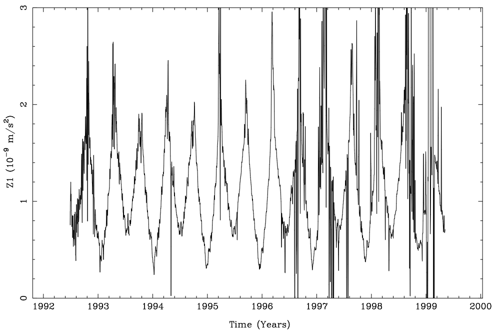

(f) Z1 acceleration for PRN 18

Figure A.5: Effect of attitude control using thruster firings due to the malfunctioning of momentum wheels. Estimated radiation pressure parameters (D0, Y0, and Z1) for PRN 14 in plane E (on the left) and PRN 18 in plane F (on the right) from June 1992 to May 1999.

PRN	Block	$D0_0$ $(10^{-9}m/s^2)$		$Y0_0$ $(10^{-9}m/s^2)$		$B0_0$ $(10^{-9}m/s^2)$	
2	II	-99.423	0.003	-0.628	0.001	-0.044	0.004
14	II	-99.225	0.385	-0.907	0.196	0.246	0.576
15	II	-99.036	0.003	-0.701	0.001	0.498	0.004
16	II	-99.165	0.353	-0.635	0.174	0.115	0.516
17	II	-99.054	0.321	-0.659	0.155	0.072	0.427
18	II	-99.412	0.346	-0.865	0.157	0.438	0.463
19	II	-99.886	0.339	-0.697	0.163	0.114	0.487
20	II	-100.391	0.971	-0.663	0.429	0.519	1.173
21	II	-99.538	0.003	-0.254	0.001	-0.111	0.004
1	IIA	-91.146	0.003	-0.747	0.001	0.512	0.004
3	IIA	-90.398	0.003	-0.531	0.001	0.393	0.004
4	IIA	-90.573	0.003	-0.781	0.001	0.239	0.004
5	IIA	-90.477	0.003	-0.742	0.001	0.241	0.004
6	IIA	-90.407	0.003	-0.730	0.001	0.337	0.004
7	IIA	-90.305	0.003	-1.054	0.001	0.231	0.004
8	IIA	-90.479	0.005	-0.861	0.002	0.284	0.006
9	IIA	-90.372	0.003	-0.788	0.001	0.365	0.004
10	IIA	-89.517	0.004	-0.739	0.001	0.153	0.004
22	IIA	-91.017	0.003	-0.725	0.001	0.045	0.004
23	IIA	-80.403	1.005	-0.753	0.245	0.967	0.910
24	IIA	-91.490	0.332	-1.050	0.164	0.205	0.458
25	IIA	-90.848	0.003	-0.872	0.001	0.396	0.004
26	IIA	-90.448	0.003	-0.998	0.001	0.424	0.004
27	IIA	-90.350	0.003	-0.956	0.001	0.429	0.004
28	IIA	-90.954	0.628	-0.819	0.320	0.136	0.883
29	IIA	-91.081	0.332	-0.919	0.150	0.524	0.418
30	IIA	-90.397	0.004	-0.783	0.001	0.526	0.004
31	IIA	-90.426	0.003	-0.621	0.001	0.641	0.004
13	IIR	-100.148	0.741	0.305	0.206	1.839	0.705

Table A.1: Satellite-specific parameter values and formal errors of the CODE solar radiation pressure model. The values for PRN 13 should be used with care. PRN 13 is a completely new type of satellite (Block IIR) which most likely will show a different solar radiation pressure pattern. The large differences in the formal errors are caused by the weighting of the problematic satellites.

Parameters	Estimate $(10^{-9}m/s^2)$	Formal Error $(10^{-11}m/s^2)$
$D0_{C2}$	-0.812	0.194
$D0_{C4}$	0.523	0.147
$Y0_{C2}$	0.066	0.086
$B0_{C2}$	-0.394	0.232
$Z1_0$ Block II	1.018	0.253
$Z1_0$ Block IIA	0.982	0.138
$Z1_{C2}$	0.517	0.180
$Z1_{S2}$	0.120	0.110
$Z1_{C4}$	0.047	0.193
$Z1_{S4}$	-0.047	0.122
$X1_0$	-0.010	0.138
$X1_{C2}$	-0.014	0.263
$X1_{S2}$	-0.000	0.156
$X3_0$	-0.020	1.150
$X3_{C2}$	-0.058	2.172
$X3_{S2}$	-0.576	1.287

Table A.2: General parameters of the CODE solar radiation pressure model

Parameters	#Est.	RMS $(10^{-9}m/s^2)$
$D0(\beta_0)$	28391	0.1124
$Y0(\beta_0)$	26815	0.0462
$B0(\beta_0)$	26569	0.1275
$Z1(\beta_0)\sin(u-u_0)$	25807	0.1127
$X1(\beta_0)\sin(u-u_0)$	24625	0.1653
$X3(\beta_0)\sin 3(u-u_0)$	26193	1.3644

Table A.3: Statistics from the CODE solar radiation pressure model estimation

B SLR residuals

B.1 SLR Residuals as a Function of Elevation

Figures B.1 and B.2 show the residuals as a function of elevation for the six SLR stations with the most observations over the time span from 1995 to day 200 (July) in 1999.

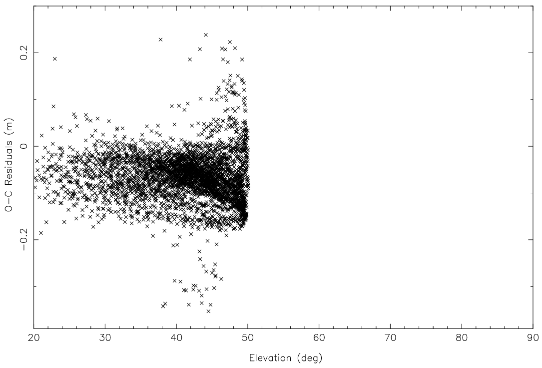

(a) PRN 5 residuals for 7210 MAUI

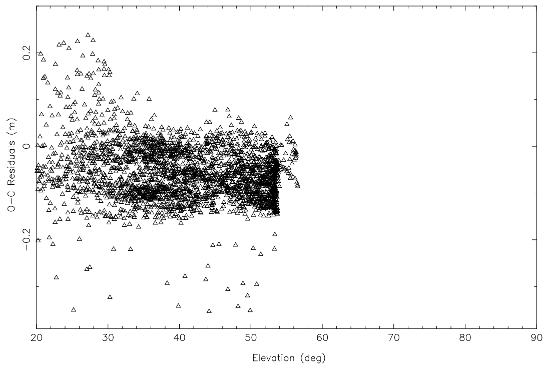

(b) PRN 6 residuals for 7210 MAUI

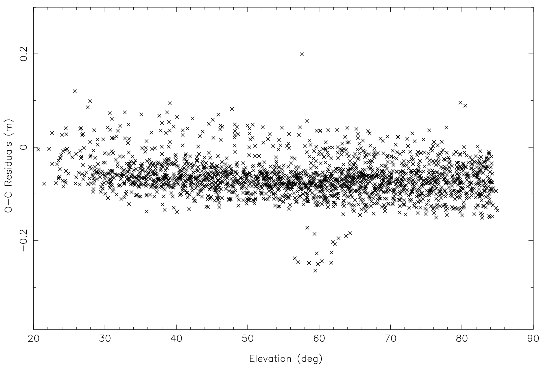

(c) PRN 5 residuals for 7110 MONP

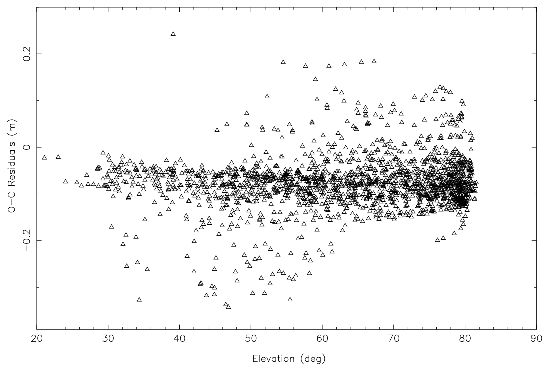

(d) PRN 6 residuals for 7110 MONP

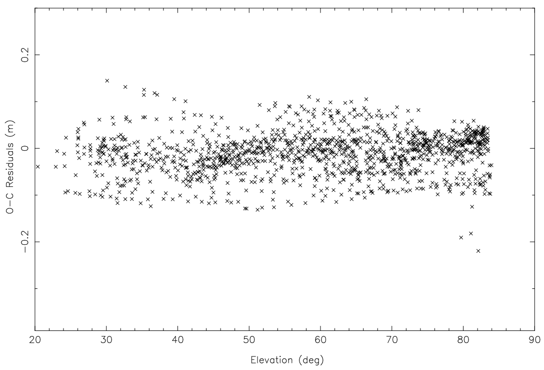

(e) PRN 5 residuals for 8834 WETT

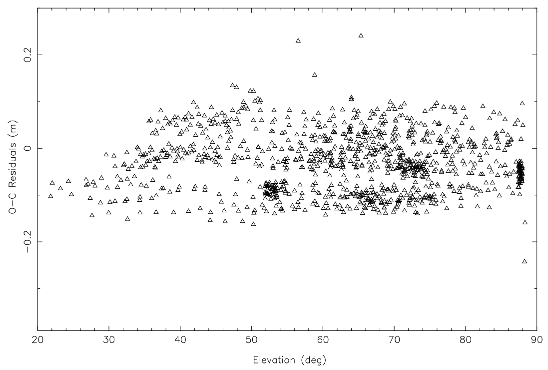

(f) PRN 6 residuals for 8834 WETT

Figure B.1: SLR residuals as a function of elevation for individual station and satellite combinations for the time span from 1995 to day 200 in 1999.

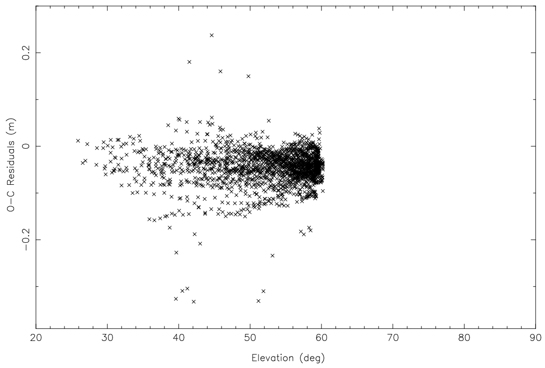

(a) PRN 5 residuals for 7090 YARR

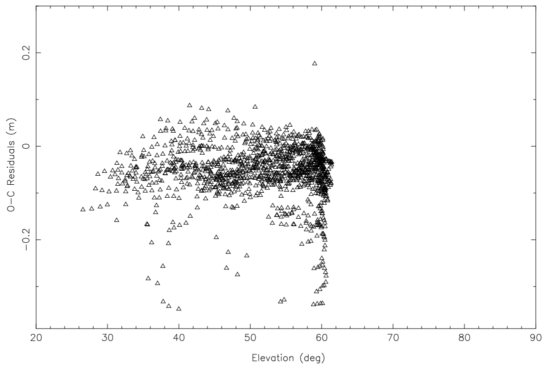

(b) PRN 6 residuals for 7090 YARR

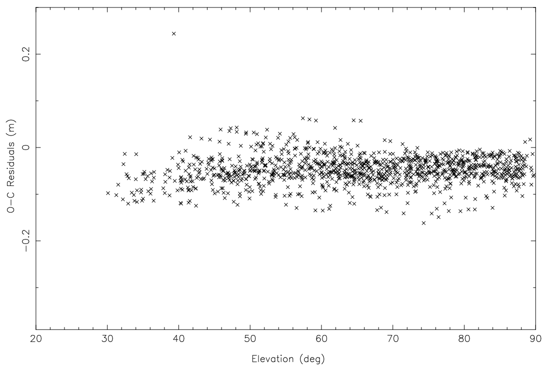

(c) PRN 5 residuals for 7840 HERS

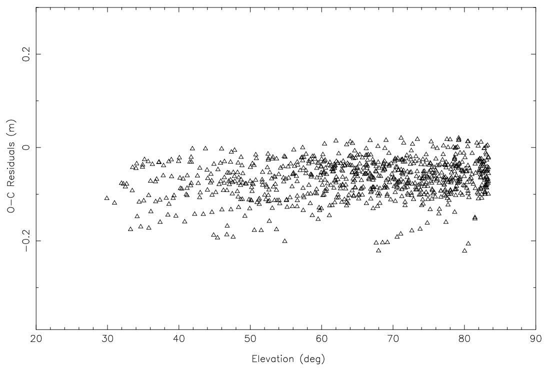

(d) PRN 6 residuals for 7840 HERS

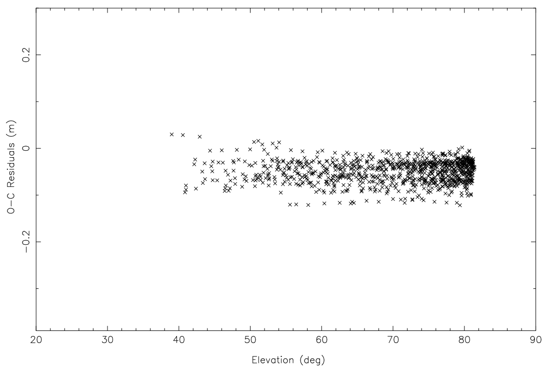

(e) PRN 5 residuals for 7839 GRAZ

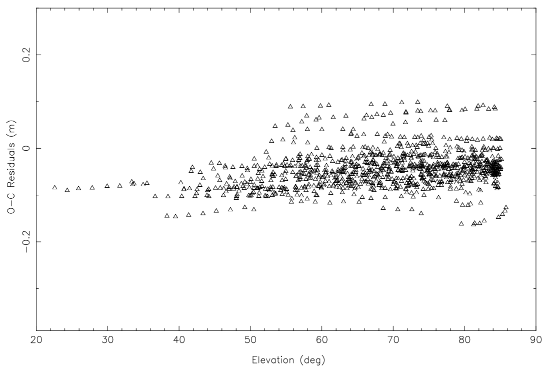

(f) PRN 6 residuals for 7839 GRAZ

Figure B.2: SLR residuals as a function of elevation for individual station and satellite combinations for the time span from 1995 to day 200 in 1999.

Bibliography

Allan, D.W., and M. Weiss (1980), Accurate time and frequency transfer during common-view of a GPS satellite, in 34^{th} *IEEE Symposium on Frequency Control*, Philadelphia.

Ashby, N., and M. Weiss (1980), Accurate time transfer during common-view of a GPS satellite, in 34^{th} *IEEE Symposium on Frequency Control*.

Ashjaee, Javad, and Robert Lorenz (1992), Precision GPS Surveying after Y-code, Ashtech, Sunnyvale, CA.

Bar-Sever, Yoaz E. (1997), New and Improved Solar Radiation Models for GPS Satellites Based on Flight Data, Final Report fo Air Force Materiel Command Space and Missile Systems Center/CZSF, April 1997.

Bar-Sever, Yoaz E. (1998), Estimation of the GPS Transmit Antenna Phase Center Offset, *presented at the AGU Spring Meeting, EOS Transactions*, *79*(45), 183, November 1998.

Beueršíma, I. (1983), NAVSTAR/Global Positioning System (GPS), II., Mitteilungen der Satelliten-Beobachtungsstation Zimmerwald, No. 10, Astronomical Institute, University of Berne.

Beutler, G. (1990*a*), Himmelsmechanik I, Mitteilungen der Satelliten-Beobachtungsstation Zimmerwald, No. 25, Astronomical Institute, University of Berne.

Beutler, G. (1990*b*), Numerische Integration gewöhnlicher Differentialgleichungenssysteme: Prinzipien und Algorithmen, Mitteilungen der Satelliten-Beobachtungsstation Zimmerwald, No. 23, Astronomical Institute, University of Berne.

Beutler, G. (1991), Himmelsmechanik II: Der erdnahe Raum, Mitteilungen der Satelliten-Beobachtungsstation Zimmerwald, No. 28, Astronomical Institute, University of Berne.

Beutler, G. (1998), Numerische Integration gewöhnlicher Differentialgleichungenssysteme: Prinzipien und Algorithmen.

Beutler, G., I. I. Mueller, and R. E. Neilan (1994*a*), The International GPS Service for Geodynamics (IGS): Development and Start of Official Service on January 1, 1994, *Bulletin Géodésique*, *68*(1), 39–70.

Beutler, G., E. Brockmann, W. Gurtner, U. Hugentobler, L. Mervart, and M. Rothacher (1994*b*), Extended Orbit Modeling Techniques at the CODE Processing Center of the International GPS Service for Geodynamics (IGS): Theory and Initial Results, *Manuscripta Geodaetica*, *19*, 367–386, April 1994.

Beutler, G., R. Weber, U. Hugentobler, M. Rothacher, and A. Verdun (1996*a*), GPS Satellite Orbits, in *Lecture Notes International School "GPS for Geodesy"*, Springer-Verlag, Delft, The Netherlands.

Beutler, G., E. Brockmann, U. Hugentobler, L. Mervart, M. Rothacher, and R. Weber (1996*b*), Combining Consecutive Short Arcs into Long Arcs for Precise and Efficient GPS Orbit Determination, *Journal of Geodesy*, *70*, 287–299.

Blewitt, G. (1990), An automatic editing algorithm for GPS data, *Geophysical Research Letters*, *17*(3), 199–202.

Blewitt, G., Y. Bock, and J. Kouba (1994), Constructing the IGS Polyhedron by Distributed Processing, in *IGS workshop on Densification of the IERS Terrestrial Reference Frame through regional GPS Networks*, edited by J.F. Zumberge and R. Liu, pp. 21–41, IGS Central Bureau, Jet Propulsion Laboratory, Pasadena, California U.S.A., November 1994.

Brockmann, E. (1997), *Combination of Solutions for Geodetic and Geodynamic Applications of the Global Positioning System (GPS)*, Geodätisch-geophysikalische Arbeiten in der Schweiz, Band 55, Schweizerischen Geodätischen Kommission, Institut für Geodäsie und Photogrammetrie, Eidg. Technische Hochscule Zürich, Zürich.

Bruyninx, C., D. Ineichen, and T. Springer (1998), The EUREF RNAAC: 1997 Annual Report, in *IGS 1997 Technical Reports*, edited by Ivan Mueller *et al.*, pp. 159–164, IGS Central Bureau, Jet Propulsion Laboratory, Pasadena, California U.S.A., October 1998.

Bruyninx, C. et al. (1997), The Use of the EUREF Permanent GPS Network for the Maintenance of the European Terrestrial Reference Frame, in *Proceedings of the Scientific Assembly of the International Association of Geodesy*, Rio de Janeiro, Brazil, September 3–9.

Clarke, J., J.A. Davis, and A.J. Lowe (1999), Characterisation of NPL's Geodetic GPS Time Transfer Receivers, in *Proceedings of the* 13^{th} *European Frequency and Time Forum EFTF 99*, Besançon, France.

Colombo, O. L. (1989), The Dynamics of Global Positioning Orbits and the Determination of Precise Ephemerides, *Journal of Geophysical Research*, *94*(B7), 9167–9182.

Degnan, John J., and Erricos C. Pavlis (1994), Laser Ranging to GPS Satellites with Centimeter Accuracy, *GPS World*, pp. 62–70, September 1994.

Dudle, G., F. Overney, L. Prost, T. Schildknecht, and T.A. Springer (1998), First Results on a Transatlantic Time and Frequency Transfer by GPS Carrier Phase, in *Proceedings of the 1998 PTTI meeting*, Reston, Virginia, U.S.A.

Dudle, G., F. Overney, L. Prost, T. Schildknecht, and T.A. Springer (1999), Transatlantic Time and Frequency Transfer by GPS Carrier Phase, in *Proceedings of the* 13^{th} *European Frequency and Time Forum EFTF 99*, Besançon, France.

Fliegel, H. F. (1993), Indirect Solar Pressure: Non-Equilibrium Force Models for GPS Satellites, presented at the American Geophysical Union Spring Meeting, Baltimore, Maryland, May 1993.

Fliegel, H. F., and T. E. Gallini (1989), Radiation Pressure Models for Block II GPS Satellites, in *Proceedings of the Fifth International Symposium on Precise Positioning with the Global Positioning System*, pp. 789–798, National Geodetic Survey, NOAA, Rockville, Md., April 1989.

Fliegel, H. F., and T. E. Gallini (1996), Solar Force Modeling of Block IIR Global Positioning System Satellites, *Journal of Spacecraft and Rockets*, *33*(6), 863–866, November–December 1996.

Fliegel, H. F., W. A. Feess, W. C. Layton, and N. W. Rhodus (1985), The GPS Radiation Force Model, in *Proceedings of the First International Symposium on Precise Positioning with the Global Positioning System*, edited by Clyde Goad, pp. 113–119, National Geodetic Survey, NOAA, Rockville, Md., March 1985.

Fliegel, H. F., T. E. Gallini, and E. R. Swift (1992), Global Positioning System Radiation Force Model for Geodetic Applications, *Geophysical Research Letters*, *97*(B1), 559–568.

Gambis, D. (1996), Multi-Technique EOP Combination, in *Proceedings of the 1996 IGS Analysis Center Workshop, Silver Spring, Maryland*, edited by R.E. Neilan *et al.*, pp. 61–70, IGS Central Bureau, JPL, March 19–21 1996.

Gendt, G. (1998), IGS Combination of Tropospheric Estimates – The Pilot Experiment, in *IGS 1997 Technical Reports*, edited by I. Mueller *et al.*, pp. 265–269, IGS Central Bureau, Jet Propulsion Laboratory, Pasadena, California U.S.A., October 1998.

Gurtner, W. (1994), RINEX: The Receiver-Independent Exchange Format, *GPS World*, *5*(7), 48–52.

Habrich, H. (1999), *Geodetic Applications of the Global Navigation Satellite System (GLONASS) and of GLONASS/GPS Combinations*, Ph.D. dissertation, Astronomical Institute, University of Berne, Berne, Switzerland.

Hackman, C., S. Jefferts, and T. Parker (1995), Common-clock two-way satellite time-transfer experiments, in *IEEE Symposium on Frequency Control*, San-Francisco.

Hofmann-Wellenhof, B., H. Lichtenegger, and J. Collins (1992), *GPS: Theory and Practice*, Springer, ISBN 3-211-82364-6.

Hugentobler, U. (1997), *Astrometry and Satellite Orbits: Theoretical Considerations and Typical Applications*, Ph.D. dissertation, Astronomical Institute, University of Berne, Berne, Switzerland.

IGS (1998), *IGS 1997 Annual Report*, IGS Central Bureau, IGS Central Bureau, JPL, Pasadena, California, USA.

Ineichen, D., M. Rothacher, T. Springer, and G. Beutler (1999), Computation of Precise GLONASS Orbits for IGEX-98, in *Proceedings of the IUGG meeting*.

Kirchner, D. (1991), Two-Way Time Transfer Via Communication Satellites, in *IEEE Symposium on Frequency Control*.

Kleusberg, A., and P. J. G. Teunissen (eds.) (1996), *GPS for Geodesy*, Lectures Notes in Earth Sciences, Springer Verlag.

Kouba, J. (1995), Analysis Coordinator Report, in *IGS 1994 Annual Report*, edited by J.F. Zumberge *et al.*, pp. 59–94, IGS Central Bureau, Jet Propulsion Laboratory, Pasadena, California U.S.A., September 1 1995.

Kouba, J. (1996), SINEX format description version 1.0, e-mail send to all IGS Analysis Centers.

Kouba, J., and Y. Mireault (1998*a*), 1997 Analysis Coordinator Report, in *IGS 1997 Annual Report*, IGS Central Bureau, Jet Propulsion Laboratory, Pasadena, California U.S.A.

Kouba, J., and Y. Mireault (1998*b*), 1997 Analysis Coordinator Report, in *IGS 1997 Technical Reports*, edited by Ivan Mueller *et al.*, pp. 23–70, IGS Central Bureau, Jet Propulsion Laboratory, Pasadena, California U.S.A., October 1998.

Kouba, J., J. Ray, and M. M. Watkins (1998), IGS Reference Frame Realization, in *Proceedings of the 1998 IGS Analysis Center Workshop*, edited by J. Dow *et al.*, ESA/ESOC, Darmstad, Germany, February 1998.

Leick, A. (1995), *GPS Satellite Surveying*, Wiley, ISBN 0-471-30626-6.

Marini, J.W., and C.W. Murray (1973), Correction of Laser Range Tracking Data for Atmospheric Refraction at Elevations Above 10 Degrees, *X–591–73–351*, NASA GSFC.

Martin Mur, T.J., T.A. Springer, and Y. Bar-Sever (1998), Orbit Predictions and Rapid Products, in *Proceedings of the IGS 1998 Analysis Center Workshop*, edited by J. Dow *et al.*, pp. 98–106, ESA/ESOC, Darmstad, Germany, February 1998.

McCarthy, D.D. (1992), IERS Standards (1992), *IERS Technical Note 13*, Observatoire de Paris, Paris, July 1992.

McCarthy, D.D. (1996), IERS Conventions (1996), *IERS Technical Note 21*, Observatoire de Paris, Paris, July 1996.

Melbourne, W. G. (1985), The Case for Ranging in GPS Based Geodetic Systems, in *Proceedings 1st International Symposium on Precise Positioning with the Global Positioning System*, edited by Clyde Goad, pp. 373–386, U.S. Department of Commerce, Rockville, Maryland.

Mervart, L. (1995), *Ambiguity Resolution Techniques in Geodetic and Geodynamic Applications of the Global Positioning System*, Geodätisch-geophysikalische Arbeiten in der Schweiz, Band 53, Schweizerischen Geodätischen Kommission, Institut für Geodäsie und Photogrammetrie, Eidg. Technische Hochscule Zürich, Zürich.

Mueller, I. I., and G. Beutler (1992), The International GPS Service for Geodynamics - Development and Current Structure, in *Proceedings 6th International Geodetic Symposium on Satellite Positioning, Vol. 2*, pp. 823–835, Ohio State University, Columbus, Ohio, USA.

Mueller, Ivan, Ruth Neilan, and Ken Gowey (1998), *IGS 1997 Technical Reports*, IGS Central Bureau, Jet Propulsion Laboratory, Pasadena, California U.S.A., October 1998.

Niell, A. E. (1996), Global Mapping Functions for the Atmosphere Delay at Radio Wavelengths, *Journal of Geophysical Research*, *101*(B2), 3227–3246.

Overney, F., L. Prost, U. Feller, T. Schildknecht, and G. Beutler (1997), GPS Time Transfer Using Geodetic Receivers: Middle Term Stability and Temperature Dependence of the Signal Delays, in *Proceedings of the* 11^{th} *European Frequency and Time Forum EFTF 97*, pp. 504–508, Warsaw, Poland, March 4–7 1997.

Overney, F., L. Prost, G. Dudle, T. Schildknecht, G. Beutler, J. A. Davis, J. M. Furlong, and P. Hetzel (1998), GPS Time Transfer Using Geodetic Receivers (GeTT): Results on European Baselines, in *Proceedings of the* 12^{th} *European Frequency and Time Forum EFTF 98*, Warsaw, Poland, March 10–12 1998.

Ray, J. (1999), IERS Analysis Campaign to Investigate Motions of the Geocenter, *IERS Technical Note 25*, Observatoire de Paris, Paris.

Rocken, C., C. Meertens, B. Stephens, J. Braun, T. VanHove, S. Perry, O. Ruud, M. McCallum, and J. Richardson (1996), Receiver and antenna test report, UNAVCO Academic Research Infrastructure (ARI).

Rothacher, M. (1992), *Orbits of Satellite Systems in Space Geodesy*, Geodätisch-geophysikalische Arbeiten in der Schweiz, Band 46, Schweizerischen Geodätischen Kommission, Institut für Geodäsie und Photogrammetrie, Eidg. Technische Hochscule Zürich, Zürich.

Rothacher, M. (1996), GPS Satellite Orbits, Orbit Determination and the IGS, in *Geodetic Applications of GPS, Lecture notes for Nordic Autumn School*, edited by Bo Jonsson, Nordic Geodetic Commission, Båstad, Sweden, August 1996.

Rothacher, M. (1998), Recent Contributions of GPS to Earth Rotation and Reference Frames, Habilitation (2nd Ph.D.), University Press, University of Berne.

Rothacher, M., G. Beutler, E. Brockmann, W. Gurtner, L. Mervart, R. Weber, U. Wild, A. Wiget, H. Seeger, and C. Boucher (1994), Annual Report of the CODE Analysis Center for 1993, IERS Technical Notes 17, September 1994.

Rothacher, M., G. Beutler, E. Brockmann, L. Mervart, R. Weber, U. Wild, A. Wiget, H. Seeger, S. Botton, and C. Boucher (1995*a*), Annual Report 1994 of the CODE Processing Center of the IGS, in *IGS 1994 Annual Report*, edited by J.F. Zumberge *et al.*, pp. 139–162, Central Bureau, JPL, Pasadena, Ca.

Rothacher, M., S. Schaer, L. Mervart, and G. Beutler (1995*b*), Determination of Antenna Phase Center Variations Using GPS Data, in *IGS Workshop Proceedings on Special Topics and New Directions*, edited by G. Gendt and G. Dick, pp. 77–92, GeoForschungsZentrum, Potsdam, Germany, May 15–18 1995.

Rothacher, M., G. Beutler, and L. Mervart (1995*c*), The Perturbation of the Orbital Elements of GPS Satellites Through Direct Radiation Pressure, in *IGS Workshop Proceedings on Special Topics and New Directions*, edited by G. Gendt and G. Dick, pp. 152–166, GeoForschungsZentrum, Potsdam, Germany, May 15–18 1995.

Rothacher, M., G. Beutler, E. Brockmann, L. Mervart, S. Schaer, T.A. Springer, U. Wild, A. Wiget, H. Seeger, and C. Boucher (1996*a*), Annual Report 1995 of the CODE Processing Center of the IGS, in *IGS 1995 Annual Report*, edited by J.F. Zumberge *et al.*, pp. 151–174, IGS Central Bureau, Jet Propulsion Laboratory, Pasadena, California U.S.A., September 1996.

Rothacher, M., W. Gurtner, S. Schaer, R. Weber, and H. O. Hase (1996*b*), Azimuth- and Elevation-Dependent Phase Center Corrections for Geodetic GPS Antennas Estimated from GPS Calibration Campaigns, in *IAG Symposium No. 115*, edited by W. Torge, pp. 335–339, Springer-Verlag.

Rothacher, M., T.A. Springer, S. Schaer, G. Beutler, E. Brockmann, U. Wild, A. Wiget, C. Boucher, S. Botton, and H. Seeger (1997*a*), Annual Report 1996 of the CODE Processing Center of the IGS, in *IGS 1996 Annual Report*, edited by J.F. Zumberge *et al.*, pp. 201–219, IGS Central Bureau, Jet Propulsion Laboratory, Pasadena, California U.S.A., November 1997.

Rothacher, M., T.A. Springer, S. Schaer, and G. Beutler (1997*b*), Processing Strategies for Regional GPS Networks, in *Proceedings of the IAG General Assembly in Rio, September, 1997*, Springer.

Rothacher, M., T.A. Springer, S. Schaer, G. Beutler, D. Ineichen, U. Wild, A. Wiget, C. Boucher, S. Botton, and H. Seeger (1998), Annual Report 1997 – CODE Analysis Center of the IGS, in *IGS 1997 Technical Reports*, edited by Ivan Mueller *et al.*, pp. 77–91, IGS Central Bureau, Jet Propulsion Laboratory, Pasadena, California U.S.A., October 1998.

Rothacher, Markus, and Leoš Mervart (1996), *The Bernese GPS Software Version 4.0*, Astronomical Institute, University of Berne, September 1996.

Saastamoinen, J. (1972), Atmospheric correction for the troposphere and stratosphere in radio ranging of satellites, In: The Use of Artificial Satellites for Geodesy, Geophysical Monograph Series.

Schildknecht, T., and T.A. Springer (1998), High Precision Time and Frequency Transfer using GPS Phase Measurements, in *Proceedings of the 1998 PTTI meeting*, Reston, Virginia, U.S.A.

Schildknecht, T., G. Beutler, W. Gurtner, and M. Rothacher (1990), Towards Subnanosecond GPS Time Transfer using Geodetic Processing Techniques, in *Proceedings of the* 4^{th} *European Frequency and Time Forum, EFTF 90*, pp. 335–346, Neuchâtel, Switzerland.

Seidelmann, P. K. (1992), Explanatory Supplement to the Astronomical Almanac, University Science Books, ISBN 0-935702-68-7.

Springer, T.A., M. Rothacher, and G. Beutler (1996), Using the Extended CODE Orbit Model: First Experiences, in *IGS 1996 Analysis Center Workshop*, edited by R.E. Neilan *et al.*, pp. 13–25, Central Bureau, JPL, Pasadena, Ca, March 19–21 1996.

Springer, T.A., W. Gurtner, M. Rothacher, and S. Schaer (1997), EUREF Activities at the CODE Analysis Center, in *Proceedings of the* 4^{th} *International Seminar on GPS in Central Europe*, vol. 4(27), pp. 165–176, Warsaw University of Technology, Warsaw, Poland, May 7–9 1997.

Springer, T.A., G. Beutler, and M. Rothacher (1998), A new Solar Radiation Pressure Model for the GPS Satellites, *GPS Solutions*, October 1998.

Springer, T.A., G. Beutler, and M. Rothacher (1999*a*), A new Solar Radiation Pressure Model for GPS, *Advances in Space Research*, *23*(4), 673–676.

Springer, T.A., G. Beutler, and M. Rothacher (1999*b*), Improving the Orbit Estimates of the GPS Satellites, *Journal of Geodesy*, *73*(3), 147–157.

Watkins, M. M., Y. E. Bar-Sever, and D. N. Yuan (1996), Evaluation of IGS GPS Orbits with Satellite Laser Ranging, in *IGS 1996 Analysis Center Workshop*, edited by R.E. Neilan *et al.*, pp. 9–12, Central Bureau, JPL, Pasadena, Ca, March 19–21 1996.

Wells, D. E., N. Beck, D. Delikaraoglou, A. Kleusberg, E. J. Krakiwski, G. Lachapelle, R. B. Langley, M. Nakiboglu, K. P. Schwarz, J. M. Tranquilla, and P. Vanicek (1987), *Guide to GPS Positioning*, Canadian GPS Associates, Fredericton, New Brunswick, ISBN 0-920-114-73-3.

Willis, P., G. Beutler, W. Gurtner, G. Hein, R. Neilan, and J. Slater (1998), The International Glonass Experiment IGEX-98, http://lareg.ensg.ign.fr/IGEX/goals.html.

Wübbena, G. (1985), Software Developments for Geodetic Positioning with GPS Using TI 4100 Code and Carrier Measurements, in *Proceedings First International Symposium on Precise Positioning with the Global Positioning System*, edited by Clyde Goad, pp. 403–412, U.S. Department of Commerce, Rockville, Maryland.

Zumberge, J. F., D. E. Fulton, and R. E. Neilan (1997*a*), *1996 Annual Report of the International GPS Service for Geodynamics*, IGS Central Bureau, Jet Propulsion Laboratory, Pasadena, California, U.S.A., November 1997, Workshop proceedings.

Zumberge, J. F., M. B. Heflin, D. C. Jefferson, M. M. Watkins, and F. H. Webb (1997*b*), Precise point positioning for the efficient and robust analysis of GPS data from large networks, *Journal of Geophysical Research*, *102*(B3), 5005–5017.

Zumberge, J.F., and R. Liu (1994), *Densification of the IERS Terrestrial Reference Frame through regional GPS Networks*, IGS Central Bureau, Jet Propulsion Laboratory, Pasadena, California U.S.A., Workshop proceedings.

Curriculum Vitae

Name	Springer, Timon Anton
Geburtsdatum	2. September 1965
Geburtsort	Willemstad, Curaçao, Niederländische Antillen
Staatsangehörigkeit	Niederländisch
Zivil stand	Verheiratet seit 1991 mit Johanna Catharina Springer–Neijzen
Kinder	Myra, geboren 15. July 1995 Pierce, geboren 26. Mai 1997 Quint, geboren 6. August 1998

1977 – 1984	Gymnasium in Den-Helder, Niederlande, Abitur 1984.
1984 – 1991	Studium an der Technischen Universität Delft, Niederlande.
Feb – Mai 1991	Praktikantenstelle an das "Brazilian National Space Research Center (INPE)". Arbeiten im Gebiet der Himmelsmechanik.
1990 – 1991	Diplom Arbeit: "Processing of GPS pseudo range and carrier phase measurements in order to obtain precise baselines". Abschluss als Dipl.-Ing. der Luft- und Raumfahrt 11. Dezember 1991.

Jan – Mai 1992	Assistent an der Technischen Universität Delft. Verarbeitung von GPS Daten des "GPS experiment for IERS and Geodynamics (GIG'91)".
1992 – 1993	Assistent am Astronomischen Institut der Universität Bern. Verarbeitung von GPS Daten der "International GPS Service for Geodynamics (IGS)".
1993 – 1995	Assistent an der Technischen Universität Delft. Verarbeitung von GPS Daten im Rahmen der "International GPS Service for Geodynamics (IGS)".
Seit Mai 1995	Assistent am Astronomischen Institut der Universität Bern. Studien zur Erlangung der Doktorwürde unter der Leitung von Prof. G. Beutler.